



Lehrstuhl für Elektrische Energiespeichertechnik
Fakultät für Elektrotechnik und Informationstechnik
Technische Universität München

Non-Invasive Aging Detection Methods of Lithium-Ion Batteries

Yao Wu, M.Sc.

Vollständiger Abdruck der von der Fakultät für Elektrotechnik und Informationstechnik der Technischen Universität München zur Erlangung des akademischen Grades eines

Doktor-Ingenieurs (Dr.-Ing.)

genehmigten Dissertation.

Vorsitzender: Prof. Dr. rer. nat. Bernhard Wolfrum

Prüfer der Dissertation: 1. Prof. Dr.-Ing. Andreas Jossen

2. Prof. Dr.-Ing. Kai-Olaf Hinrichsen

Die Dissertation wurde am 20.06.2018 bei der Technischen Universität München eingereicht und durch die Fakultät für Elektrotechnik und Informationstechnik am 01.10.2018 angenommen.

Acknowledgement

This doctoral dissertation is written during my work as a research associate at the Institute for Electrical Energy Storage Technology (EES) of Technical University of Munich from October 2013 to July 2018.

My deepest gratitude goes first and foremost to my supervisor Prof. Dr.-Ing. Andreas Jossen, for providing me this chance to complete my dissertation in an interesting research area and for his constant encouragement and guidance. I would also like to express my sincere gratitude to Prof. Dr. Jürgen Garche for the instructive discussions of my research topics.

My thanks also go to all the colleagues at EES for their constant support and the close cooperation. I would like to express my special thanks to Dr.-Ing. Peter Keil for the illuminating discussions and advice on my publications. I am also grateful to Jörn Wilhelm and Jonas Keil for their useful suggestions on my dissertation. I would also like to thank Matthieu Dubbary and the University of Hawaii at Mānoa for sharing the ‘alawa battery emulation toolbox.

Finally, I am indebted to my beloved family and friends for their continuous support and great confidence in me through all these years.

Yao Wu

Munich, Germany

June 12, 2018

Abstract

Lithium-ion battery degradation is a major problem, which hinders the further development of electric vehicles. The battery degradation depends largely on the electrode materials and electrolyte composition. Therefore, it is not possible to describe all the lithium-ion batteries with a universal aging model. Besides the macroscopic description of battery aging behavior, the internal aging mechanisms are also important for engineers to design functional battery systems.

This thesis presents a lithium-ion battery aging study, in which pouch cells comprising a $\text{LiCoO}_2/\text{LiNi}_{0.8}\text{Co}_{0.15}\text{Al}_{0.05}\text{O}_2$ blended cathode and a graphite anode are examined. The impacts of temperature, charge current and discharge current on the battery aging are investigated with experiments. Mathematical empirical aging models are established for the examined pouch cell based on knowledge from previous aging studies in literature.

In addition to the empirical models, non-invasive aging detection methods are employed to shed light on the degradation mechanisms inside the batteries during different operations. The idea is to make full use of the measurable electrical and thermal signals from a lithium-ion battery to give a comprehensive overview of its internal aging phenomena without disassembly. The detection methods are classified into three types based on the signals used: current-voltage-based aging detection, impedance-based aging detection and temperature-based aging detection.

Regarding the current-voltage-based aging detection, differential voltage analysis and incremental capacity analysis are applied to determine the lithium inventory loss and active material loss inside the battery, which are origins of capacity fade. Incremental capacity analysis is particularly useful for the degradation tracking in the blended cathode. The impedance-based aging detection, i.e., electrochemical impedance spectroscopy, provides information on the evolution of ohmic and non-ohmic resistances, which are attributed to different processes in the lithium-ion battery. The temperature-based detection method is developed to estimate capacity fade without direct current measurements. However, some preconditions need to be fulfilled in order to use this method. A combination of all the detection methods gives a detailed description of the degradation processes inside the examined lithium-ion battery without causing any additional damage to it.

A highlight in this thesis is the separation of the aging mechanisms of both components in the blended cathode via non-invasive aging detection methods. Different degradation patterns in the cathode components limit the normal use of conventional current-voltage-based detection methods and thus should be treated separately. Another highlight of this thesis is the newly developed temperature-based detection method, which makes use of the entropy characteristics

of a blended electrode. It can predict the state of health of the battery via a simple temperature measurement, when the battery is charged with a constant current from a fully discharged state.

Table of Contents

1	Introduction	1
1.1	Motivation	1
1.2	Outline.....	2
2	Fundamentals of Lithium-Ion Cells	5
2.1	Functional Components of a Lithium-Ion Cell	5
2.2	Blend Electrodes	6
2.2.1	Blended Anode	6
2.2.2	Blended Cathode.....	7
2.2.3	Blended Electrode Working Potential	8
2.3	Aging Mechanisms	9
2.3.1	Aging Mechanisms of the Anode	9
2.3.2	Aging Mechanisms of the Cathode	11
2.3.3	Aging Mechanisms of the Separator	12
3	State-of-the-Art Test Methods of Lithium-Ion Cells	13
3.1	State-of-the-Art Aging Test Methods	13
3.1.1	Overview of the Test Standards.....	13
3.1.2	Stress Factors for Calendar Aging and Cycle Life Aging	15
3.1.3	Design-of-Experiment	16
3.1.4	Empirical Aging Model	17
3.1.4.1	Model for Calendar Aging.....	17
3.1.4.2	Model for Cycle Life Aging	17
3.2	State-of-the-Art Non-Invasive Aging Detection.....	18
3.2.1	Capacity, State of Charge and State of Health	18
3.2.2	Current-Voltage-based Aging Detection	20
3.2.2.1	Open Circuit Voltage.....	20
3.2.2.2	Degradation Modes.....	22
3.2.2.3	Differential Voltage Analysis	24
3.2.2.4	Incremental Capacity Analysis	26
3.2.3	Impedance-based Aging Detection.....	28
3.2.3.1	Equivalent Circuit Model	28
3.2.3.2	Electrochemical Impedance Spectroscopy	29

3.2.4 Temperature-Based Aging Detection	32
3.2.4.1 Intercalation Entropy	32
3.2.4.2 Heat Generation	39
3.2.4.3 Cell Resistance Evolution.....	40
4 Experimental and Test Methods	43
4.1 Investigated Cell	43
4.1.1 Cell Variation	44
4.1.2 Capacity Rate Test.....	45
4.1.3 Electrode Material Identification.....	46
4.2 Performance Test Methods	46
4.3 Aging Test Methods.....	48
4.4 Half Cell Measurements.....	50
4.5 DC Pulse Resistance Test	51
5 Aging Test Results and Discussion	53
5.1 Aging Behavior of the Tested Lithium-Ion Cell	53
5.1.1 Calendar Aging.....	53
5.1.2 Cycle Life Aging	57
5.1.2.1 Effect of the Temperature.....	58
5.1.2.2 Effect of the Discharge Rate.....	63
5.1.2.3 Effect of the Charge Rate	68
5.2 Current-Voltage-Based Aging Detection.....	73
5.2.1 C/10 Charge Voltage Degradation	73
5.2.2 DVA Method	74
5.2.3 ICA Method.....	78
5.3 Impedance-Based Aging Detection	81
5.3.1 Nyquist Plots.....	81
5.3.2 Non-Ohmic Resistances	83
5.4 Temperature-Based Aging Detection.....	86
5.4.1 Surface Temperature Distribution	86
5.4.2 Temperature Variation Analysis.....	87
5.4.2.1 Temperature Increase during Charge/Discharge	87
5.4.2.2 Temperature Variation Rate	88
5.4.2.3 t_{\min} vs. Aging Detection.....	89

5.4.2.4 Current Optimization	91
6 Post-Mortem Analysis	95
7 Conclusion and Outlook	97
Appendix I	101
Appendix II	107
Bibliography	110

Abbreviations

AC	alternating current
ANSI	American National Standards Institute
BEV	battery-driven electric vehicle
BoT	begin of test
CC	constant current
CE	counter electrode
CV	constant voltage
DC	direct current
DoD	depth of discharge
DoE	department of energy
DVA	differential voltage analysis
ECM	equivalent circuit model
EDX	energy-dispersive X-ray
EFC	equivalent full cycle
EIS	electrochemical impedance spectroscopy
EoL	end of life
EoT	end of test
EV	electric vehicle
GHG	greenhouse gas
GITT	galvanostatic intermittent titration technique
HEV	hybrid electric vehicle
HPPC	hybrid pulse power characterization
ICA	incremental capacity analysis
ICEV	internal combustion engine vehicle
IEC	International Electrotechnical Commission
IEEE	Institute of Electrical and Electronics Engineers
ISO	International Standardization Organization
JEVA	Japan Electric Vehicle Association
LAM_{deAn}	loss of active material in the delithiated anode
LAM_{deCa}	loss of active material in the delithiated cathode
LAM_{liAn}	loss of active material in the lithiated anode
LAM_{liCa}	loss of active material in the lithiated cathode
LCO	lithium cobalt oxide
LFP	lithium iron phosphate

LIB	lithium-ion battery
LIC	lithium-ion cell
LLI	loss of lithium inventory
LMO	lithium manganese oxide
LTO	lithium titanate
NCA	lithium nickel cobalt aluminum oxide
NCO	lithium nickel cobalt oxide
NMC	lithium nickel manganese cobalt oxide
NMR	nuclear magnetic resonance
NTC	negative temperature coefficient
OCV	open circuit voltage
ORI	ohmic resistance increase
PHEV	plug-in hybrid electric vehicle
RC	resistor-capacitor
RE	reference electrode
RL	resistor-inductor
SAE	Society of Automotive Engineers
SEI	solid electrolyte interphase
SEM	scanning electron microscopy
SoC	state of charge
SoH	state of health
USABC	United States Advanced Battery Consortium
VDE	Verband Deutscher Elektrotechniker
WE	working electrode
XRD	X-ray diffraction

1. Introduction

Conventional light-duty internal combustion engine vehicles (ICEV) cause roughly 10% of energy consumption and greenhouse gas (GHG) emissions worldwide [1, 2]. Moreover, they emit exhaust containing particulates, SO_2 and NO_x , which can trigger serious environmental problems such as acidification, eutrophication and photochemical air pollution [3]. The exhaust problem can be mitigated via catalytic converters and filters, but the fossil energy resource and GHG emission problems remain unattended. The recent boom in the development of electric vehicles (EV) globally comes with the expectations to solve the last two problems by replacing ICEVs with EVs [3].

EVs encompass a variety of electrical propulsion systems for passenger cars, involving battery car, fuel cell car and serial hybrid car [3]. Recently, most of the automobile manufacturers are keenly interested in developing and promoting their own hybrid electric vehicles (HEV), plug-in hybrid electric vehicles (PHEV) and purely battery-driven electric vehicles (BEV). Batteries adopted in these battery cars are traction batteries. Lithium-ion battery (LIB) is currently the most mature and promising battery technology for traction application thanks to its extraordinarily high energy density [4]. In the rest of this thesis, the term EV will present all types of battery cars including HEVs, PHEVs and BEVs, to avoid any possible ambiguity.

1.1 Motivation

In the last decades, LIBs have already been employed in various application fields from portable devices to EVs. Unlike in portable devices, where the battery life usually exceeds the device life, EVs usually have more stringent demands on the electrical performance of LIBs as well as their long-term stability in the dynamic environment. Therefore, the investigation of LIB degradation is of ultimate importance for ensuring the safe and reliable operation of EVs [5].

In spite of the fact that electrification is the focus of almost all the automobile manufacturers, the EV market shares of most countries in 2016 are below 1.5% except for Norway, the Netherlands and Sweden [6]. Consumers are still concerned about charging infrastructure, charging time, driving range and traction battery lifetime. Regarding the last point, Tab. 1 gives an overview of traction battery lifetime warranty and end of life (EoL) capacity of several EV models based on the US market [7]. If the life span of the traction batteries is extended, EVs will be more economical for the consumers and a wider EV adoption could be realized.

A prerequisite for a longer battery life is a thorough understanding of the battery aging mechanisms. This thesis work is focused on the aging behavior of LIBs under various operational conditions and the non-invasive detection methods of the aging mechanisms. The investigation is carried out on single cell level, to exclude any influence from other components.

Table 1. Traction battery lifetime warranty of EV models [7].

Model	Period	Range	EoL Capacity
BMW i3s (94 Ah)	8 years/100,000 miles	124 miles	70%
BYD e6	10 years	186 miles	
Chevrolet Bolt EV	8 years/100,000 miles	238 miles	60%
Fiat 500e	8 years	84 miles	
Ford Focus Electric	8 years/100,000 miles	115 miles	
Kia Soul EV	10 years/100,000 miles	111 miles	70%
Mercedes B250e	8 years/100,000 miles	143 miles	70%
Nissan Leaf S	8 years/100,000 miles	151 miles	70%
smart fortwo electric	8 years/62,000 miles	124 miles	
Tesla Model S	8 years	304 miles	
Volkswagen e-Golf	8 years/100,000 miles	125 miles	70%

*The table includes actual information from automobile manufacturers' websites on May 22, 2018.

A cell is a basic electrochemical unit, whereas a battery is a collection of cells ready for use [8]. Hence, a lithium-ion cell (LIC) is used in the following text to refer to such a basic lithium-ion electrochemical unit.

1.2 Outline

This thesis is composed of six chapters as shown in Fig. 1. The first chapter introduces the industrial background for the booming of LIC technology and the significance to investigate its degradation behavior.

The second chapter provides the theoretical basis of LICs and their aging mechanisms based on a vast amount of literature. The aging mechanisms depend greatly on the electrode materials, thus some common electrode materials are introduced and their typical aging phenomena are discussed.

The third chapter focuses on the state-of-the-art aging test methods and non-invasive aging detection methods of LICs. For the state-of-the-art aging test, Section 3.1 gives an overview of some authoritative test standards for traction batteries. Based on these test standards and a literature review, the most important stress factors for calendar and cycle life aging tests are

extracted. The design of the experimental work depends on previous investigation results and the available testing resources. Empirical aging models from literature are introduced. As for the state-of-the-art non-invasive aging detection methods, Section 3.2 classifies them into three categories: current-voltage-based, impedance-based and temperature-based. The theoretical background of the aging detection methods is depicted in Subsection 3.2.2, Subsection 3.2.3 and Subsection 3.2.4.

The fourth chapter gives detailed information about the investigated LIC and describes the test procedures conducted within the framework of this thesis.

The fifth chapter analyzes the aging behavior of the investigated LIC and the corresponding non-invasive aging detection. The test results of calendar and cycle life aging are presented in Section 5.1. The impacts of temperature, discharge rate and charge rate on the LIC aging are discussed. In Section 5.2, Section 5.3 and Section 5.4, the three categories of non-invasive aging detection are applied to the investigated LIC to disclose its aging mechanisms under different operational conditions.

The sixth chapter shows the post-mortem analysis of one aged LIC. The last chapter summarizes the thesis work and provides some suggestions for future research.

This thesis contains text and figures from my peer-reviewed journal contributions [5,9], especially in Chapters 3, 4 and 5.

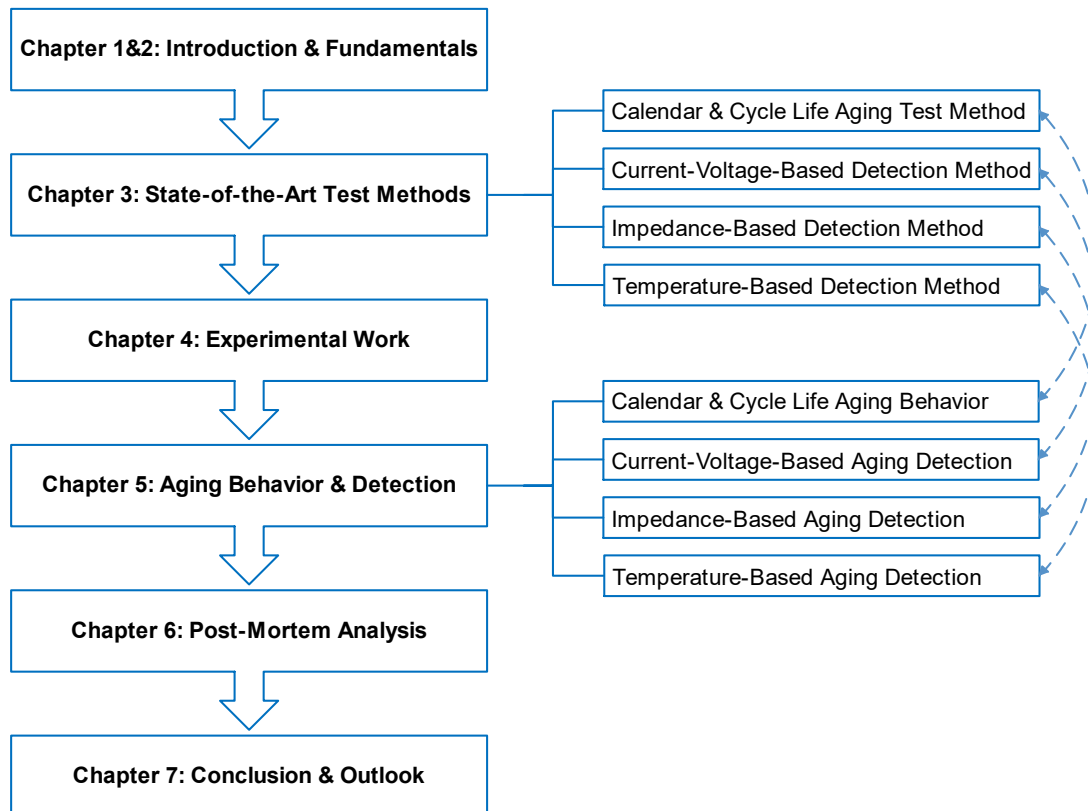


Figure 1. Structure of the thesis focused on aging test and detection of LICs.

2. Fundamentals of Lithium-Ion Cells

LICs are rechargeable batteries or secondary batteries, in which lithium ions move between the anode and the cathode during charge or discharge.

With a good combination of high energy density, tiny memory effect and low self-discharge, LICs have been adopted in systems from consumer electronics, EVs to renewable energy storage systems. Whatever the application is, LICs suffer from inevitable degradation, which depends greatly on the electrode and electrolyte composition. This chapter gives an introduction to LICs, including their composite materials and the degradation phenomena on each of their components.

2.1 Functional Components of a Lithium-Ion Cell

A LIC is composed of an anode, a cathode, a separator, electrolyte, current collectors and packaging materials. The anode is commonly made of graphitizable carbon (soft carbon) or non-graphitizable carbon (hard carbon). The former has more ordered crystallites orientation than the latter. At the moment, graphite is the most important anode material in LICs and it has received the most research attention [10]. The cathode material derives mainly from three groups: olivine material, e.g., LiFePO_4 (LFP), layered material, e.g., LiCoO_2 (LCO) and spinel material, e.g., LiMn_2O_4 (LMO). Anode and cathode materials enable the reversible intercalation and deintercalation of lithium ions.

The electrolyte is usually a mixture of alkyl organic carbonates containing lithium salts (e.g., LiPF_6) and additives [11]. The separator can be polymer membranes, non-woven fabric mats or inorganic composite membranes. It prevents the electrical contact between the electrodes and allows the transport of lithium ions in the electrolyte through it [12]. The anode current collector is made of copper and the cathode current collector is made of aluminum. They connect the electrodes with the external circuit. The packaging materials can be soft coffee bag, hard aluminum case or hard stainless steel case according to the LIC geometry and application.

Fig. 2 illustrates the interior structure of a LIC with a graphite anode and an LCO cathode [13]. During charge, electrons move from the cathode to the anode via the external circuit. Inside the LIC, lithium ions deintercalate out of the cathode, transport through the Li^+ -conductive electrolyte and intercalate into the anode.

The discharge process is contrariwise. The operational potential of a LIC depends primarily on the anode and cathode materials. The capacity of a LIC depends on the type and amount of active anode and cathode materials.

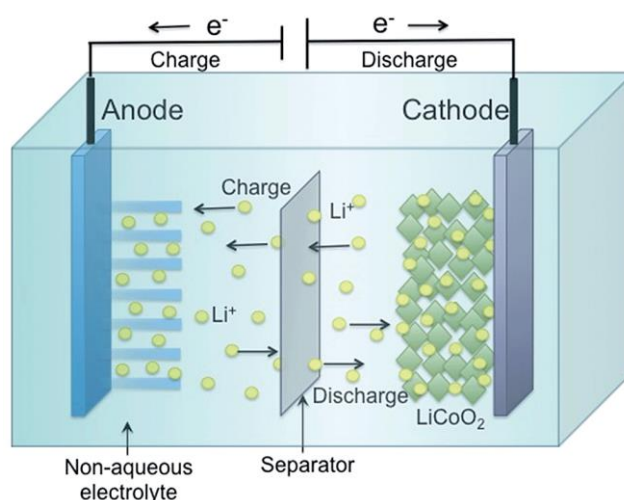


Figure 2. Schematic of a LIC with a graphite anode and an LCO cathode during charge or discharge [13].

2.2 Blended Electrodes

Different electrode materials possess different advantages and disadvantages regarding price, resource, thermal stability, chemical stability and energy density. A blended electrode is developed by physically mixing two or more lithium intercalation compounds to compensate the demerits of one compound with the merits of another [14].

2.2.1 Blended Anode

In addition to the aforementioned carbon-based anodes, $\text{Li}_4\text{Ti}_5\text{O}_{12}$ (LTO) and silicon (Si) are excellent candidates for LIC anode material. Pure LTO anode has already been commercialized, whereas the development of pure Si anode encounters difficulties due to large volume change, typically up to 270% [15].

The most common blended anode is graphite/Si anode, as a way to overcome the large volumetric expansion of pure Si. Graphite is well known for its good stability, cheap cost and low working potential, while Si has a ten times higher specific capacity than graphite and is the second most abundant element in the Earth's crust. Their working potential curves vs. Li/Li^+ are shown in Fig. 3 (a). In the blended anode, the specific capacity increases with Si content and the volumetric expansion is limited since Si particles are uniformly located within the space between graphite particles. However, besides volume change, lithium ions tend to remain in the Si particles as LiSi_x , which causes capacity fade during the operation [16].

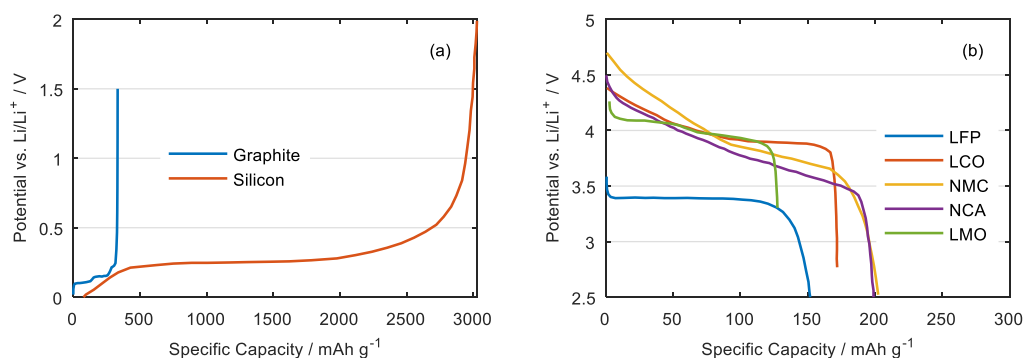


Figure 3. (a) Discharge profiles of graphite [17] and silicon [18] at C/10; (b) discharge profiles of LFP [19], LCO [20], NMC [21], NCA [22] and LMO [23] at C/10 or C/20.

2.2.2 Blended Cathode

As mentioned in Subsection 2.1, cathodes come from three groups: olivine, layered and spinel materials. Discharge potential profiles of various cathode materials from the three groups are shown in Fig. 3 (b).

LFP is the most commercially successful material in the olivine group, also known as polyanion compounds. It has a lower potential as well as a lower specific capacity compared to materials from the other groups. However, LFP has a good thermal stability, high power capability and long cycle life.

LCO was firstly introduced by Goodenough in 1980 and commercialized by SONY. It is still to be found in many commercial LICs. LCO has relatively high specific capacity, low self-discharge, high working potential and long cycle life [24]. However, high cost for cobalt, low thermal stability and fast capacity fade at high currents or deep cycling are the main limits of LCO. LCO suffers from irreversible lattice distortion from hexagonal to monoclinic symmetry at over 50% lithium delithiation, which is the most important material degradation for LCO during cycling. In order to avoid this deterioration, different transition metals are used as dopants for cobalt. Some compositions have achieved success in stabilizing the layered structure. $\text{LiNi}_{1/3}\text{Mn}_{1/3}\text{Co}_{1/3}\text{O}_2$ (NMC) and $\text{LiNi}_{0.8}\text{Co}_{0.15}\text{Al}_{0.05}\text{O}_2$ (NCA) are the most successful representatives of them [15].

Spinel LMO has the advantages of low cost, abundant supply and environmental friendliness. Its three-dimensional structure enables fast lithium ion diffusion through it, thus high rate capability. Nevertheless, its specific capacity is the lowest in Fig. 3 (b). Furthermore, LMO suffers from irreversible side reactions with electrolyte, oxygen loss and Mn^{2+} dissolution [15].

Blended cathodes are often found in EV batteries, since automotive propulsion applications have higher requirements on LICs in terms of energy, power, safety and life span. For example, *Ford Focus BEV* and *Chevrolet Volt* use LICs with NMC/LMO blended cathodes [14].

There are generally four types of blended cathodes: blends of spinel and layered oxides, blends of olivines and layered oxides, blends of LCO with NMC, NCA or spinel and blends with $x\text{Li}_2\text{MnO}_3-(1-x)\text{LiMO}_2$ ($M=\text{Mn, Ni, Co}$) systems [14, 25, 26].

In the first type, spinel has lower cost, higher working potential, higher rate capability and better thermal stability [27], which perfectly compensate the shortcomings of layered oxides. Furthermore, several research groups [25, 28, 29] have reported about the suppression of Mn^{2+} dissolution of spinel by adding layered oxides. The most important blended cathodes of this type are NMC/LMO and NCA/LMO.

In the second type, olivine-structured cathodes have the favorable attributes of good thermal stability and long cycle life [30]. However, their relatively flat potential profiles make them less attractive for EV applications. Blending with layered oxides overcomes the disadvantages of olivines. For example, blended cathode LFP/Li[Li_{0.17}Mn_{0.58}Ni_{0.25}]O₂ has been reported to present advantages in cost, safety and rate capability [31]. This blending system is particularly interesting for PHEV-related applications [32].

In the third type, LCO is known as the most successful cathode material, but it suffers from poor thermal stability and irreversible lattice deterioration during overcharge. Lee et al. [33] improved the thermal stability of the LCO cathode by adding NMC.

The last type of blending system is also known as “ Li_2MnO_3 -stabilized” oxides. Li_2MnO_3 helps to stabilize layered structure of LiMO_2 ($M=\text{Mn, Ni, Co}$) and thus the blends achieve enhanced performance [34, 35]. The blended cathodes can reach relatively high specific capacity of 250-280 mAh/g. The disadvantage is high irreversible capacity fade in the first cycles.

As a summary, blended cathodes provide a more balanced performance than their composite materials due to the weighted averaging of the material properties. However, there are still some problems with blended cathodes. In spinel-containing blends, Mn^{2+} dissolution remains a challenge for LIC cycle life. Additionally, the usage of the composite materials depends on their working potentials. It is possible that the composite materials are not uniformly utilized during the whole charge/discharge process [14].

2.2.3 Blended Electrode Working Potential

Anode and cathode can be regarded as serial-connected potential sources, whereas composite materials in the blended electrode are considered as parallel-connected potential sources. Fig. 4 shows the equivalent circuit for a LIC with a blended cathode and a blended anode. The electrodes contain two composite materials respectively. On the cathode side, $Z_{\text{ca},1}$ and $Z_{\text{ca},2}$ are the impedances of the two cathode composite materials and $U_{\text{ca},1}$ and $U_{\text{ca},2}$ are their potentials. U_{ca} is the potential of the blended cathode. On the anode side, $Z_{\text{an},1}$ and $Z_{\text{an},2}$ are the impedances of the two anode composite materials and $U_{\text{an},1}$ and $U_{\text{an},2}$ are their potentials. U_{an} is the potential of the blended anode. Z_0 is the impedance of the rest components inside the LIC. U_{OCV} is the

open circuit voltage (OCV) of the LIC, which is the potential difference between the cathode and the anode in a static state:

$$U_{OCV} = U_{ca} - U_{an} \quad (1)$$

$Z_{ca,1}$ and $Z_{ca,2}$ are usually not identical, and neither are $Z_{an,1}$ and $Z_{an,2}$. However, if the current inside the LIC is low enough, the voltage drops over $Z_{ca,1}$, $Z_{ca,2}$, $Z_{an,1}$ and $Z_{an,2}$ are negligible. The following equations can be obtained under this precondition [36].

$$U_{ca} = U_{ca,1} = U_{ca,2} \quad (2)$$

$$U_{an} = U_{an,1} = U_{an,2} \quad (3)$$

Hence, the same working potential applies to the composite materials.

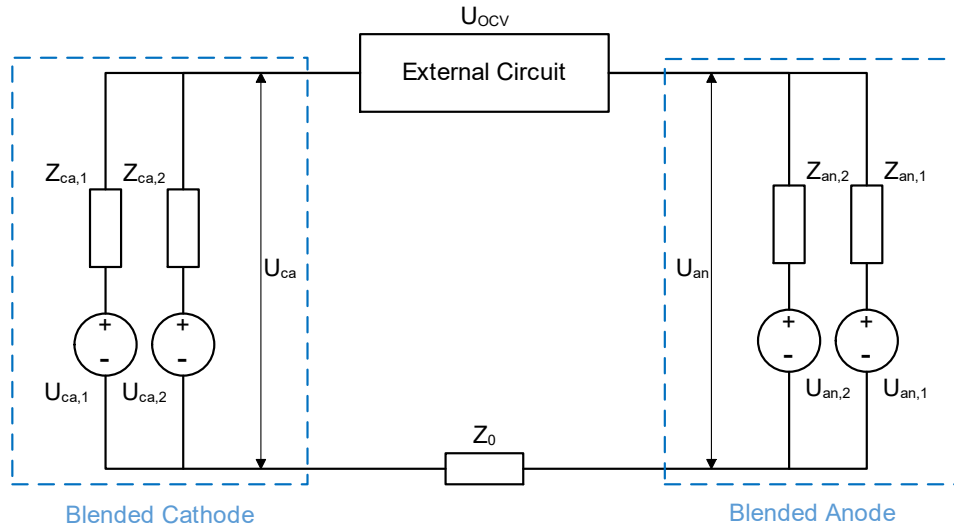


Figure 4. An equivalent circuit for a LIC with a blended anode and a blended cathode.

2.3 Aging Mechanisms

The performance characteristics of LICs are mainly capacity and resistance. If a LIC's capacity reduces or its resistance rises, the LIC is aged. However, various aging mechanisms are involved in these two kinds of performance degradation. In the following subsections, aging mechanisms are categorized into: aging mechanisms of the anode, aging mechanisms of the cathode and aging mechanisms of the separator.

2.3.1 Aging Mechanisms of the Anode

Since graphite is the most widely used anode material, the aging mechanisms discussed in this subsection is confined to graphite anode. During charge and discharge, i.e., intercalation and deintercalation of lithium ions in graphite, a volume change in the order of 10% or less takes place in the graphite anode, which may cause particle cracking or related structural change [15]. Moreover, graphite exfoliation and cracking due to solvent co-intercalation, electrolyte reduction and gas evolution inside graphite may also occur in the anode. However, the most

pronounced aging mechanisms on the anode side occur at the anode/electrolyte interface, i.e., the formation of a solid electrolyte interphase (SEI) and lithium plating [37–39].

Solid Electrolyte Interphase

The lithiated graphite operates at low potentials, causing electrochemical instability of the electrolyte. Hence, during the initial cycles of a LIC, the SEI is formed with electrolyte decomposition products covering the anode surface [39–42]. These decomposition products contain mainly Li_2CO_3 , LiOH , LiF , Li_2O , ROCO_2Li , and RCOLi [43]. An ideal SEI should be electronically insulating and only allow lithium ion conduction, thus it inhibits further electrolyte reduction in the successive cycles. However, some charged species and solvents do pass through the SEI to some extent after the first few cycles. In fact, SEI formation occurs throughout the whole life of a LIC [39, 40]. In the meanwhile, lithium ions are irreversibly consumed, resulting in capacity fade. After a long period of cycling or storage, the SEI may grow thicker and insert into pores of the anode and even into pores of the separator, diminishing the accessible active surface area of the anode. It is a major cause for lithium plating under mild operational conditions [44].

Moreover, changes of composition and morphology of the SEI with time and temperature have also been reported, e.g., the inorganic compositions increase and the organic compositions decrease with time [45–49]. Both the growth and the conversion of SEI layer cause impedance rise in the LIC. Furthermore, the SEI is highly dependent on the electrolyte formula and its growth can be influenced by dissolved cathode components in the electrolyte [50, 51].

Lithium Plating

The intercalation potential of graphite is approximately the potential of lithium metal [39]. When the potential at the graphite/electrolyte interface drops below 0 V vs. Li/Li^+ , lithium plating begins [52]. The factors that trigger lithium plating can be classified into thermodynamic factors and kinetic factors. Thermodynamic factors refer to the cell unbalance situation, where the anode is already fully lithiated before the end of charge. Cell unbalance could be due to poor cell design or aging-induced anode material loss. Kinetic factors are more common. They are harsh cell charging conditions (e.g., low temperature, high charge current), aging-induced anode/electrolyte interface degradation (e.g., SEI formation, surface porosity reduce) and inappropriate electrolyte formulation [53].

Lithium plating occurs during the charge process and especially at the end of the constant current (CC) charge step, where the anode potential develops to its lowest point. Hence, the extent of the lithium plating reaction is at its maximum. If a subsequent constant voltage (CV) charge step begins, the charging current declines and the anode potential rises. The plated lithium begins to re-intercalate into the graphite anode. During this step, there is a coexistence of lithium plating, plated lithium re-intercalation and lithium ion intercalation [54]. If a relaxation period follows the CV charge step, more plated lithium re-intercalates into the

unsaturated graphite anode [55]. When a discharge current is applied to a LIC with plated lithium on the anode, it is possible that the plated lithium is partially recovered as active lithium, known as reversible lithium plating. It takes place because lithium oxidation (stripping) occurs at a lower potential than lithium deintercalation out of graphite. The reversible lithium plating does not contribute to capacity loss in the LIC [53]. However, there is still a part of the plated lithium, which is not oxidized during discharge. This is known as irreversible lithium plating [56]. The irreversible plated lithium accumulates on the anode with operation and reacts with the electrolyte to form new SEI [57–59]. It may lose contact with the anode to form dead lithium or build dendrites, which eventually penetrate the separator and cause short circuits in the LIC [56, 60, 61]. Irreversible lithium plating leads to capacity loss as well as safety issues.

Lithium plating is one of the most detrimental degradation mechanisms in the LIC. It is a major limiting factor for the application of LICs and the development of fast charging for EVs. It also relates to the transition from linear to nonlinear aging of LICs during normal operation [44, 62], thus a great risk for second life application of LICs. Lithium plating could be eased through material improvement, cell design, thermal management and adapted charge protocols.

2.3.2 Aging Mechanisms of the Cathode

Lithium ion (de-)intercalation in the cathode induces mechanical strain to the cathode particles, further causing particle isolation and phase transition in the cathode [39]. The degradation of the cathode may result in active lithium ion isolation and cathode capacity decrease, both leading to LIC capacity loss. Besides the general degradation mechanisms brought by (de-)intercalation, cathode has specific aging mechanisms according to the active material. Layered oxide Li_xCoO_2 is prone to a transition to a monoclinic structure at $x=0.5$ [63, 64], while spinel LMO suffers from structural changes due to Jahn-Teller distortion of Mn^{3+} [65]. Additionally, transition metal dissolution and electrolyte oxidation are aging mechanisms commonly observed in LIC cathodes.

Transition Metal Dissolution

The transition metals in the cathode are not always stable during the operation. High cell voltage can oxidize transition metals into dissoluble cations, especially in the cases of cobalt and manganese. The cations dissolve into the electrolyte and eventually deposit on the anode. The deposited transition metals accelerate the SEI formation, leading to capacity fade and impedance rise in the LIC. This aging phenomenon has been detected in LICs with LCO [66], LFP [67, 68], NMC [69–71] and LMO [72–74] cathodes.

Electrolyte Oxidation and Passive Film Formation

The organic carbonates in the electrolyte have an oxidation potential around 4.7 V vs Li/Li^+ [75, 76]. This oxidation potential can be reduced via temperature elevation [65, 77, 78]. Furthermore, ethers, esters and some partially reduced lithium compounds from the anode can be oxidized at even lower potentials [79–81]. A passive film composed of organic and inorganic

compounds from electrolyte decomposition is formed on the cathode [58]. There is an investigation reporting about passive film formation at 4.3 V vs Li/Li⁺ on various cathode materials at 25°C [82]. Under the oxidized electrolyte compounds film, there exists an inorganic surface layer owing to cathode surface deterioration, such as surface reconstruction or phase change [21, 83]. When a LIC is charged or stored at high potentials, the passive films develop at the electrolyte/cathode interface. It gives rise to resistance increase of the cathode side, which can be more pronounced than that of SEI on the anode side [79, 84].

2.3.3 Aging Mechanisms of the Separator

Separators suffer from swelling and internal or external mechanical stress, leading to cracks or viscoelastic creep in them [85, 86]. Furthermore, electrolyte decomposition products [87] and even electrode active material particles [86] may clog the pores in the separator. All these degradation phenomena result in an increased ionic resistivity of the separator and in turn a higher LIC resistance.

In addition to the aforementioned aging mechanisms, current collector corrosion, binder decomposition, gas evolution, etc. have also been reported in literature [39, 88–90].

3. State-of-the-Art Test Methods of Lithium-Ion Cells

3.1 State-of-the-Art Aging Test Methods

LICs are tested to evaluate their performance under various operational conditions. Application-oriented LIC performance tests consist of at least three parts: characterization tests to obtain cell features, aging tests to simulate the working scenarios and safety tests to investigate extreme conditions. Safety tests are beyond the scope of this thesis, thus only characterization tests and aging tests are discussed in Section 3.1.

3.1.1 Overview of the Test Standards

Standards for products and services are usually created by public or private standardization organizations. In the area of battery standardization, International Electrotechnical Commission (IEC), International Standardization Organization (ISO) and Institute of Electrical and Electronics Engineers (IEEE) are the three most active entities. In Europe, the European Committee for Electrotechnical Standardization is involved in battery standardization. There are also standards from individual countries, especially United States of America (SAE and ANSI), Germany (VDE), Japan (JEVA) and China [91].

LIC-related standards cover different objectives, including design, performance tests, safety design, safety tests, environmental protection, classification, guidance and recommendation. Based on the interest of this thesis, LIC-related standards with focus on performance tests for automotive application are selected as follows [92]:

- ISO 12405-1: Electrically propelled road vehicles – Test specification for lithium-ion traction battery packs and systems – Part 1: High-power applications
- ISO 12405-2: Electrically propelled road vehicles – Test specification for lithium-ion traction battery packs and systems – Part 2: High-energy applications
- Battery test manual for plug-in hybrid electric vehicles (INL/EXL-07-12536): The development of this test standard for PHEV is supported by the Department of Energy (DOE)-United States Advanced Battery Consortium (USABC).

The performance tests consist of a characterization part describing the energy and power features of the battery and an aging part evaluating the battery degradation over time (calendar aging) or usage cycles (cycle life aging). Tab. 2 and Tab. 3 describe the main characterization tests and aging tests according to the selected standards.

Table 2. Battery characterization tests according to selected standards [91–95].

Application	ISO 12405-1 (2009)	ISO 12405-2 (2009)	INL/EXT-07-12536 (2014)
Capacity Test	-18°C, -10°C, 0°C, 25°C and 40°C discharge at 1C, 10C and I_{\max}	-25°C, -10°C, 0°C, 25°C and 40°C discharge at 1/3C, 1C, 2C and I_{\max}	According to the manufacturer
Power Test	pulse at SoCs (20%, 35%, 50%, 65% and 80%) and temperatures (-18°C, -10°C, 0°C, 25°C and 40°C) with charge/discharge current of I_{\max} for 18 s and $-0.75I_{\max}$ for 10 s	pulse at SoCs (20%, 35%, 50%, 70% and 90%) and temperatures (-25°C, -18°C, -10°C, 0°C, 25°C and 40°C) with charge/discharge current of I_{\max} for 18 s, $0.75I_{\max}$ for 102 s and $-0.75I_{\max}$ for 20 s	Hybrid Pulse Power Characterization (HPPC): 10 s discharge pulse at I_{\max} and 10 s charge pulse at $0.75I_{\max}$ at each 10% SoC interval from 10% to 90% SoC with 1 hour rest
Energy Efficiency Test	pulse at SoCs (65%, 50% and 35%) and temperatures (0°C, 25°C and 40°C) with charge current of I_{\max} or 20C for 12 s and discharge current of $0.75I_{\max}$ or 15C for 16 s; a 40 s rest between charge and discharge	Fast charging at 25°C and 0°C: Fast charge at 1C, 2C or I_{\max} and rest 1 hour, followed by standard discharge	Charge-sustaining test profiles are used for the efficiency tests and are 90 s in duration.

Table 3. Battery aging tests according to selected standards [91–95].

Application	ISO 12405-1 (2009)	ISO 12405-2 (2009)	INL/EXT-07-12536 (2014)
Calendar Aging Test	Storage at 45°C and 50% SoC for 30 days; The remaining capacity is measured by a 1C discharge test.	Storage at 45°C and 50% SoC for 30 days; The remaining capacity is measured by a 1/3C discharge test.	Storage at 100% or a target SoC at three different temperatures; A 10 kW constant power discharge test and a HPPC test are repeated every 32 days.
Cycle Life Aging Test	Cycling with charge and discharge rich profiles between 30%-80% SoC at 25°C; A pulse test is repeated every 7 days; A 1C capacity test is repeated every 14 days.	Cycling with dynamic discharge profiles A and B from 100% to 20% SoC at 25°C; A 1/3C capacity test and a pulse power test at 25°C are repeated every 28 days; A 1/3C capacity test and a pulse power test at -10°C are repeated every 2 months.	Charge-sustaining cycle life test; Charge-depleting cycle life test

3.1.2 Stress Factors for Calendar Aging and Cycle Life Aging

According to Tab. 3, LICs undergo two kinds of aging tests in the application, i.e., calendar aging test and cycle life aging test. Calendar aging corresponds to the standby mode, whereas cycle life aging represents the working load condition. The selected test standards adopt different testing conditions for calendar aging and cycle life aging tests in Tab. 3. They differ in temperature, state of charge (SoC), cycling profiles, etc., which are referred to as stress factors by some researchers [96–98]. “1C”, “1/3C” and “2C” are mentioned in Tab. 2 and Tab. 3. C-rate is a unit of charge/discharge current for batteries. 1C means the constant current, with which the full cell capacity is theoretically discharged in 1 h, e.g., 1C is 5 A for a LIC with 5 Ah. By introducing C-rate, the charge/discharge current can be better compared between LICs with different capacities.

A classification of basic stress factors for calendar aging and cycle life aging is illustrated in Fig. 5. Charge and discharge currents are listed as stress factors instead of dynamic cycling profiles in Tab. 3, since it is difficult to compare dynamic cycling profiles directly. There are

also researchers [99], who have put forward new stress factors, e.g., cut-off voltage and CV time. However, they are merely different expressions of depth of discharge (DoD) and average SoC. A superposition assumption between calendar aging and cycle life aging is generally accepted [98, 100–102]. That means, during LIC operation, its total aging is the addition of its calendar aging and its cycle life aging.

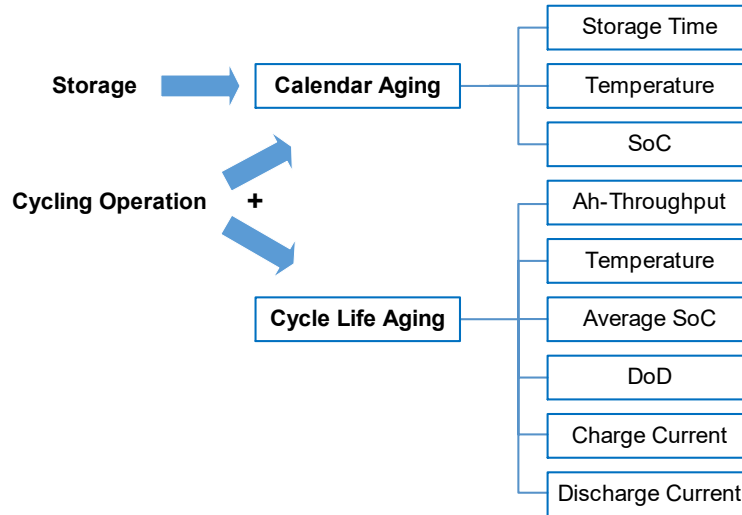


Figure 5. Stress factors of calendar aging and cycle life aging.

3.1.3 Design-of-Experiment

Large-scale aging experiments have been carried out by many research groups [97, 98, 103, 104] to obtain semi-empirical aging models for LICs. In spite of their lower predictability compared to physicochemical aging models, semi-empirical aging models require lower computation time and are thus more suitable for integration into battery management systems [105].

As illustrated in Fig. 5, there are three basic stress factors for calendar aging and six basic stress factors for cycle life aging. For each stress factor, at least three test points should be chosen to obtain a reliable aging-dependence. Furthermore, under each test point, at least two LICs should be tested to ensure the reproducibility of the measurement. As a result, if a detailed investigation covering all the stress factors is to be carried out, hundreds of LICs are involved. In order to reduce the test expenditure, for calendar aging only two stress factors are chosen, temperature and storage time. The cycle-life-aging dependence on DoD has been clarified by a few groups [106, 107] with Wöhler-curve or Stress-cycle-curve, where the LIC life span decreases exponentially with increasing DoD. The cycle-life-aging dependence on average SoC could hardly be investigated without the known calendar-aging dependence on SoC. Hence, for cycle life aging, ambient temperature, charge current, discharge current and Ah-throughput are selected as stress factors.

Orthogonal test design is employed to further reduce test points [98, 99]. Two LICs are measured under the same condition. The test range for the stress factors considers the safe

operation range according to the battery technical data sheet. In my experiment, six cells are tested for calendar aging and sixteen cells are tested for cycle life aging.

The test profiles for cycle life aging could be specific profiles related to the application, e.g., charge depleting and charge sustaining profiles in INL/EXT-07-12536 and dynamic discharge profiles in ISO 12405. Nonetheless, in order to investigate the current intensity influence on aging, simplified protocols with CC-CV charge and CC discharge regimes are more appropriate.

3.1.4 Empirical Aging Model

Macroscopic LIC aging phenomena, i.e., capacity loss and resistance increase, can be described with empirical aging models. The stress factors serve as variants in the model. The models require test data for parameterization.

3.1.4.1 Model for Calendar Aging

For calendar aging, SEI growth is considered to be the most pronounced aging mechanism. Capacity fade is mainly due to SEI growth. An exponential aging model with stress factors, i.e., storage time, temperature and SoC, is proposed by researchers [104, 108–110] as follows:

$$Q_{\text{loss}}^{\text{cal}} = B_{\text{cal}} \exp\left(-\frac{Ea_{\text{cal}}}{RT}\right) t^{z_{\text{cal}}} \quad (4)$$

Where $Q_{\text{loss}}^{\text{cal}}$ is the relative capacity loss, B_{cal} is a pre-exponential factor depending on SoC, Ea_{cal} is the activation energy in J/mol, R is the gas constant 8.314 J/mol/K, T is the absolute temperature in K, t is the storage time and z_{cal} is a dimensionless constant.

Resistance increase has a similar model but with different parameters:

$$R_{\text{inc}}^{\text{cal}} = B'_{\text{cal}} \exp\left(-\frac{Ea'_{\text{cal}}}{RT}\right) t^{z'_{\text{cal}}} \quad (5)$$

Where $R_{\text{inc}}^{\text{cal}}$ is the relative resistance increase, B'_{cal} is a pre-exponential factor depending on SoC, Ea'_{cal} is the activation energy in J/mol and z'_{cal} is a dimensionless constant.

3.1.4.2 Model for Cycle Life Aging

The cycle life aging model develops with Ah-throughput instead of time. Some research groups [104, 108] adopt an analogous model to the calendar model:

$$Q_{\text{loss}}^{\text{cyc}} = B_{\text{cyc}} \exp\left(\frac{-Ea_{\text{cyc}} + \alpha|I|}{RT}\right) q^{z_{\text{cyc}}} \quad (6)$$

Here, $Q_{\text{loss}}^{\text{cyc}}$ is the relative capacity loss, B_{cyc} is a pre-exponential factor, Ea_{cyc} is the activation energy in J/mol, α is a coefficient for aging acceleration due to charge/discharge current in J-h/mol, I is the charge/discharge C-rate in h⁻¹, q is the Ah-throughput and z_{cyc} is a dimensionless constant.

Similarly, the resistance increase model is expressed as follows:

$$R_{inc}^{cyc} = B'_{cyc} \exp\left(\frac{-Ea'_{cyc} + a'|I|}{RT}\right) q^{z'_{cyc}} \quad (7)$$

Where R_{inc}^{cyc} is the relative resistance increase, B'_{cyc} is a pre-exponential factor, Ea'_{cyc} is the activation energy in J/mol, a' is a coefficient for aging acceleration due to charge/discharge current in J·h/mol and z'_{cyc} is a dimensionless constant.

DoD is proven to show negligible influence on cycle life aging by Wang et al. [104], when the total Ah-throughput is applied. For degradation due to cycling operation, the calendar aging (Eq. 4-5) should be added to the cycle life aging (Eq. 6-7).

3.2 State-of-the-Art Non-Invasive Aging Detection

In order to detect aging mechanisms, an enormous number of investigations have been undertaken in the last decades. The most straightforward method is to disassemble an aged LIC and examine its components with physicochemical analysis techniques such as nuclear magnetic resonance spectroscopy (NMR), scanning electron microscopy (SEM) and X-ray diffraction technique (XRD) [111]. These detection methods are referred to as post-mortem analysis, which requires pricey analysis equipment as well as cell disassembly. In the hope of tracking aging mechanisms in a LIC without damaging it and in a more economical way, non-invasive aging detection methods have become research highlights of many groups globally. Without destroying a LIC, the measurable parameters are mainly current, voltage, impedance and temperature. In the following part of Section 3.2, a literature survey and the non-invasive measurements are presented to show how these parameters reveal the aging mechanisms in the LIC.

3.2.1 Capacity, State of Charge and State of Health

Before having a deep look into the non-invasive aging detection methods, there are three technical terms, which should be understood thoroughly. One of them is capacity. There are different definitions of LIC capacity in literature, which should be clarified before defining the concepts SoC and state of health (SoH).

There are three main capacity definitions, i.e., nominal capacity, initial capacity and actual capacity. The nominal capacity is the capacity defined by the manufacturer for operation under nominal conditions (nominal temperature, nominal charge/discharge current, etc.). It is the guaranteed minimal capacity by the manufacturer at the time of delivery. The initial capacity is the charge amount that can be withdrawn from a LIC in a new state starting from a fully charged condition. The initial capacity under nominal conditions is usually slightly higher than its nominal capacity. The actual capacity is the charge amount that can be withdrawn from a LIC in its actual state starting from a fully charged condition. If a LIC is aged, its actual capacity is lower than its initial capacity. The initial and actual capacities can be defined at either nominal

or non-nominal conditions. The influence of conditions on capacity is prominent. Higher temperature and lower discharge current increase capacity [112].

The concept SoC has been utilized to describe lead-acid batteries and nickel-cadmium batteries [113]. In LIC research literature, SoC has two different definitions. There is a true SoC (t-SoC), which is defined under thermodynamic equilibrium and corresponds to a certain lithiation state of both electrodes. The other one is an empirical SoC (e-SoC), which is defined empirically via engineering methods. The measurement of t-SoC requires techniques such as galvanostatic intermittent titration technique (GITT) or very low currents (typically C/25), which makes t-SoC infeasible in most applications [114–116]. Therefore, in the rest part of this thesis, only e-SoC is discussed and used. For convenience, e-SoC will be replaced with SoC from now on.

SoC describes the availability of usable capacity that can be deployed from a LIC or a battery module/pack. From engineering perspective, SoC acts as a fuel gauge for battery-powered systems and provides a basis for the comparison of LIC performance characteristics [116]. According to USABC Battery Test Procedure Manual [117], SoC is defined as the ratio of the remaining capacity under a given testing condition and the actual capacity under the same specific condition as follows:

$$SoC = \frac{Q_{\text{res}}}{Q_{\text{act}}} \quad (8)$$

Where Q_{res} is the remaining capacity and Q_{act} is the actual capacity under the same testing condition.

Besides, SoC is commonly determined with coulomb counting method, which counts electrical charges into or out of the LIC [116].

$$SoC(t) = SoC_0 + \frac{\int_0^t \eta i dt}{Q_{\text{act}}} \quad (9)$$

Here, SoC_0 is the initial SoC, η is the coulombic efficiency, i is the current (positive for charge; negative for discharge), t is the time and Q_{act} is the actual capacity.

SoH describes the performance difference between the present condition and the initial condition of a LIC due to aging. Nevertheless, there is actually no consensus in the industry regarding SoH definition and determination. Different performance features can be used to quantify SoH and they result in different SoH values. Considering energy and power as the most important features of a battery system, capacity and resistance are usually applied to define SoH [112, 118]:

$$SoH_Q = \frac{Q_{\text{act}}}{Q_{\text{ini}}} \quad (10)$$

$$SoH_R = \frac{R_{\text{act}}}{R_{\text{ini}}} \quad (11)$$

Where Q_{act} is the actual capacity, Q_{ini} is the initial capacity, R_{act} is the actual resistance and R_{ini} is the initial resistance. Some researchers [112, 118, 119] replace the initial capacity with the nominal capacity, which may cause SoH values larger than 100%. In order to keep SoH_Q within the range 0-100%, the definition with initial capacity is employed in this thesis.

For applications where battery energy plays a more important role, e.g., EVs or plug-in EVs, EoL criteria of a battery system is set as 70% or 80% SoH_Q. As for situations where battery power is more crucial, e.g., HEVs, EoL criteria is defined as 200% SoH_R [103, 120, 121]. In most cases, the health evaluation of a LIC should consider both SoHs. Due to different operational conditions and battery materials, there could be different extent of resistance increase for the same degree of capacity decrease [118, 122].

Additional concepts such as state of energy, state of function [112] and state of safety [123] exist, but are not discussed in this thesis.

3.2.2 Current-Voltage-Based Aging Detection

The most fundamental current-voltage description of a LIC is its OCV curve. Detection methods like incremental capacity analysis (ICA) and differential voltage analysis (DVA) amplify the characteristics along the OCV curve or the pseudo-OCV curve to unravel the involved aging mechanisms.

3.2.2.1 Open Circuit Voltage

The OCV of a LIC is the potential difference between the cathode and the anode, when no external electric current flows between the electrodes and all the internal chemical and physical processes are finished or in equilibrium. The OCV excludes all the dynamic influences and depends only on the temperature and the lithiation degree of both electrodes (or SoC) for the same LIC system. It has already been defined with Eq. 1 in Subsection 2.2.3.

The relationship between $U_{\text{OCV}}(Q)$, $U_{\text{ca}}(Q)$ and $U_{\text{an}}(Q)$ is illustrated in Fig. 6. The potential curves are obtained from half cell measurements of a fresh LIC. The x-axis shows the absolute capacities of the half cells and the full cell. The cathode has an initial capacity of $Q_{\text{ini,ca}}$ and the anode $Q_{\text{ini,an}}$. The anode is designed to be over-sized ($Q_{\text{ini,ca}} < Q_{\text{ini,an}}$), so that at the end of charge the anode is not yet saturated and thus thermodynamic lithium plating can be avoided. During the long-term operation, both electrodes may lose some active materials, which can be described with scaling factors α_{ca} and α_{an} , respectively. The actual capacities of the cathode and the anode are then expressed as follows:

$$Q_{\text{ca}} = Q_{\text{ini,ca}} \cdot \alpha_{\text{ca}}, \quad 0 < \alpha_{\text{ca}} \leq 1 \quad (12)$$

$$Q_{\text{an}} = Q_{\text{ini,an}} \cdot \alpha_{\text{an}}, \quad 0 < \alpha_{\text{an}} \leq 1 \quad (13)$$

In a LIC, its fully delithiated anode does not correspond to its fully lithiated cathode. This is due to the loss of a certain amount of cyclable lithium during the SEI formation in the formation

cycles. An offset (OFS) thus exists between both electrodes in Fig. 6. The OFS expands with aging as more cyclable lithium are consumed by side reactions.

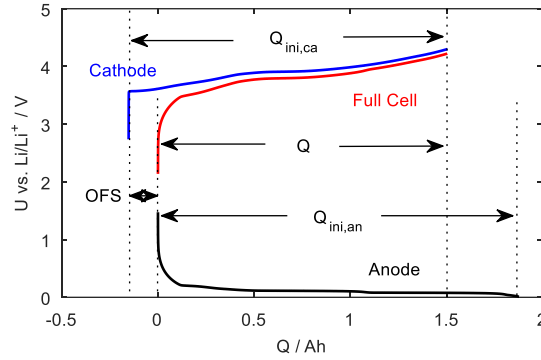


Figure 6. Schematic of OCV and electrode potentials based on half cell measurements of a fresh Kokam cell.

The OCV curve covering the full SoC range of a LIC can be attained via GITT or by averaging charge and discharge voltage curves at the same current [124]. Fig. 7 illustrates the OCV curve of a fresh LIC used in the experimental part of this thesis via the averaging method. At a charge/discharge current of C/10, the averaged OCV curve is approximately identical with the charge curve as shown in Fig. 7. For convenience, the C/10 charge curve replaces the OCV curve in the current-voltage-based aging detection analysis.

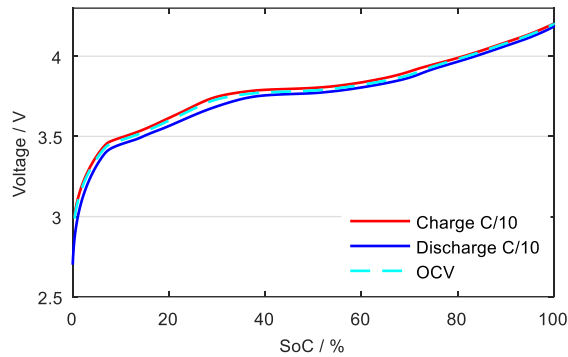


Figure 7. The OCV curve of a fresh Kokam cell as the average of its charge and discharge curves at C/10. Due to large diffusion overpotentials at low SoC range during the discharge process, the OCV curve is determined with a constant voltage difference to the charge curve between 0% and 50% SoC.

The charge curve in Fig. 7 possesses several voltage plateaus, corresponding to two-phase areas of co-existing intercalation phases in either anode or cathode [125–128]. These voltage plateaus can be amplified with differentiation methods displayed in Fig. 8. The differential capacity curve in Fig. 8 (b) and the differential voltage curve in Fig. 8 (c) are referred to as ICA and DVA respectively by researchers [73, 129, 130].

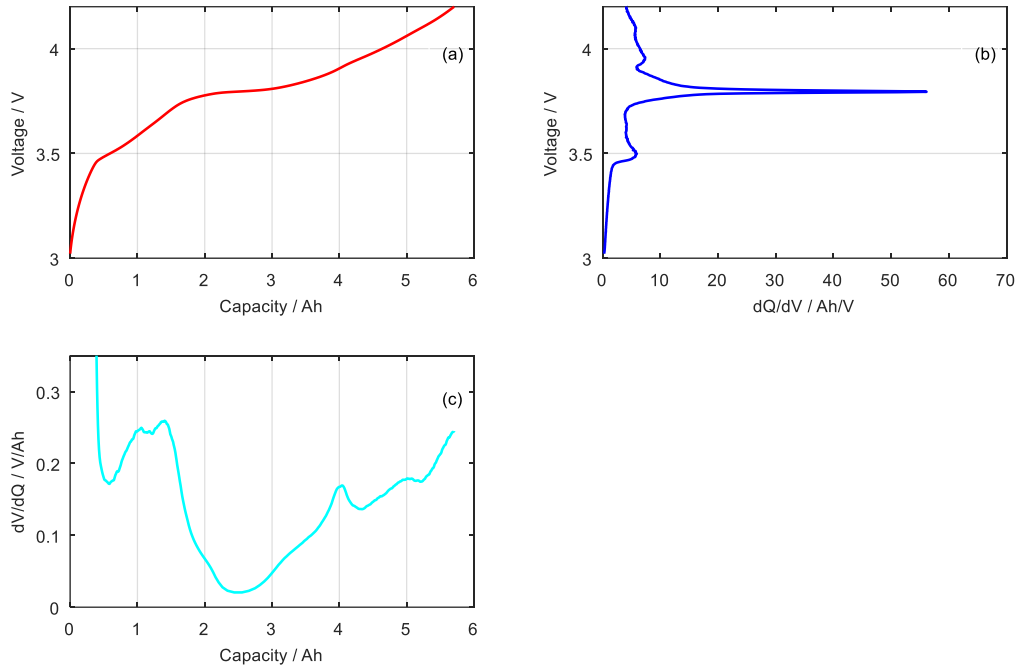


Figure 8. (a) The charge curve of a fresh Kokam cell at C/10; (b) the differential capacity curve vs. voltage derived from the charge curve in (a); (c) the differential voltage curve vs. capacity derived from the charge curve in (a).

3.2.2.2 Degradation Modes

Section 2.3 gives a comprehensive description of all the common aging mechanisms in LICs. According to their influences on the LIC, six basic degradation modes can be defined: loss of lithium inventory (LLI), loss of active material in the lithiated cathode (LAM_{LiCa}), loss of active material in the delithiated cathode (LAM_{deCa}), loss of active material in the lithiated anode (LAM_{LiAn}), loss of active material in the delithiated anode (LAM_{deAn}) and ohmic resistance increase (ORI). LLI is induced by lithium-ion-consuming aging mechanisms e.g., SEI formation and lithium plating. It exists almost in every operation case and dominates in the early stage of aging [131–133]. All four types of LAM are due to contact loss between the material particles [134], transition metal dissolution, electrode composition variation [69], or structural change in the active material [135]. ORI is due to electric contact loss in the electrode, electrolyte degradation or passive layer formation [135, 136].

The aforementioned six degradation modes are then synthesized based on Fig. 6, according to Ref. [137]. In Fig. 9 (a)–(e), the results show the loss of active material or lithium inventory from 0% to 25% at an interval of 5%. ORI has no influence on the OCV, thus a discharge current of C/25 is assumed in Fig. 9 (f). The ohmic resistances of both electrodes increase from 0% to 500% at an interval of 100%. Fig. 9 (a) stands for the case of LAM_{LiCa} , causing fewer lithium ions can be released from the cathode at the end of charge. It leads immediately to full cell capacity fade. Fig. 9 (b) represents LAM_{deCa} , where the cathode can take in fewer lithium ions at the end of discharge. It influences the full cell capacity under the condition that the

cathode material decrease exceeds the initial offset. Fig. 9 (c) illustrates LAM_{deAn} , where the anode arrives at a more lithiated state at the end of charge due to its active material loss. The full cell capacity stays the same unless the anode is already fully lithiated at the end of charge. LAM_{deAn} introduces only slight deformation in the full cell OCV if no full cell capacity fade is observed.

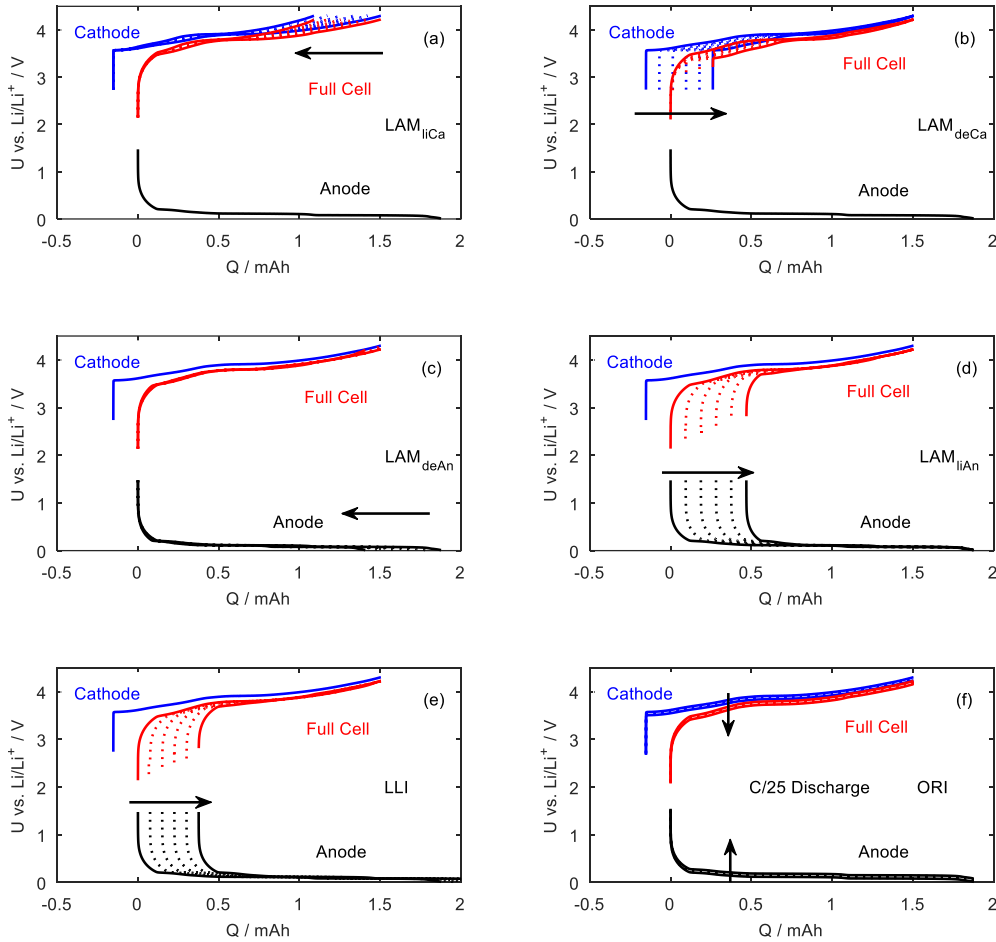


Figure 9. The six synthesized degradation modes: (a) LAM_{liCa} ; (b) LAM_{deCa} ; (c) LAM_{deAn} ; (d) LAM_{liAn} ; (e) LLI; (f) ORI. The OCV curves are shown for (a)-(e) and the C/25 discharge curve is shown for (f). Solid lines: start and end positions of the electrode or full cell; Dashed lines: 5% intervals of LAM for (a)-(d), 5% intervals of LLI for (e) and 100% intervals of ORI for (f).

Fig. 9 (d) describes LAM_{liAn} , where the anode sets fewer lithium ions free at the end of discharge. It influences the cell capacity immediately. Fig. 9 (e) depicts LLI, which is basically an expansion of the initial offset. LAM_{liCa} , LAM_{deAn} and LLI are more common in the charge regime, while LAM_{deCa} and LAM_{liAn} occur more often in the discharge regime [137]. Fig. 9 (f) shows ORI, where the cell capacity is not affected but the discharge curve at C/25 decreases in

its potential due to increased resistances on both electrodes. In the following subsections, the six degradation modes will be analyzed with ICA and DVA.

3.2.2.3 Differential Voltage Analysis

DVA has been employed by Bloom et al. [138–141] and Dahn et al. [142] for non-invasive aging analysis. As explained in Subsection 2.2.3, the anode and the cathode are considered as serial-connected voltage sources, thus the superposition principle works for DVA [138, 143], as shown in Eq. 14.

$$\frac{dU_{OCV}}{dQ} = \frac{dU_{ca}}{dQ} - \frac{dU_{an}}{dQ} \quad (14)$$

The superposition principle can be validated with the voltage curves of the half cells during de-/intercalation. A fresh Kokam cell was disassembled and half cells were built out of its electrodes versus lithium metal. Details about the half cell assembly and measurement are revealed in Section 4.4. Figs. 10 (a) and 10 (b) present the half cell voltage curves and DVA curves that correspond to the charging of the full cell. The full cell DVA curve in Fig. 10 (c) was calculated from the charge voltage curve of the full cell with a current of $C/10$ from 2.7 V to 4.2 V. As illustrated in Fig. 10 (c), the peaks in the charge DVA curve of a full cell can be attributed to both electrodes according to the DVA superposition principle in Eq. 14. These distinguishable peaks, valleys or ends are marked conforming to their electrode origins as A1, A2, A3, C1, C2 and C3. The x-axis distances between peaks, valleys or ends from the same electrode can be used to determine changes in the active material amount of this electrode [5].

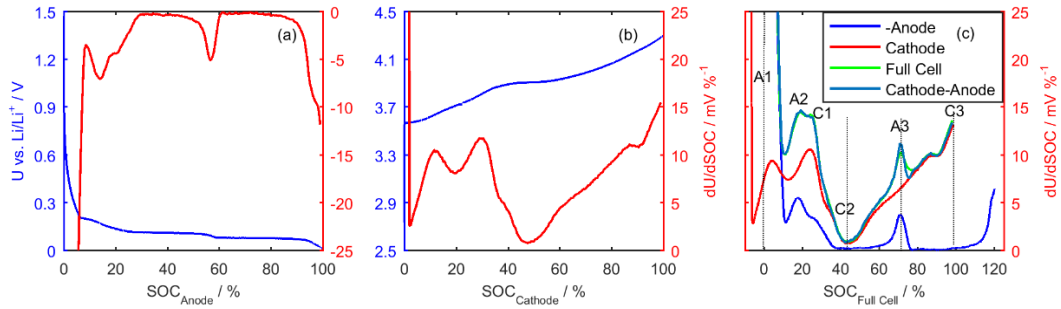


Figure 10. Half cell voltage curves and the resulting DVA curves of (a) anode and (b) cathode, which correspond to the full cell; (c) superposition of both half cell DVA curves and comparison with the full cell DVA curve [5].

As the OCV deforms due to the degradation modes in Fig. 9, the DVA curve of the full cell in Fig. 11 deforms accordingly. The red thick line stands for the initial state and the other thin lines are intervals of LAM, LLI or ORI. The SoC scale is based on the initial state. In Fig. 11 (a), i.e., LAM_{LiCa} , the decrease of cyclable lithium is obvious with the decrease of the x-axis distance between A1 and C3. The decrease of the cathode active material is observed with the decrease of the x-axis distance between C1 and C2. In Fig. 11 (b), the amount of cyclable lithium is firstly not affected from 0% to 10% LAM_{deCa} . With more LAM_{deCa} , the cyclable

lithium begins to decrease and the starting point A1 (SoC=0%) is limited by the cathode in the meantime. The loss of the cathode active material can be detected via the x-axis distance between C2 and C3. In Fig. 11 (c), the amount of cyclable lithium stays constant until 15% LAM_{deAn} and decreases subsequently. The decline of the anode active material can be recognized through the decrease of the x-axis distance between A1 and A3.

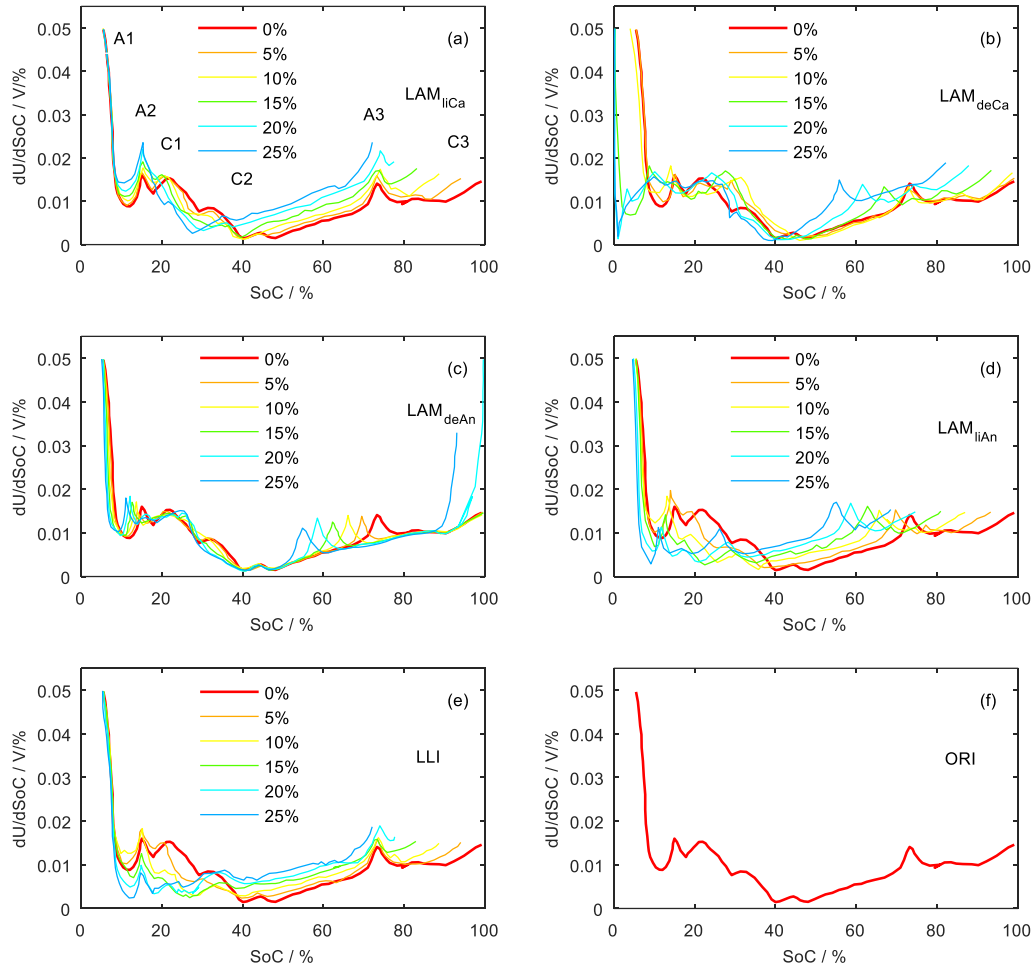


Figure 11. The C/25 charge DVA evolution of six synthesized degradation modes: (a) LAM_{LiCa} ; (b) LAM_{deCa} ; (c) LAM_{deAn} ; (d) LAM_{LiAn} ; (e) LLI; (f) ORI.

In Fig. 11 (d), i.e., LAM_{LiAn} , the decrease of cyclable lithium and anode active material can be easily monitored by the shift of A3 and C3. In the case of LLI in Fig. 11 (e), the gradual left-shift of the C3 end leads eventually to the disappearance of the A3 peak. Only the loss of cyclable lithium is observed here. Finally, no DVA change is visible for ORI in Fig. 11 (f), since ORI does not affect the total amount of cyclable lithium or the form of OCV. It is regarded as a limitation of DVA for degradation detection.

3.2.2.4 Incremental Capacity Analysis

The Clauss group [144] firstly introduced the method ICA in 1976 on a Leclanché-type dry cell. In the last decade, Dubarry et al. [115, 132, 133] have performed a series of aging characterization work by means of ICA on a wide range of LIC chemistries. According to Dubarry et al., although ICA and DVA share similar information due to their reciprocal nature, ICA has the advantage that it relates with the cell voltage, which is a direct and primary indicator of the battery state. In contrast, DVA refers to the cell capacity, which is an accumulative and secondary indicator of the battery state.

However, ICA is at a disadvantage compared to DVA when it comes to peak separation. The superposition principle between cathode, anode and full cell does not apply to ICA, which can be depicted by the inverse of Eq. 14 in the following equation:

$$\frac{dQ}{dU_{OCV}} = \frac{1}{\frac{dU_{ca}}{dQ} - \frac{dU_{an}}{dQ}} = \frac{dQ}{dU_{ca} - dU_{an}} \neq \frac{dQ}{dU_{ca}} - \frac{dQ}{dU_{an}} \quad (15)$$

The ICA peaks cannot be directly attributed to each electrode, but they can be distinguished with the help of DVA. It is known that ICA is the reciprocal of DVA, thus an ICA peak corresponds to a DVA valley in Fig. 8. The origins of the ICA peaks are marked with a1, a2 (a for anode) and c1 (c for cathode) in Fig. 12 (a). Peak a1 is the first potential plateau when lithiating the graphite anode, corresponding to the valley between A1 and A2 in Fig. 10 (c). Peak a2 is the potential plateau shortly after the LiC_{12} to LiC_6 transition staging during the anode lithiation process, which is peak A3 in Fig. 10 (c). Peak c1 refers to the large potential plateau in the middle of the cathode potential curve and valley C2 in Fig. 10 (c).

Fig. 12 presents the same degradation modes as Fig. 9 and Fig. 11. In Fig. 12 (a), a1 and a2 move to higher voltages, since the cathode potential rises when it goes through LAM_{LiCa} . LAM_{LiCa} also leads to the shrinkage of c1, as less cyclable lithium is involved in this cathode transition reaction. In Fig. 12 (b), a1 and a2 move to lower voltages because the cathode potential declines in the case of LAM_{deCa} . The area under peak c1 decreases only after the cathode becomes the limiting electrode at the end of discharge. The most noticeable change in Fig. 12 (c) is the shift of a1 and a2. Peak a1 moves to a slightly lower voltage due to the decline of the anode potential through LAM_{deAn} . The shift of a2 is more pronounced, since the $\text{LiC}_{12}/\text{LiC}_6$ transition staging moves much closer to the end of discharge than in the initial state. It is also noticeable that the end-of-charge voltage decreases in the final aging state owing to an excess of the cathode material.

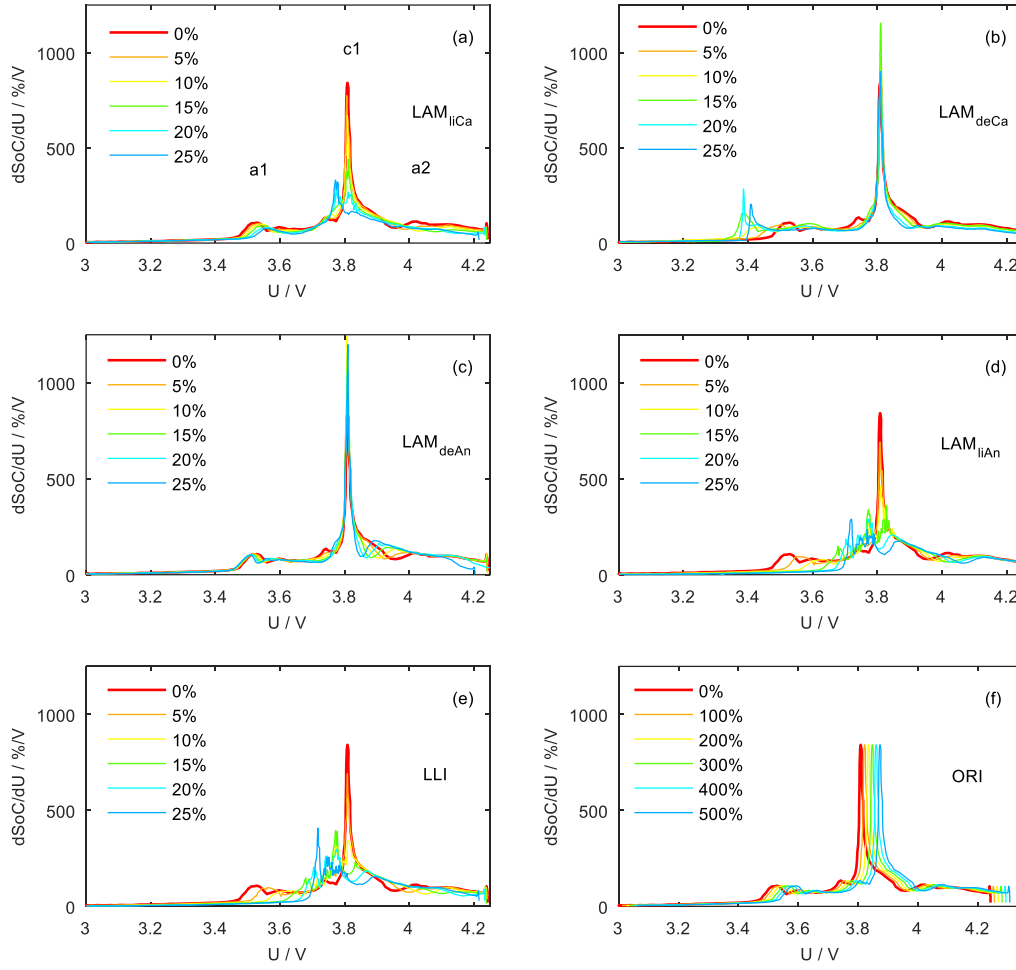


Figure 12. The C/25 charge ICA evolution of six synthesized degradation modes: (a) LAM_{LiCa} ; (b) LAM_{deCa} ; (c) LAM_{deAn} ; (d) LAM_{LiAn} ; (e) LLI; (f) ORI.

In the case of LAM_{LiAn} in Fig. 12 (d), the first anode potential plateau (a1) moves to a higher voltage. Peak a2 moves to a higher voltage as well but to a less extent. The shifted a1 interferes gradually with c1 until it disappears in the final state. LLI has a similar influence on ICA when comparing Fig. 12 (e) with Fig. 12 (d). The major difference is that peak a2 moves faster to the end of charge in the case of LLI. In Fig. 12 (f), ICA keeps exactly the same form and all peaks move to higher voltages during charging (contrariwise during discharging). ICA shows an advantage over DVA in the detection of ORI.

Furthermore, ICA method can be used to investigate blended electrode. As explained in Subsection 2.2.3, composite materials of the blended electrode are parallel-connected voltage sources, thus the electrode capacity is the capacity addition of both composite materials. A similar superposition principle can be established for ICA [5, 36, 145]. The percentages of composite materials are α and $(1 - \alpha)$. In the case of a two-component cathode, the following equations are obtained:

$$Q_{ca}(U) = \alpha \cdot Q_{ca,1}(U) + (1 - \alpha) \cdot Q_{ca,2}(U) \quad (16)$$

$$\frac{dQ_{ca}}{dU} = \alpha \cdot \frac{dQ_{ca,1}}{dU} + (1 - \alpha) \cdot \frac{dQ_{ca,2}}{dU} \quad (17)$$

The precondition for the ICA superposition principle is that the applied current should be low enough to eliminate the influence from the resistance difference of both composite materials. The principle also works for more-component electrode systems.

3.2.3 Impedance-Based Aging Detection

The electrical impedance describes the relationship between alternating current and alternating voltage on a conductor. According to the reaction of the circuit element to the voltage, the impedance can be classified into three types, i.e., ohmic resistance, capacitance and inductance. The three impedance types correspond to different components or processes in the LIC. Hence, the change of the impedance with aging can be used to detect aging mechanisms.

3.2.3.1 Equivalent Circuit Model

When a constant discharge current is applied to a LIC, its voltage response is shown in Fig. 13. The voltage drop process is comprised of three parts: the voltage drop due to ohmic resistance, which takes effect immediately; the voltage drop caused by charge transfer resistance, which begins after a time delayed determined by the double layer capacitance; the voltage drop owing to diffusion resistance, which is the result of lithium ion diffusion into and out of active materials and within the electrolyte [146, 147].

It is apparent that the LIC contains resistance and capacitance. Furthermore, the LIC also has an inductive part, which can only be observed at high frequencies. A LIC can be described with an equivalent circuit model (ECM) comprised of ohmic resistance, capacitance and inductance elements as shown in Fig. 14.

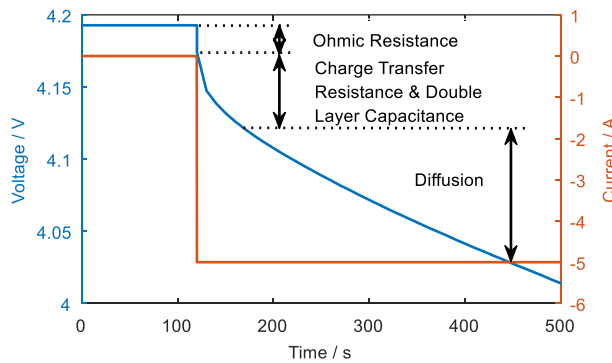


Figure 13. Schematic of LIC voltage response to a constant discharge current.

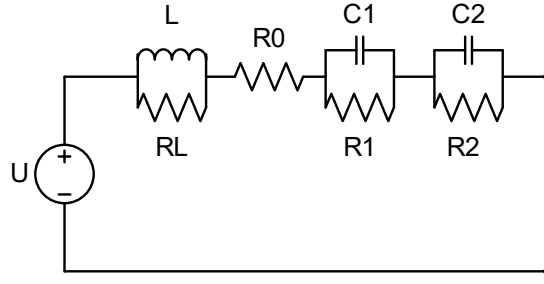


Figure 14. A LIC ECM with two RC elements.

The resistor-inductor (RL) element represents the inductive part of the LIC. The resistor R0 stands for the ohmic resistance contributions inside the LIC, including electrolyte, electrodes, separator, current collectors, etc. The two resistor-capacitor (RC) elements describe the charge transfer process and the diffusion process. The accuracy of the ECM can be improved with more RC elements in series or by adding Warburg elements to describe the diffusion process.

3.2.3.2 Electrochemical Impedance Spectroscopy

In addition to the aforementioned direct current voltage response test, electrochemical impedance spectroscopy (EIS) is often used to characterize the cell impedance. It has the advantages that the cell impedance can be measured at different frequencies in a relatively short period and the cell SoC will not be altered.

In the measurement, a sinusoidal current signal is brought to a LIC and the characteristic voltage response is recorded, which is named as the galvanostatic EIS. The input signal can also be voltage and thus current as output, which is named as the potentiostatic EIS. The impedance $Z(f)$ is expressed as follows:

$$Z(f) = \frac{u(f)}{i(f)} = \frac{\hat{U} \cdot e^{j(2\pi ft + \varphi_u)}}{\hat{I} \cdot e^{j(2\pi ft + \varphi_i)}} = |Z(f)| \cdot e^{j\varphi} \quad (18)$$

$$|Z(f)| = \frac{\hat{U}}{\hat{I}} \quad (19)$$

$$\varphi = \varphi_u - \varphi_i \quad (20)$$

$u(f)$ is the voltage signal, $i(f)$ is the current signal, t is the time, \hat{U} is the voltage signal amplitude, \hat{I} is the current signal amplitude, f is the frequency and φ is the phase shift.

The impedance can be divided into a real part $Re\{Z\}$ and an imaginary part $Im\{Z\}$. The real and imaginary parts can be plotted in one graph with the change of the frequency, namely the Nyquist plot. Fig. 15 presents the Nyquist plot of a fresh Kokam cell of 50% SoC at 25°C. The measurement details are depicted in Chapter 4. The plot can be separated into five parts according to the frequency range. These five parts correspond to different components or processes inside a LIC. Furthermore, the ohmic resistance R_{ohm} and the sum of the SEI layer

resistance R_{SEI} and the charge transfer resistance R_{ct} can be obtained. The separation of R_{SEI} and R_{ct} is troublesome, since the boundary frequency changes or blurs with aging.

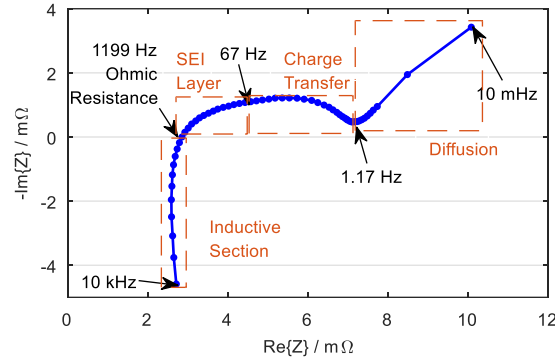


Figure 15. The Nyquist plot of a fresh Kokam cell of 50% SoC at 25°C.

Inductive Section

The inductive section of the Nyquist plot, where $-Im\{Z\}$ is negative, has once been mistakenly attributed to the formation of SEI [148, 149]. However, a recent study [150] have experimentally disproven the interrelationship between the inductive section and the SEI. Instead, the inductances in LICs originate from the metallic elements between the electrode paste and the measuring equipment, including the wiring and the current collectors [146, 147, 150, 151]. Consequently, active material changes during the LIC aging process have little influence on this part. An RL element in the ECM (Fig. 14) is applied to characterize this part.

Ohmic Resistance

The ohmic resistance is approximately the real part of the impedance where $Im\{Z\}$ equals zero, i.e., at the intersection of the Nyquist plot with the real axis in Fig. 15. At this point, the inductive behavior of partial LIC elements is wholly compensated by the capacitive behavior of other LIC elements [152]. The ohmic resistance stands for the resistance sum of the current collectors, the active materials, the electrolyte and the separator [146, 147]. The Kokam cell in Fig. 15 shows pure ohmic behavior at a frequency of approximately 1199 Hz. Nonetheless, this pure ohmic frequency varies from 1060 Hz to 1500 Hz among all the fresh Kokam cells from the same charge under the same test conditions.

SEI Layer & Charge Transfer

In the middle part of the Nyquist plot, from 1199 Hz to 1.17 Hz, two superimposed semi-circles are observed. According to the literature, the semi-circle at higher frequencies originates largely from the anode and is ascribed to the SEI layer [146, 152–157], while the semi-circle at medium frequencies represents mainly the double layer capacity and the charge transfer resistance of the cathode [147, 154, 158, 159]. One or more RC-elements in the ECM are employed to interpret this frequency range.

Diffusion

Below 1.17 Hz the impedance is characterized by a 45° slope, representing the diffusion hindrance of lithium ions into/out the active material and within the electrolyte. The slope is primarily attributed to solid state diffusion [148, 160]. This process is commonly described with a Warburg element [153, 160–162]. Conventional aging processes have little influence on the diffusion tail.

Influence Factors of EIS Measurement

In order to use EIS as a reliable aging detection tool for LICs, it should firstly be clarified, which factors can influence the EIS results besides aging. In an electrochemical system such as the LIC, SoC and temperature have major influences on the impedance.

Fig. 16 shows the influence of SoC and temperature on the Nyquist plot of a fresh Kokam cell. At 0% and 20% SoCs, the cell has a much higher resistance in the area of SEI layer and charge transfer. For SoC higher than 40%, there is only a slight difference in their Nyquist plots. Besides, SoC has little influence on the ohmic resistance. Temperature plays a crucial role in the development of the Nyquist plots. The two superimposed semi-circles increase largely with temperatures below 25°C. The ohmic resistance almost doubles from 40°C to 0°C. Temperature has a great influence on the electrolyte conductivity.

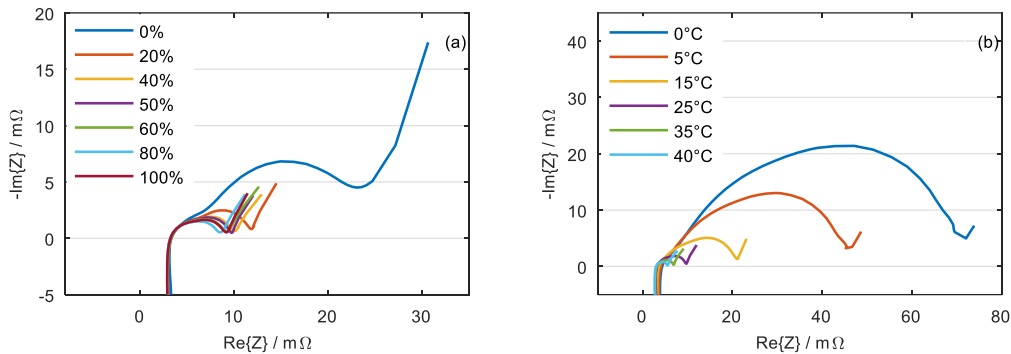


Figure 16. The Nyquist plot evolution of a fresh 5 Ah Kokam cell with the same test plan (a) of different SoCs; (b) at different temperatures.

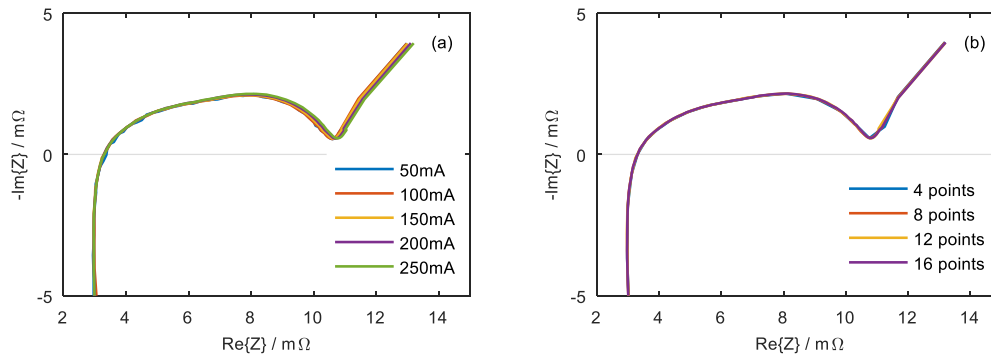


Figure 17. The Nyquist plot evolution of a fresh 5 Ah Kokam cell with (a) different current amplitudes; (b) different combinations of points per decade.

During the measurement, parameters like current amplitude and points per decade may also cause difference in the EIS results. Fig. 17 presents the influence of the two parameters on the Nyquist plot. Details of the parameters are introduced in Section 4.2. In Fig. 17 (a), only the current amplitudes of Stage I and II are changed. From an amplitude of 50 mA to 250 mA, only minor increase in the semi-circle at medium frequencies is observed. In Fig. 17 (b), points per decade of Stage I and II are adjusted to “4 points – 2 points”, “8 points – 6 points”, “12 points – 10 points” and “16 points – 14 points” (see Appendix I A.2). The adjustment of points per decade makes little difference to the Nyquist plot.

3.2.4 Temperature-Based Aging Detection

LIC generates heat during charge and discharge. The heat generation consists mainly of reversible heat and irreversible heat. The former relies on the LIC entropy change and the current. The latter depends on the LIC resistance and the current. Both entropy change and resistance vary with LIC degradation, which is the basis of all the temperature-based aging detection methods in literature.

Maher and Yazami [163–165] developed electrochemical thermodynamics measurements to determine the evolution of entropy change in a LCO/graphite LIC during storage and cycling tests. It has been found that cycle life aging leads to severe crystal structure degradation in the LCO cathode by analyzing the entropy change profiles. Calorimeters were employed by researchers [166–168] to quantify the heat flow difference between aged and unaged LICs during the same operation. Differential thermal voltammetry was introduced by the Offer group [169–171] as a diagnostic technique for LICs. It presents equivalent information to slow rate cyclic voltammetry measurements and provides additional temperature information. There are major limitations of these detection methods. A complete entropy change measurement covering the whole SoC range takes normally several weeks. Furthermore, an excellent climate chamber is required to keep the temperature accurate and stable. A calorimeter is an expensive piece of laboratory equipment. Based on thermodynamics and literature survey, a novel aging detection method based on temperature measurement is put forward in this thesis. It correlates the LIC SoH with a temperature variation minimum during charge. The theoretical background is clarified in the following subsections and the validation is in Section 5.4.

3.2.4.1 Intercalation Entropy

Anode and cathode materials of LICs are capable of storing and extracting lithium ions, causing few crystalline structure changes in them. In these two processes, i.e., intercalation and deintercalation, heat is generated or absorbed [172]. Entropy change is employed to describe this thermal effect. If the chemical reaction is 100% reversible, the entropy changes by intercalation and deintercalation have the same value but the opposite sign.

Entropy Change of the Full Cell

As explained in Eq. 1, the OCV of a full cell is the potential difference of its electrodes. The potential of the electrode depends on its lithiation degree or its own SoC, which distinguishes from the full cell SoC due to anode over dimension and electrode offset, as explained in Subsection 3.2.2.1. Eq. 1 can be thus rewritten into the following equation with respective SoCs:

$$U_{OCV}(SoC) = U_{ca}(SoC_{ca}) - U_{an}(SoC_{an}) \quad (21)$$

The electrical work, which equals the change in Gibbs free energy ΔG , can be expressed as follows.

$$\Delta G_{T,p} = -nFU_{OCV} \quad (22)$$

Here, n is the number of exchanged electrons and F is the Faraday constant (96484.6 C/mol). The subscripts T and p means that the equation is true for constant temperature and pressure.

The change of Gibbs free energy of a system is a function of enthalpy change ΔH , entropy change ΔS and temperature T in Eq. 23. By differentiation, the entropy change can be expressed in Eq. 24 [173].

$$\Delta G_{T,p} = \Delta H - T\Delta S \quad (23)$$

$$\Delta S = -\left(\frac{\partial \Delta G}{\partial T}\right)_p = nF\left(\frac{\partial U_{OCV}}{\partial T}\right)_p \quad (24)$$

Combining Eq. 21 and Eq. 24, the entropy change of the full cell is the difference of the entropy changes of both electrodes [174].

$$\Delta S(SoC) = \Delta S_{ca}(SoC_{ca}) - \Delta S_{an}(SoC_{an}) \quad (25)$$

Entropy Change of the Anode

The entropy change of graphite during lithium intercalation has been measured in literature [125, 175–178] and one of the measurement results is displayed in Fig. 18. The lithiation of graphite can be expressed with the following reaction:



The entropy change of this reaction is described as follows [124]:

$$\Delta S(x) = nF\left(\frac{\partial U_{an}}{\partial T}\right)_x \quad (27)$$

$\Delta S(x)$ is the reaction entropy change at a lithiation degree of Li_xC_6 .

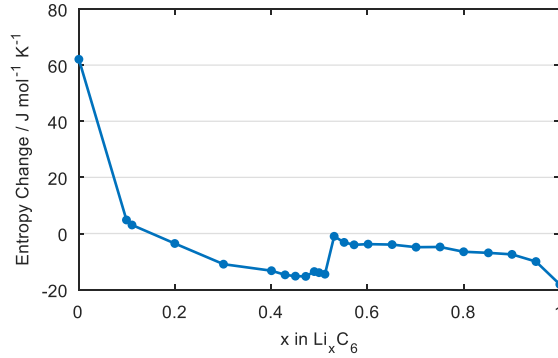
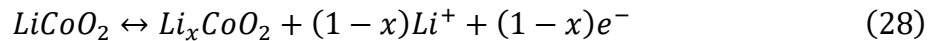


Figure 18. Entropy change of graphite during lithium intercalation [175].

According to literature [128, 179, 180], lithium intercalation into graphite occurs in an ordered way, which is referred to as staging. The following intercalation stages are known from graphite to LiC_6 : dilute stage-1, stage-4, stage-3, liquid-like stage-2 (2L), ordered stage-2 and ordered stage-1 [125]. The entropy change also follows the staging process. The graphite has an ordered structure. Initial lithium intercalation brings disorder into the graphite structure and thus positive entropy change in the lithiation range of graphite to $\text{Li}_{0.15}\text{C}_6$. Due to numerous equivalent sites for lithium atoms at the beginning, the configurational entropy is large. When the lithium concentration rises to $x > 0.2$, the compounds experience the transition from more disordered stage-2L to ordered stage 2 ($\text{Li}_{0.5}\text{C}_6$), which improves the ordering of the structure. Hence, the entropy change is negative between $\text{Li}_{0.13}\text{C}_6$ and $\text{Li}_{0.5}\text{C}_6$. At $\text{Li}_{0.5}\text{C}_6$, there is a sharp peak in the entropy change reaching almost 0 J/mol/K. It is believed to be caused by a change in the vibrational entropy [125, 175]. Afterwards, the entropy change stays below zero during the transition from stage-2 ($\text{Li}_{0.5}\text{C}_6$) to more ordered stage-1 (LiC_6). The transitions stage-2L \rightarrow stage-2 and stage-2 \rightarrow stage-1 are first-order phase transitions [77], therefore, the entropy change forms two plateaus accordingly [125, 181].

Entropy Change of the Cathode

In Ref. [178], the entropy change profiles of several conventional LIC cathodes are presented. Compared to other cathodes, LCO has the most pronounced entropy change as shown in Fig. 19. The delithiation of LCO follows the reaction in Eq. 28, where $0.5 < x < 1$.



According to literature [165], from LiCoO_2 to $\text{Li}_{0.5}\text{CoO}_2$, the cathode goes through the following phase transitions: (1) single phase hexagonal (O3I) \rightarrow two-phase (O3I+O3II) at $\sim \text{Li}_{0.95}\text{CoO}_2$; (2) two-phase (O3I+O3II) \rightarrow single phase (O3II) at $\sim \text{Li}_{0.875}\text{CoO}_2$; (3) single phase (O3II) \rightarrow single monoclinic phase at $\sim \text{Li}_{0.65}\text{CoO}_2$; (4) single monoclinic phase \rightarrow hexagonal phase (O3II') at $\sim \text{Li}_{0.6}\text{CoO}_2$; (5) hexagonal phase (O3II') \rightarrow hexagonal phase (O3) at $\sim \text{Li}_{0.55}\text{CoO}_2$.

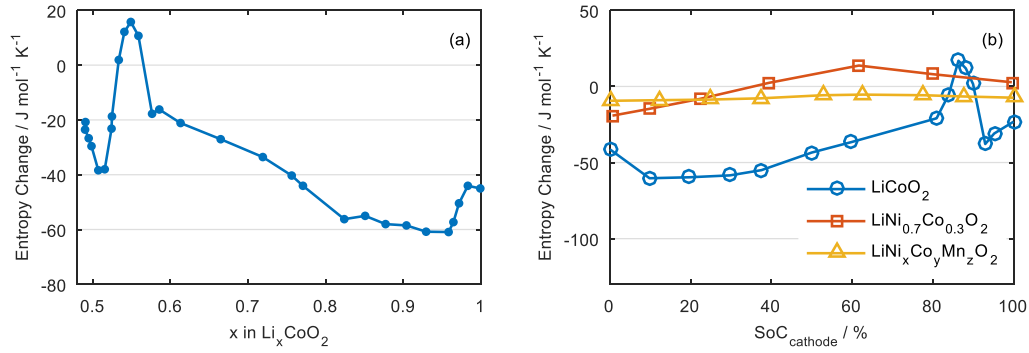


Figure 19. (a) Entropy change of LCO [176]; (b) comparison of entropy changes of various cathodes [178] during lithium deintercalation.

The examined Kokam cell has a graphite anode and a LCO/NCA blended cathode. Since no entropy change data of pure NCA has been found in literature, the entropy changes of LiNi_{0.7}Co_{0.3}O₂ (NCO) and LiNi_xCo_yMn_zO₂ (NMC) are displayed in Fig. 19 (b) instead. Due to similar crystal structure and composition between NCA, NCO and NMC, it is assumed that the entropy change of NCA should be comparable with the entropy changes of NCO and NMC. The entropy change curves of NCO and NMC from Fig. 19 (b) are both relatively flat compared to that of LCO and vary between -20~15 J/mol/K. The entropy change curve of NCA is believed to be quite flat and varies within the same range.

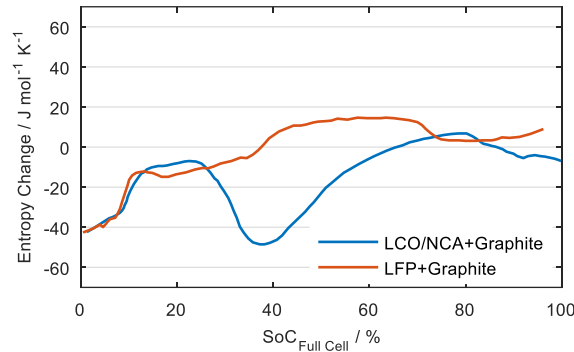


Figure 20. Entropy change curves of a Kokam cell with an LCO/NCA cathode and an A123 cell with an LFP cathode [182].

The entropy change of a LIC from the same manufacturer (Kokam) is found in Ref. [182] and shown in Fig. 20. It consists of a graphite anode and a LCO/NCA blended cathode, which is believed to be the same as the experimental cell in this thesis work. Fig. 20 shows the entropy change curves of the literature Kokam cell and an A123 cell with a graphite anode and a LFP cathode. In spite of different cathode materials, both curves in Fig. 20 are almost identical in the beginning 10% SoC, which implies the dominant influence from the graphite anode in this area [164]. As shown in Fig. 18, there is indeed a pronounced entropy change in graphite at the beginning of lithiation. The Kokam entropy change curve has a minimum at around 38% SoC of the full cell. This entropy change minimum does not occur in the A123 cell, indicating that

it is a characteristic of the LCO/NCA blended cathode. However, compared to Fig. 19 (b), there is no such entropy change minimum in LCO, NCO or NMC at 38% SoC.

The entropy change calculation of a blended cathode from its composite materials has not been found in literature. In Subsection 2.2.3, it is known that the potentials for both composite materials are approximately identical when the current is low. With the potential curves of pure LCO and pure NCA from literature [142], the potential curve and the deintercalation behavior of the blended cathode can be calculated. The blended cathode consists of 44% LCO and 56% NCA (percentage based on the capacity). Hence, the potential curve of the blended cathode versus its SoC can be calculated discretely as follows:

$$\Delta SoC_{ca}(\Delta U_{ca}) = 44\% * \Delta SoC_{LCO}(\Delta U_{ca}) + 56\% * \Delta SoC_{NCA}(\Delta U_{ca}) \quad (29)$$

Fig. 21 (a) shows the potential curves of LCO, NCA, the calculated blended cathode (LCO+NCA) and the measured blended cathode. The dot-dash line stands for the measured potential curve of the blended cathode, which is attained from half cell measurements. The calculated cathode potential curve agrees well with the measured one. In Fig. 21 (b), SoC_{LCO} and SoC_{NCA} are plotted against SoC_{ca} . It suggests that, in the beginning 30% SoC_{ca} during charge, all lithium ions are extracted out of NCA due to its low working potential and LCO is unused. At around 30% SoC_{ca} or a cathode potential of 3.8 V, lithium ions start to be drawn out of LCO at a considerably rapid speed owing to the LCO potential plateau, which also forms the potential plateau of the blended cathode. Above 3.8 V, lithium ions deintercalate from both cathode components simultaneously.

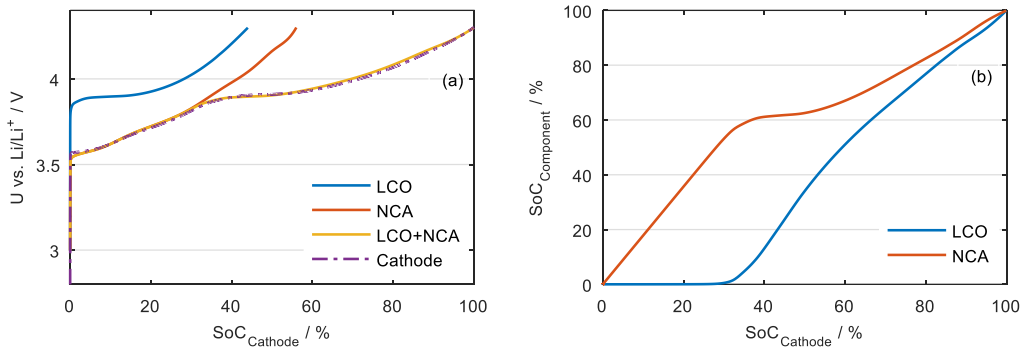


Figure 21. (a) Potential curves of LCO, NCA [142], the calculated blended cathode LCO+NCA and the measured blended cathode; (b) SoC evolution of LCO and NCA versus the SoC of the blended cathode [9].

In order to determine the current distribution in both cathode components, a Matlab *Simscape* model is designed in Fig. 22. The parameters applied in the model are listed in Tab. 4. Besides the assumed constants, potential-DoD values of LCO and NCA from Fig. 21 (a) are imported separately into the *Lookup Tables* in the model (with $DoD=1-SoC$).

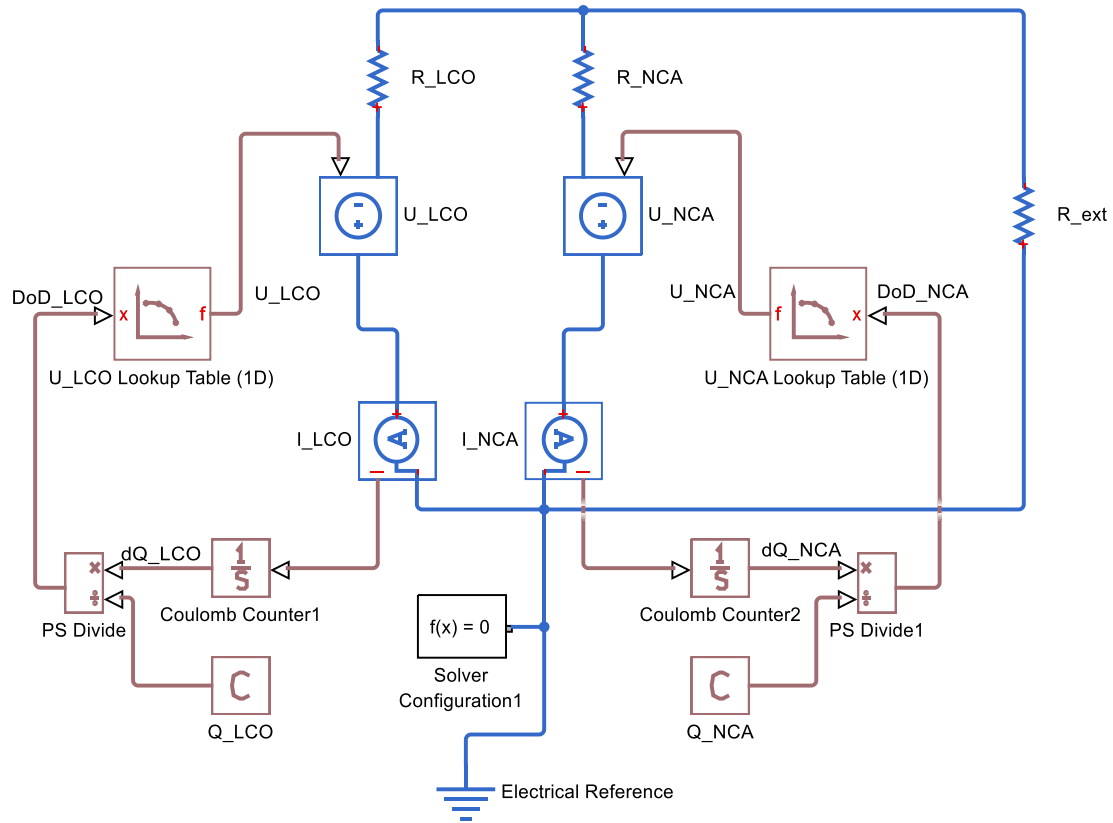


Figure 22. A Matlab *Simscape* model used to determine the current distribution in both cathode components.

Table 4. Parameters for the Matlab *Simscape* model.

Parameter	Definition	Value
R_{LCO}	LCO Resistance	1.5 m Ω
R_{NCA}	NCA Resistance	1.5 m Ω
R_{ext}	External Resistance	0.66 Ω
Q_{LCO}	LCO Capacity	2.508 Ah
Q_{NCA}	NCA Capacity	3.192 Ah
DoD_{LCO}	LCO DoD	Calculated by Q_{LCO} and integrated Current I_{LCO}
DoD_{NCA}	NCA DoD	Calculated by Q_{NCA} and integrated Current I_{NCA}
U_{LCO}	LCO Potential	Calculated by DoD_{LCO} via <i>Lookup Table</i>
U_{NCA}	NCA Potential	Calculated by DoD_{NCA} via <i>Lookup Table</i>

*Parameter values are comparable to a Kokam cell with a capacity of 5.7 Ah and an ohmic resistance of 3 m Ω .

The current distribution can be expressed in the following equation.

$$I = I_{\text{LCO}} + I_{\text{NCA}} = \alpha * I + (1 - \alpha) * I \quad (30)$$

The current distribution in both components according to the Matlab *Simscape* model is shown in Fig. 23 (a) and the current distribution coefficient α in Fig. 23 (b).

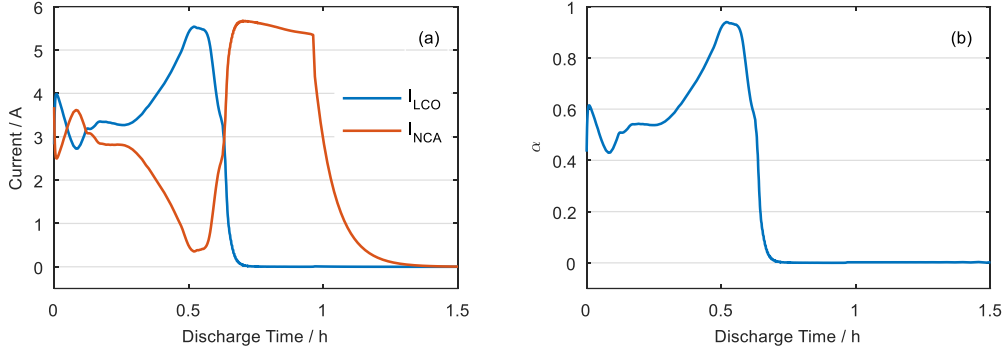


Figure 23. (a) The simulated current distribution I_{LCO} and I_{NCA} in both cathode components with discharge time; (b) the simulated current distribution coefficient α with discharge time.

The entropy change of the blended cathode can be expressed with the current distribution coefficient α as well.

$$\Delta S_{\text{ca}} = \alpha * \Delta S_{\text{LCO}} + (1 - \alpha) * \Delta S_{\text{NCA}} \quad (31)$$

Based on Eq. 30 and Eq. 31, the entropy change of the blended cathode is calculated and presented in Fig. 24 (a), where NCA entropy change is replaced with NCO entropy change. Since the current distribution coefficient decreases to zero near the end of discharge and LCO has a much lower entropy change than NCO, an entropy change minimum appears at about 40% SoC_{ca} in the calculated LCO+NCO entropy change curve. In the area where α drops to zero, there is an abrupt jump of the entropy change of LCO+NCO.

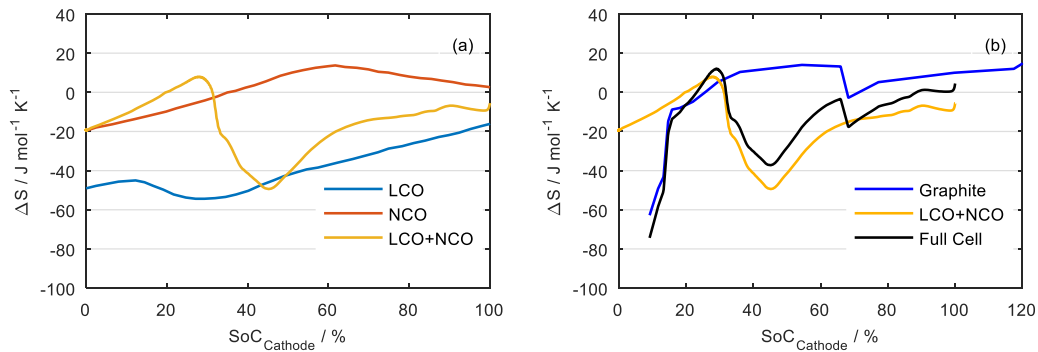


Figure 24. (a) Entropy change curves of LCO, NCO and the calculated blended cathode; (b) entropy change curves of graphite, the calculated blended cathode and the calculated full cell [9, 178].

Comparing to Fig. 21 (b), since no de-/intercalation reaction takes place in LCO in the beginning 30% SoC_{ca} , there is no reaction entropy change contribution from LCO. The entropy change of the blended cathode in this SoC_{ca} range depends merely on the entropy change of the

NCA. In the SoC_{ca} range of 30% to 100%, there are de-/intercalation reactions in both cathode components. Thus, the entropy change of the blended cathode is a mixture of the entropy changes of LCO and NCA [183].

In Fig. 24 (b), the inverse of the graphite entropy change from Fig. 18 is employed to determine the full cell entropy change. The graphite anode is 1.133 times oversized compared to the blended cathode and has an initial offset of 9.2% SoC_{ca} [5]. The entropy change minimum of the full cell explains the origin of the entropy change minimum for the Kokam cell in Fig. 20. The calculated entropy change of the full cell in Fig. 24 (b) does not agree perfectly with the entropy change curve in Fig. 20, but it shows a similar tendency.

This entropy change minimum may appear in other lithium ion cells with blended electrode, where the electrode components show prominent difference in their operation potentials.

3.2.4.2 Heat Generation

The charge and discharge processes of a LIC are accompanied with heat generation, including the Joule heat \dot{Q}_{jou} , the reversible reaction heat \dot{Q}_{re} , the side reaction heat \dot{Q}_{sr} and the mixing heat \dot{Q}_{mix} [184]. These four heat generation terms can be expressed in the following equation [185]:

$$\dot{Q} = \dot{Q}_{\text{jou}} + \dot{Q}_{\text{re}} + \dot{Q}_{\text{sr}} + \dot{Q}_{\text{mix}} \quad (32)$$

During one charge/discharge process, the degradation rate of a commercial LIC is considerably low [186]. Consequently, the side reaction heat can be neglected. The mixing heat due to concentration gradients inside the LIC is prominent under dynamic cycling conditions. By constant current charging/discharging with 1C, which is the case in my experimental work, the mixing heat can be also ignored [181, 185]. Accordingly, Eq. 32 can be simplified as follows:

$$\dot{Q} = \dot{Q}_{\text{jou}} + \dot{Q}_{\text{re}} = I(U_{\text{OCV}} - U_t) - IT \frac{\partial U_{\text{OCV}}}{\partial T} \quad (33)$$

\dot{Q} is the total heat generation rate (+ for heat generation; - for heat consumption), I is the current (+ for discharge; - for charge), U_{OCV} is the OCV, U_t is the terminal voltage, T is the cell temperature.

Under constant current operation circumstances, the Joule heat can be approximately given by:

$$\dot{Q}_{\text{jou}} = I^2 R \quad (34)$$

where R is the battery internal resistance during charge/discharge.

The reversible reaction heat can be expressed with entropy change as follows [125, 176, 178]:

$$\dot{Q}_{\text{re}} = - \frac{IT}{nF} \Delta S \quad (35)$$

Where n is the number of electrons per reaction, F is the Faraday constant and ΔS is the entropy change of the LIC.

The total heat generation in Eq. 32 is then transformed into Eq. 36:

$$\dot{Q} = I^2 R - \frac{IT}{nF} \Delta S \quad (36)$$

The Biot number is an index of the ratio of the heat transfer resistance inside of and at the surface of a body. It is defined as [187]:

$$Bi = \frac{hL_C}{k_b} \quad (37)$$

where h is the surface heat transfer coefficient; L_C is the characteristic length, which equals the quotient of the body volume and the body surface area; k_b is the thermal conductivity of the body.

If the Biot number is smaller than 0.1, the temperature inside the body can be considered as uniform [187]. In our case, the cell is a pouch cell with a L_C of 0.0057 m. The cross-plane thermal conductivity $k_b=3.4 \text{ Wm}^{-1}\text{K}^{-1}$ is obtained from literature [188]. A forced convection is applied to the cell in a climate chamber at 25°C. The heat convection coefficient $h=24.927 \text{ Wm}^{-2}\text{K}^{-1}$ is extracted from literature [185]. With all the conditions, a Biot number of 0.042 is calculated for the cell, which is smaller than 0.1. Therefore, the pouch cell can be considered to have a homogenous internal temperature distribution during the operation.

The temperature variation rate dT/dt of a cell can be expressed in Eq. 38. The temperature is influenced by the Joule heat, the reaction heat and the heat dissipation to the environment.

$$\frac{dT}{dt} = \frac{\dot{Q}}{mc_p} - \frac{hA}{mc_p} (T - T_{\text{env}}) \quad (38)$$

Combining Eq. 36 and Eq. 38, the temperature variation rate can be calculated with Eq. 39:

$$\frac{dT}{dt} = \frac{1}{mc_p} \left(I^2 R - \frac{IT}{nF} \Delta S \right) - \frac{hA}{mc_p} (T - T_{\text{env}}) \quad (39)$$

where m is the cell mass, c_p is the cell heat capacity, h is the heat convection coefficient, A is the cell surface area, T_{env} is the environmental temperature. When the cell temperature change is limited ($<5^\circ\text{C}$), c_p and h could be assumed as constant [185, 189].

3.2.4.3 Cell Resistance Evolution

In Eq. 39, entropy change ΔS varies with SoC. Resistance R may also vary with SoC. In order to exclude the SoC influence on R , the following resistance aging results of the experimental cell are shown in advance.

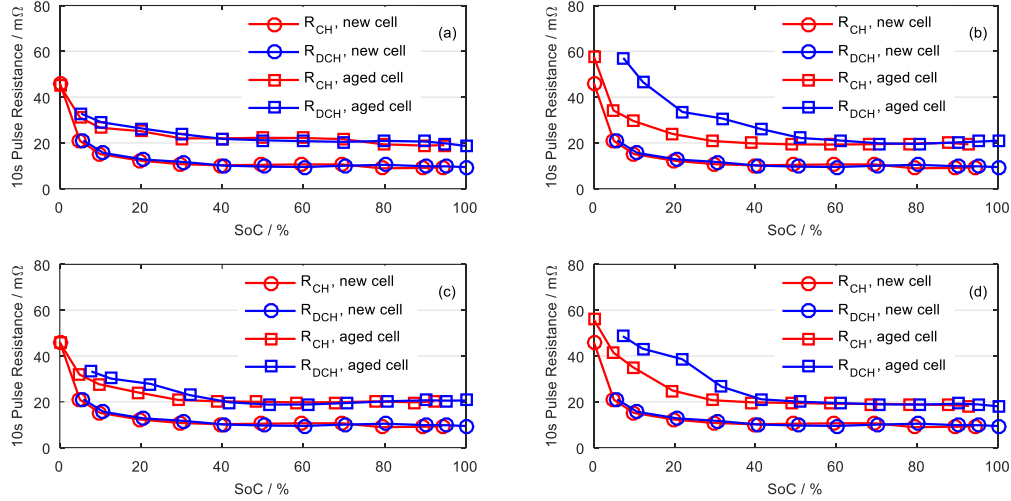


Figure 25. 10s-charge/discharge pulse resistance of a new cell and an aged cell (a) stored at 55°C; (b) 1C cycled at 25°C; (c) 3C cycled at 25°C; (d) 5C cycled at 25°C. R_{CH} : 10s-charge pulse resistance at 1C; R_{DCH} : 10s-discharge pulse resistance at 1C [9].

The employed resistance R is a 10s-charge/discharge resistance from the pulse test. Fig. 25 shows the 10s-pulse resistances of a new cell and an aged cell under four different aging conditions. The SoH of the aged cell in Fig. 25 (a) is 85%. The other aged cells in Fig. 25 (b)-(d) have SoHs below 80%.

In the new cell, the charge and discharge resistances are almost identical. They are considerably higher in the range of 0-20% SoC. Above 20% SoC, both resistances stay almost constant. In Fig. 25 (a) and (c), the charge and discharge resistances of the aged cells have increased to the same extent. Both resistances keep nearly constant over the SoC range of 20-100%. As for the aged cells in Fig. 25 (b) and (d), the discharge resistance has increased more than the charge resistance. However, the charge resistance can still be considered as constant above 20% SoC. Therefore, in the SoC range of 20-100% during charge, temperature variation rate dT/dt is an indicator for entropy change ΔS . The entropy change minimum shown in Fig. 20 should be visible on the dT/dt curve during CC charge. The dT/dt curve evolution can be thus used to detect LIC aging. This assumption will be proven in Section 5.4.

4. Experimental and Test Methods

To investigate the impact of various stress factors on aging and the corresponding aging detection, lithium-ion pouch cells of the type Kokam SLPB50106100 with a nominal capacity of 5 Ah were examined. In this chapter, the basic cell information is introduced and the test profiles are presented in detail.

4.1 Investigated Cell

The examined cells were purchased from the manufacturer Kokam with *Technical Specification* in Ref. [190]. Fig. 26 shows one cell and its geometry. Tab. 5 shows the cell specifications provided by the manufacturer. According to Tab. 5, 5 A is recommended as 1C. The cell should be operated between 2.7 V and 4.2 V.

Table 5. Basic information of Kokam SLPB50106100 from the manufacturer [190].

Parameter	Value	Comment
Rated Capacity	Typ. 5.5 Ah	Charge at 0.2C (1.0 A)
	Min. 5.0 Ah	Discharge at 0.5C (2.5 A)
Nominal Voltage	3.7 V	
Lower Limit Voltage	2.7 V	
Upper Limit Voltage	4.2 V \pm 0.03 V	
Maximal Continuous Charge Current	10 A	
Maximal Continuous Discharge Current	25 A	
Operation Temperature Range	Charge: 0~45°C	
	Discharge: -20~60°C	
Storage Temperature Range	\leq 1 year: -20~25°C	SoC 50 \pm 5%
	\leq 3 months: 25~40°C	

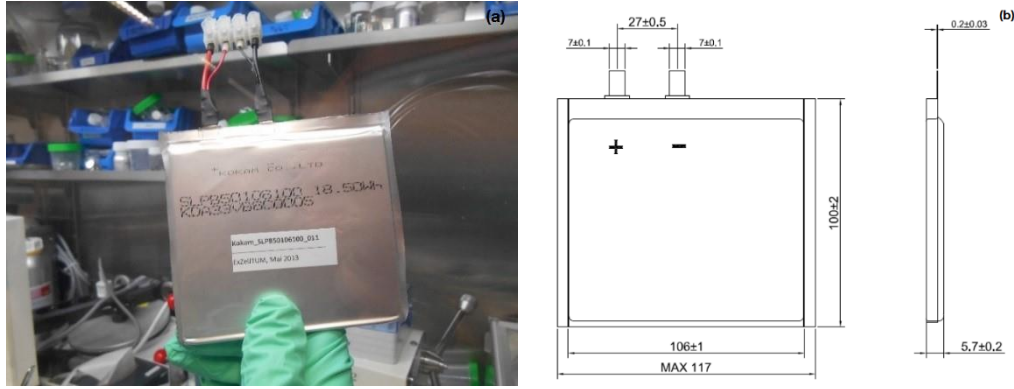


Figure 26. (a) A Kokam SLPB50106100 pouch cell; (b) cell geometry in mm [190].

4.1.1 Cell Variation

After receiving the 90 Kokam cells, weight tests, capacity tests and resistance tests were immediately carried out to check the quality of the cells. The capacity measurement and the 30 min direct current (DC) relaxation resistance ($R_{DC_30min_Relax}$) measurement are described in Subsection 4.2. The ohmic resistance, i.e., 1 kHz alternating current (AC) resistance (R_{AC_1kHz}), is obtained with a Hioki BT3562 Battery HiTester at room temperature. The cell variation histograms regarding weight, capacity, AC resistance and DC resistance are presented in Fig. 27. They show slight normal distribution, but the sample size (90) is not large enough to assess any statistical distribution. The cells have a good quality and the arithmetic means and deviations are listed in Tab. 6.

Table 6. Overview of the cell parameter variation.

Parameter	Arithmetic Mean	Deviation
Cell Weight	119.548 g	+0.34% / -0.29%
Cell Capacity	5.759 Ah	+0.57% / -0.44%
AC Resistance at 1 kHz	2.646 m Ω	+7.07% / -4.63%
DC Resistance of 30 min Relaxation	17.17 m Ω	+3.73% / -10.02%

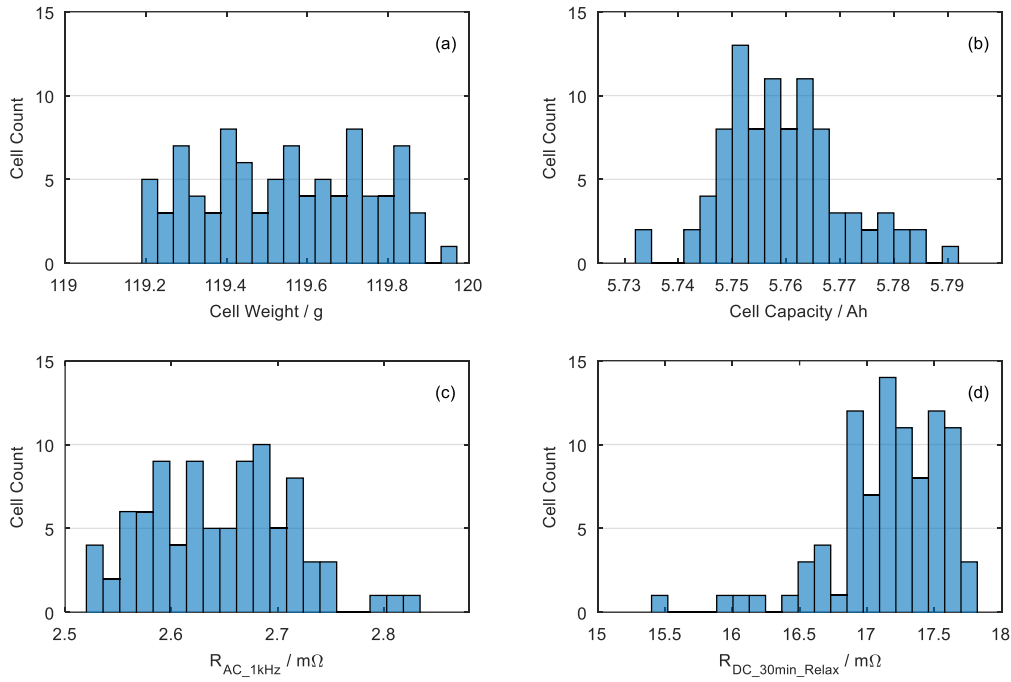


Figure 27. Overview of histograms of (a) cell weight; (b) cell capacity; (c) AC resistance at 1 kHz; (d) DC resistance of 30 min relaxation.

4.1.2 Capacity Rate Test

Three cells were tested with several C-rates to determine their charge and discharge rate capability. The three cells show comparable behavior and thus only the results of one cell is representative and displayed in Fig. 28. With a CV step, the same capacity can be charged into or discharged out of the cell with different C-rates. However, for the CC step, the discharge capacity decreases with the C-rate, which can be described with Peukert's law.

$$t \cdot I^k = c \quad (40)$$

Here t is the time to CC discharge the cell, I is the CC discharge current in A, c is a constant and $k \geq 1$ is the dimensionless Peukert constant.

Eq. 40 can be reformulated as follows:

$$Q = I \cdot t = \frac{c}{I^{k-1}} \quad (41)$$

Here Q is the discharge capacity of a cell at the current I .

If the discharge capacity of a cell is known as Q_1 at the current I_1 , then the discharge capacity Q_2 of the cell at a different current I_2 can be calculated as follows:

$$Q_2 = I_2 \cdot t_2 = \frac{c}{I_2^{k-1}} = \frac{I_1^k \cdot t_1}{I_2^{k-1}} = \left(\frac{I_1}{I_2}\right)^{k-1} \cdot Q_1 \quad (42)$$

According to the measurement in Fig. 28 (b), a Peukert constant of 1.0184 is obtained for the tested cell discharged with 1C, 3C and 5C at 25°C. It is a relatively low Peukert constant for LICs, which means the experimental cell has a good discharge rate capability.

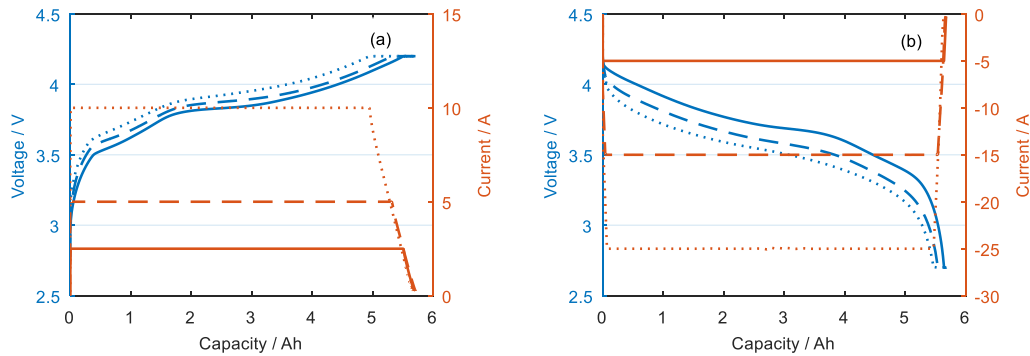


Figure 28. (a) Charge rate test at 0.5C, 1C and 2C with CV phases; (b) discharge rate test at 1C, 3C and 5C with CV phases.

4.1.3 Electrode Material Identification

In order to identify the electrode material, a fresh cell was disassembled and its electrodes were investigated with SEM. Fig. 29 shows the SEM images of both electrodes. The cathode SEM image shows that it consists of two types of particles. With the help of energy-dispersive X-ray (EDX), the multi-domain particle is identified as NCA and the single-domain particle is LCO.

Since EDX only measures the element composition of one spot on the electrode surface, it is not able to give information on the LCO/NCA ratio in the bulk cathode material. The anode SEM image shows typical graphite layer structure. It is further confirmed by the anode half cell potential curve in Fig. 34 (b), which shows graphite staging plateaus. The details of the half cell measurements are presented in Subsection 4.4.

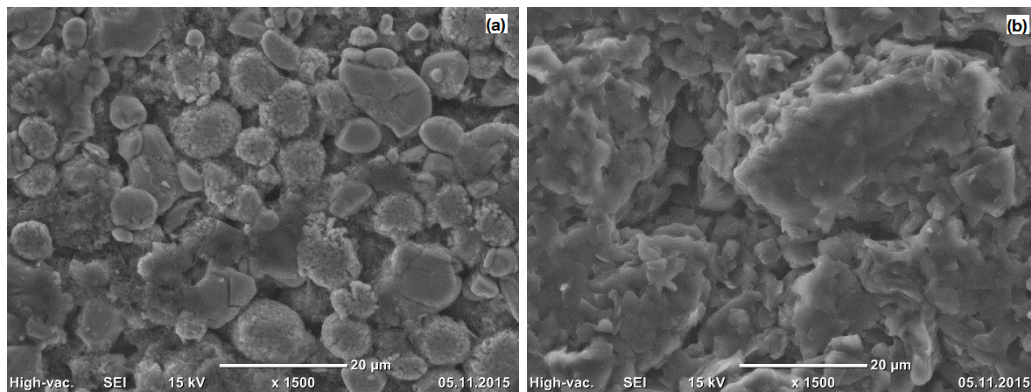


Figure 29. SEM images of the (a) cathode and (b) anode surface of a fresh Kokam cell.

4.2 Performance Test Methods

In our aging experiment, performance tests were carried out periodically to check the aging condition of the cells. At the beginning of each performance test, there is a 2 h pause for

stabilization. The performance tests were divided into basic performance tests and extended performance tests as shown in Fig. 30. The basic performance test, i.e., the capacity test, was carried out every two weeks and took 8 h each time. At the end of each basic performance test, $R_{DC_30min_Relax}$ can be calculated in the 30 min relaxation.

$$R_{DC} = \frac{\Delta U_{30min}}{\Delta I_{30min}} \quad (43)$$

The extended performance test, including a capacity test and an OCV test, was conducted every four weeks and at the very beginning/end of the aging test. Six hours after each extended performance test, an EIS test was performed to check the impedance change of the cell. The extended performance test along with the successive EIS test took almost 48 h.

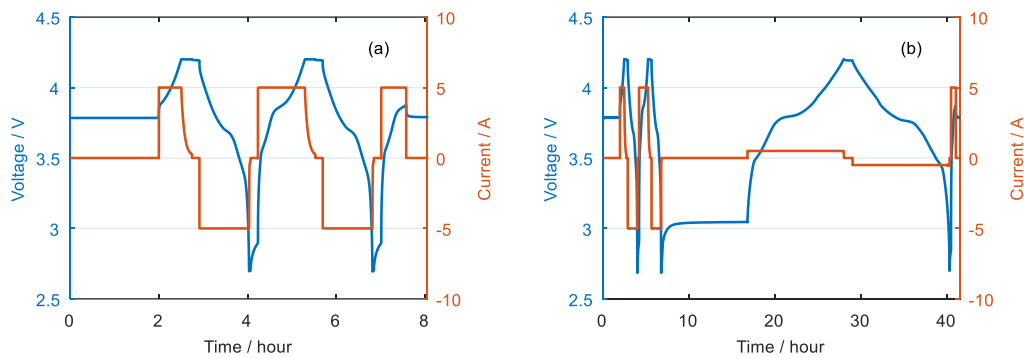


Figure 30. (a) The basic performance test and (b) the extended performance test.

Cycling tests, basic performance tests and extended performance tests were all conducted with a Cell Test System by BaSyTec. EIS tests were done on a potentiostat VMP3 by Biologic Science Instruments. All the tests were performed in climate chambers at 25°C. A negative temperature coefficient (NTC) thermistor from EPCOS AG was attached to the surface center of each cell to record the real surface temperature during the performance tests (see Fig. 31). The NTC thermistor has a resistance tolerance within $\pm 1\%$ between 0°C to 60°C. The measurement was intended for temperature analysis as well as protection against cell overheating during the test. The cells were tested under regular atmospheric pressure.

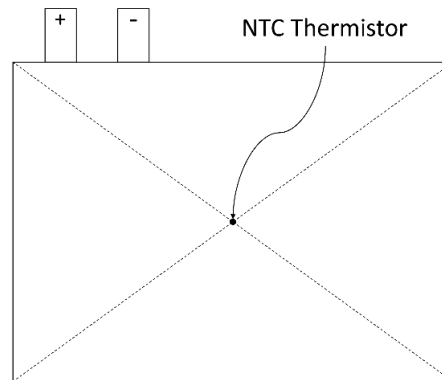


Figure 31. Schematic of a tested pouch cell and the position of the NTC thermistor [9].

In the laboratory, two kinds of capacity values are usually compared. One is measured by a constant current (CC) discharge, which is dependent on the current intensity and the internal resistance of the LIC. The other is measured by a CC discharge and a consecutive constant voltage (CV) discharge cut off by a very low current. This CC-CV capacity is approximately unaffected by the CC current intensity or the LIC internal resistance. It stands for the amount of the total cyclable lithium inventory in a LIC.

In the capacity test, the remaining capacity was measured as follows. Cells were charged with 1C CC to 4.2 V and then switched to a CV phase at 4.2 V. When the current dropped below 0.05C in the CV phase, cells were considered as 100% charged. After a pause of 10 min, a CC of 1C was applied to discharge the cells to 2.7 V, followed by a CV phase to further discharge the cell until the current fell below 0.05C. The purpose of this CV phase was to minimize the influence of impedance rise in the cells on the measured capacity.

Table 7. EIS test plan in three stages.

	Stage I	Stage II	Stage III
Frequency Range	100 kHz ~ 2.1 Hz	1.93 Hz ~ 100 mHz	90 mHz ~ 10 mHz
Points per Decade (logarithmic spacing)	12	10	3
Current Amplitude	200 mA	200 mA	100 mA

The OCV tests were always started 10 h after the preceding capacity test to exclude an influence of relaxation on the OCV curves. A CC of 0.1C was implemented to charge the cells to 4.2 V and then the same CV charge phase as above was employed. After a pause of 1 h, the cells were discharged with a 0.1C CC to 2.7 V and with the same CV discharge phase as above.

The impedance spectrum was measured 6 h after the OCV test in galvanostatic mode from 100 kHz to 10 mHz with an AC amplitude of max. 200 mA at 50% SoC. The real part of the impedance at the zero crossing in the Nyquist plot was taken as the ohmic resistance of the cell. A three-stage EIS test plan is adopted to minimize the test duration by reducing the sample points at lower frequencies. The details about the EIS test plan are listed in Tab. 7.

4.3 Aging Test Methods

Tab. 8 and Tab. 9 provide an overview of the calendar aging and cycle life aging test matrix, respectively. For the calendar aging, 25°C, 40°C and 55°C were chosen to verify the Arrhenius behavior of LIC aging. 50% storage SoC was selected, since it corresponds to the average SoC of full cycling in the cycle life test.

Table 8. Calendar aging test matrix for investigating the stress factor temperature.

	25 °C	40 °C	55 °C
50% SoC	×	×	×

Table 9. Cycle life aging test matrix for investigating the stress factors temperature, charge C-rates and discharge C-rates.

	10 °C	25 °C	40 °C
3C Charge + 1C Discharge		×	
2C Charge + 1C Discharge		×	
C/2 Charge + 1C Discharge		×	
1C Charge + 1C Discharge	×	×	×
1C Charge + 3C Discharge		×	
1C Charge + 5C Discharge		×	

For the cycle life aging, temperatures 10°C, 25°C and 40°C were chosen to investigate both the low temperature aging behavior and the high temperature aging behavior of the cell. In the cycling profile in Fig. 32, cells were charged with a 1C CC-CV procedure and discharged with a 1C CC procedure at each temperature. After discharge and before charge, there is a 5 min pause. The charging process was switched from CC to CV at 4.2 V and the CV process was stopped when the current dropped below 0.05C. The discharging process was stopped at 2.7 V.

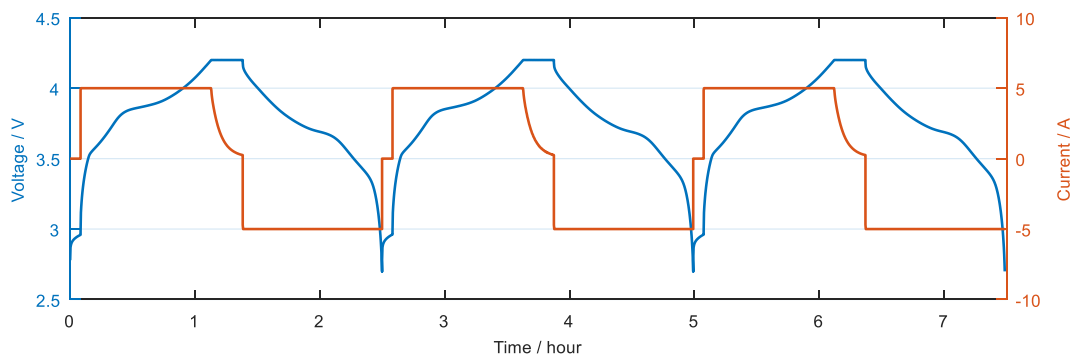


Figure 32. 1C CC-CV charge and 1C CC discharge cycling profile (3 cycles).

For the discharge rate test series, all cells were tested at 25°C. The discharge procedure was changed to 3C and 5C CC discharge respectively, whereas the charge procedure was kept the same. For the charge rate test series, all cells were tested at 25°C. The charge procedure in Fig. 32 was changed to C/2, 2C and 3C CC charge respectively, whereas the CV charge and CC

discharge were kept the same. At least two cells were tested under each aging condition. The same NTC thermistors were adopted during the cycle life test to monitor the cell temperature.

4.4 Half Cell Measurements

A fresh cell was firstly CCCV discharged to 0% SoC and then disassembled in an argon-filled glove box (H_2O and $\text{O}_2 < 0.1$ ppm, MBraun, Germany). The cell had a Z-folding structure with 16 double-side coated anodes and 15 double-side coated cathodes plus 2 single-side coated cathodes on both ends.

Small round slices were punched out of a single-side coated cathode. For the anode, the coating on one side was scratched off with great caution and then small round slices were punched out of its single-side coated part. These slices were then rinsed with dimethyl carbonate to remove residual electrolyte and dried overnight in the glove box. Small round slices were also punched out of a lithium metal foil for the construction of Swagelok T-cells.

As illustrated in Fig. 33, a Swagelok T-cell consists of a working electrode (WE), a counter electrode (CE) and a reference electrode (RE) [191]. Herein, the lithium slice was the RE and the anode and cathode slices were the WE and the CE. Glass fiber separators and LP572 electrolyte from BASF were used in the Swagelok T-cells. The sizes and the voltage ranges of the electrodes were listed in Tab. 10.

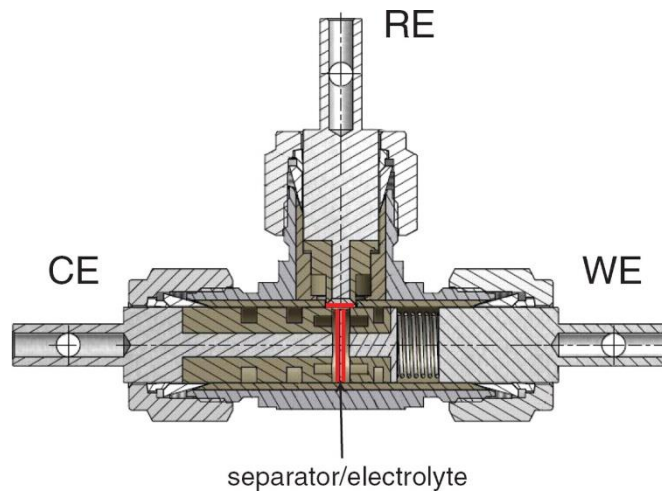


Figure 33. Schematic of the Swagelok T-cell set-up [191].

Table 10. Sizes and test voltage ranges of the electrodes in a Swagelok T-cell.

	Diameter	Voltage Range vs. Li/Li^+
Lithium Slice	11 mm	0 V
Anode Slice	10 mm	0.1-1.5 V
Cathode Slice	10 mm	2.7-4.3 V

Three identical Swagelok T-cells were constructed and tested, but only the best test results were presented. Fig. 34 shows the potential profiles of the anode vs. lithium metal and the cathode vs. lithium metal. The cycling tests were performed with a current of 0.046 mA, approximately C/50 for both electrodes. The potential profiles are stable during the two cycles and the data from the second cycle is utilized for further analysis.

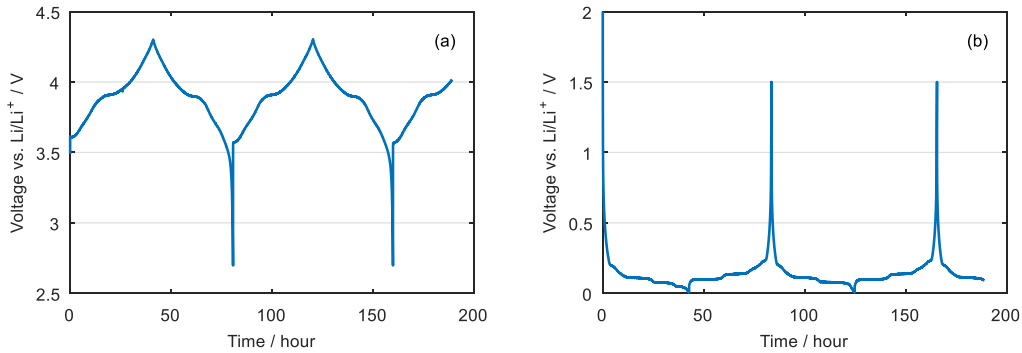


Figure 34. Potential profiles of the (a) cathode and (b) anode vs. lithium metal.

4.5 DC Pulse Resistance Test

The charge/discharge DC pulse resistances are measured with the following method. In the charge direction, a 30 s 1C charge pulse is applied to the cell at SoCs from 0% to 95%. Between the pulses, 1C CC charge is utilized to charge the cell to the next required SoC level. After the 30 s charge pulse at 95% SoC, the cell is 1C CCCV charged to 100% SoC. The first 30 s 1C discharge pulse is applied at 100% SoC. Afterwards, the cell is discharged with 1C CC to lower SoCs from 95% to 5%. At each SoC level, a 30 s 1C discharge pulse is carried out. After each pulse, a 10 min pause is added before charging/discharging to the next SoC. After charging/discharging to the next SoC, a 30 min pause is applied before the next pulse. Fig. 35 shows the complete charge/discharge pulse test for one cell. The DC pulse resistance test is applied to several experimental cells at their begin of test (BoT) and end of test (EoT).

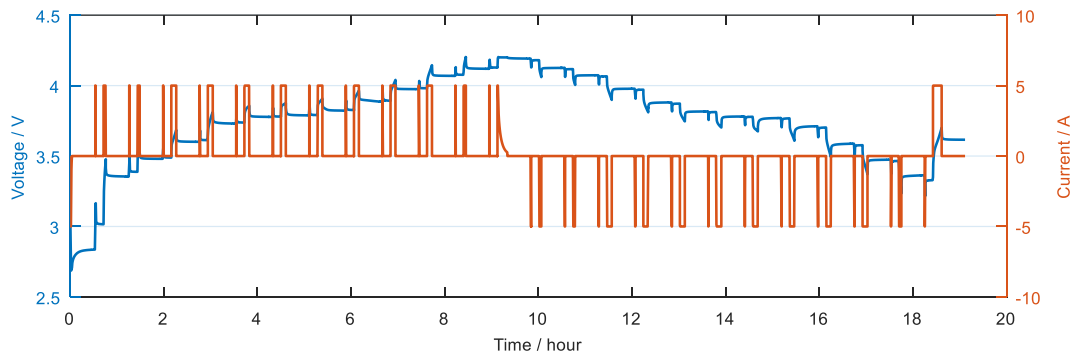


Figure 35. 30s-charge/discharge DC pulse resistance test.

5. Aging Test Results and Discussion

The results of the aging experiment are analyzed and discussed in this chapter. In Section 5.1, the aging behavior of the tested cells is presented, including calendar aging and cycle life aging with different stress factors. In Section 5.2, the current-voltage-based aging detection methods, i.e., ICA and DVA, are applied to the aged cells. The impedance-based aging detection method is adopted to clarify the aging processes in Section 5.3. Finally, the temperature-based aging detection method is utilized in Section 5.4.

5.1 Aging Behavior of the Tested Lithium-Ion Cell

Calendar aging and cycle life aging tests were carried out according to Tab. 8 and Tab. 9. Their aging behavior is elucidated in the following text. Furthermore, empirical aging models from Subsection 3.1.4 are chosen to describe the degradation of the tested cells.

5.1.1 Calendar Aging

The aging behavior of the cells stored at different temperatures is presented in this subsection. Fig. 36 (a) shows the normalized discharge capacity (CC+CV) versus storage time at 25°C, 40°C and 55°C. One of the two cells tested at 25°C storage was accidentally damaged after several months. Considering the mild aging condition and the good cell quality, only one cell is kept for testing since then. The results of two cells are shown for 40°C and 55°C. At the test beginning, the cells had an average discharge capacity of 5.709 Ah, with a deviation of $\pm 0.26\%$. All three cases show a root-function-like capacity fade and the fade rate increases with temperature. The capacity deviation of the cells tested under identical conditions is generally negligible. Only after 450 days of storage at 55°C, the two cells split into two aging curves. One of them continues its root-function-like capacity fade, while the other experiences a roll-over effect in capacity.

Fig. 36 (b) shows the normalized ohmic resistance versus storage time. The data were taken from the EIS measurements. At the beginning, the average ohmic resistance was 2.7 m Ω , with a deviation of $\pm 5\%$. The ohmic resistance increases also in a root-function-like way in all cases. The increase of the ohmic resistance correlates with the increasing temperature. There are two abrupt ohmic resistance increases at 40°C and 55°C, which are marked with a circle and an ellipse. These two areas are due to malfunction in the climate chamber, which heated the cells up to 70°C for 1-2 days. There are also correspondingly rapid capacity fade in these two periods, which are also marked in Fig. 36 (a). However, the capacity fade is not as remarkable as the resistance increase. After 450 days, the resistance evolution of the cells stored at 55°C also

divides into two directions, with one root-function-like increase and the other accelerated increase.

The same root-function-like behavior and the same roll-over point for capacity fade and ohmic resistance increase indicate the identical aging mechanism behind the two degradation phenomena. SEI growth is known as the most crucial aging mechanism for calendar aging [68, 109, 111]. Additionally, a short period of high temperature (e.g., 70°C) has a stronger influence on the ohmic resistance than on the capacity.

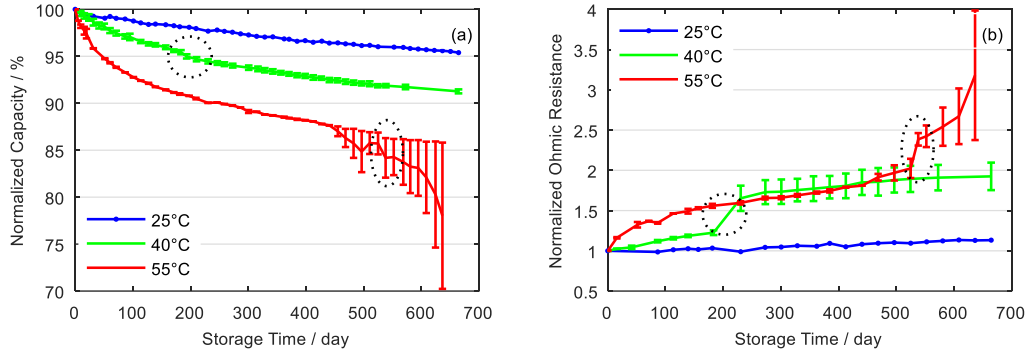


Figure 36. Results from the performance tests at 25°C: (a) normalized capacity plotted as a function of storage time in days; (b) normalized ohmic resistance plotted as a function of storage time in days. Data are shown for the cells stored at 25°C, 40°C and 55°C of 50% SoC. The curve represents the average value of two cells stored at the same temperature and the error bar shows the values of individual cells.

Empirical Aging Model & Arrhenius Behavior

The influences of the climate chamber malfunction are removed before the data are used for the empirical model study. For cells stored at 40°C and 55°C, the one with less aging is chosen for the following analysis, so that the roll-over effect is excluded in the following aging model.

The empirical aging model Eq. 4 from Subsection 3.1.4 is utilized to fit the capacity fade data in Fig. 36 (a). Eqs. 44-46 are obtained as the best fit for all three temperatures as shown in Fig. 37 (a). The mean square error is 4.3×10^{-3} . The storage time t is in d (day).

$$25^{\circ}\text{C}: \quad \frac{Q_{\text{act}}}{Q_{\text{ini}}} = 1 - 0.002355 * \left(\frac{t}{d}\right)^{0.4393} \quad (44)$$

$$40^{\circ}\text{C}: \quad \frac{Q_{\text{act}}}{Q_{\text{ini}}} = 1 - 0.004552 * \left(\frac{t}{d}\right)^{0.4393} \quad (45)$$

$$55^{\circ}\text{C}: \quad \frac{Q_{\text{act}}}{Q_{\text{ini}}} = 1 - 0.008563 * \left(\frac{t}{d}\right)^{0.4393} \quad (46)$$

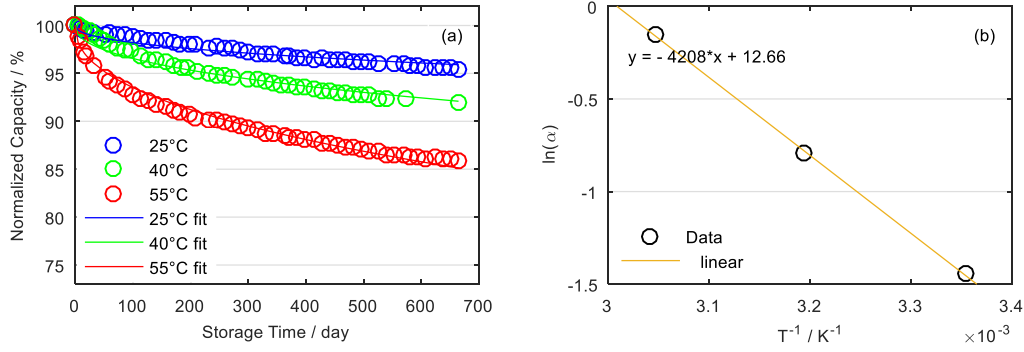


Figure 37. (a) Fitting results of capacity fade due to calendar aging at different temperatures; (b) the influence of the temperature on the capacity fade reaction rate: a plot of $\ln(\alpha)$ vs. T^{-1} .

The factors before the time exponent in Eqs. 44-46 are extracted to verify the Arrhenius behavior of capacity fade. The Arrhenius behavior describes the temperature dependence of the reaction rate α as follows (according to Eq. 4):

$$\alpha = B_{cal} \exp\left(-\frac{E_{a_{cal}}}{RT}\right) \quad (47)$$

After a logarithmic transformation, the following equation is obtained:

$$\ln(\alpha) = \ln(B_{cal}) - \frac{E_{a_{cal}}}{R} \cdot \frac{1}{T} \quad (48)$$

A linear correlation between $\ln(\alpha)$ and T^{-1} should be observed, if the reaction rate of capacity fade agrees with the Arrhenius law. In Fig. 37 (b), $\ln(\alpha)$ is plotted versus the reciprocal temperature. A linear dependency is clearly presented. The linear regression has a norm of residuals of 0.014. The activation energy is calculated to be 35 kJ/mol. Hence, the final empirical model of capacity fade for calendar aging can be expressed as follows:

$$\frac{Q_{act}}{Q_{ini}} = 1 - 3149 * \exp\left(-\frac{34985 \text{ J/mol}}{RT}\right) \left(\frac{t}{d}\right)^{0.4393} \quad (49)$$

Similarly, Eq. 5 from Subsection 3.1.4 is applied to fit the ohmic resistance increase in Fig. 36 (b). The following equations are obtained as the best fit for all three temperatures as shown in Fig. 38 (a). The mean square error is 4.9×10^{-5} . The storage time t is in d.

$$25^{\circ}\text{C}: \quad \frac{R_{act}}{R_{ini}} = 1 + 0.0036 * \left(\frac{t}{d}\right)^{0.5139} \quad (50)$$

$$40^{\circ}\text{C}: \quad \frac{R_{act}}{R_{ini}} = 1 + 0.0170 * \left(\frac{t}{d}\right)^{0.5139} \quad (51)$$

$$55^{\circ}\text{C}: \quad \frac{R_{act}}{R_{ini}} = 1 + 0.0361 * \left(\frac{t}{d}\right)^{0.5139} \quad (52)$$

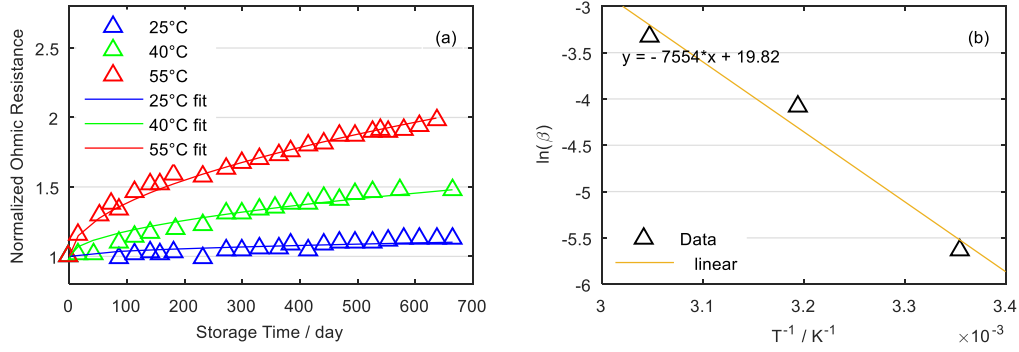


Figure 38. (a) Fitting results of ohmic resistance increase due to calendar aging at different temperatures; (b) the influence of the temperature on the ohmic resistance increase reaction rate: a plot of $\ln(\beta)$ vs. T^{-1} .

The factors before the time exponent in Eqs. 50-52 are extracted to verify the Arrhenius behavior of the ohmic resistance increase. The Arrhenius behavior describes the temperature dependence of the reaction rate β as follows (according to Eq. 5):

$$\beta = B'_{cal} \exp\left(-\frac{Ea'_{cal}}{RT}\right) \quad (53)$$

After a logarithmic transformation, the following equation is obtained:

$$\ln(\beta) = \ln(B'_{cal}) - \frac{Ea'_{cal}}{R} \cdot \frac{1}{T} \quad (54)$$

Therefore, a linear correlation between $\ln(\beta)$ and T^{-1} should be observed, if the reaction rate of ohmic resistance increase agrees with Arrhenius law. In Fig. 38 (b), $\ln(\beta)$ is plotted versus the reciprocal temperature. The linear regression has a norm of residuals of 0.28. The activation energy is calculated to be 63 kJ/mol, which almost doubles that of capacity fade. The final empirical model of ohmic resistance increase for calendar aging can be expressed as follows:

$$\frac{R_{act}}{R_{ini}} = 1 + 4.052 \times 10^8 * \exp\left(-\frac{62804 \text{ J/mol}}{RT}\right) \left(\frac{t}{d}\right)^{0.5139} \quad (55)$$

Round-Trip Energy Efficiency

The round-trip energy efficiency, with the definition in Eq. 56, is determined with *Wh-step* values recorded by BaSyTec during the second cycle of regular capacity tests.

$$\eta_{\text{round-trip}} = \frac{\text{Energy Output by a full Discharge}}{\text{Energy Input by a full Charge}} \quad (56)$$

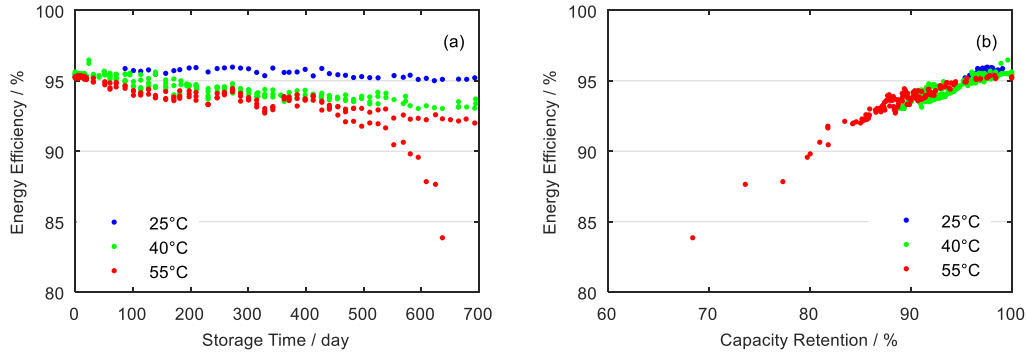


Figure 39. The evolution of the round-trip energy efficiency measured at 25°C and 1C with (a) storage time and (b) capacity retention. All the cells come from the calendar aging tests at 25°C, 40°C and 55°C.

The round-trip energy efficiency considers the coulombic efficiency as well as the energy loss due to overpotentials inside the cell. The evolution of the energy efficiency versus storage time and capacity retention is separately displayed in Fig. 39.

In Fig. 39 (a), the energy efficiency decreases with temperature after the same storage period. This is due to the high ohmic resistance increase caused by high temperature storage, thus more overpotential-induced energy loss. The extremely low energy efficiency of one cell stored at 55°C is also evoked by high overpotential, since the cell shows a roll-over effect in its ohmic resistance in Fig. 36 (b). In Fig. 39 (b), there is a quasi-linear trend between the round-trip energy efficiency and the capacity retention. All three temperatures show almost the same decrease in energy efficiency at the same capacity retention. Commercial cells possess good coulombic efficiency, thus energy efficiency decrease is often a result of ohmic and non-ohmic resistance increase.

5.1.2 Cycle Life Aging

The aging behavior of cells cycled at different temperatures and with different charge/discharge rates is presented in this subsection. Climate chambers are employed to keep the ambient temperature constant during the cycling tests. Nonetheless, the surface temperature of the cells varies and fluctuates due to heat generation inside the cell.

Tab. 11 presents the minimum, maximum and average cell surface temperatures for different cycling conditions. The temperature is measured at the surface center point of each cell as shown in Fig. 31. The temperature data in Tab. 11 are taken from the last cycling tests before EoT. These values can be considered as worst-case values, as the cells have lower internal resistances in their earlier cycles.

Table 11. Cell surface temperature during the last cycling tests.

Charge	Discharge	Ambient Temperature	Minimum Temperature	Average Temperature	Maximum Temperature
1C	1C	10°C	8.4°C	10.1°C	15.4°C
1C	1C	25°C	25.3°C	27.5°C	33.1°C
1C	1C	40°C	39.6°C	41.5°C	44.2°C
1C	3C	25°C	26.4°C	30.2°C	40.2°C
1C	5C	25°C	26.4°C	31.1°C	49.3°C
C/2	1C	25°C	25.0°C	25.8°C	27.7°C
2C	1C	25°C	26.8°C	28.2°C	30.3°C
3C	1C	25°C	27.9°C	29.8°C	33.5°C

5.1.2.1 Effect of the Temperature

The aging behavior of cells tested at different temperatures is presented here. Fig. 40 shows the evolution of normalized discharge capacity and normalized ohmic resistance versus equivalent full cycle (EFC) at the three ambient temperatures. In Subsection 3.1.2, Ah-throughput is introduced as a stress factor for cycle life aging. EFC is equivalent to Ah-throughput, since a constant amount of Ah-throughput is assumed for each cycle during the cycle life tests.

$$EFC = \frac{Q_{Ah}}{2 * Q_{ini}} \quad (57)$$

Here Q_{Ah} is the total Ah-throughput including charge and discharge processes and Q_{ini} is the initial cell capacity.

The three ambient temperatures, i.e., 10°C, 25°C and 40°C, correspond to the average surface temperatures of 10.1°C, 27.5°C and 41.5°C in Tab. 10. All tested cells had an initial average discharge capacity (CC+CV) of 5.709 Ah, with a deviation of $\pm 0.26\%$. In the first 300 cycles, there is a root-function-like capacity fade for all tested cells in Fig. 40 (a). Afterwards, the capacity decreases linearly in all cases yet at different rates. Cycling at 25°C is the mildest operational condition with the lowest capacity degradation rate over EFC. Cycling at 10°C and 40°C both accelerate the capacity fade. The capacity deviation of the cells tested under identical conditions is generally negligible. An exception occurs for cells cycled at 40°C after more than 15% capacity loss. Here, a split of two aging curves is observed. One cell continues to lose its capacity linearly over EFC. The other cell shows a roll-over effect in its capacity fade.

Fig. 40 (b) shows the normalized ohmic resistance versus EFC. The data were taken from the EIS measurements. At the beginning, the average ohmic resistance was $2.7 \text{ m}\Omega$, with a deviation of $\pm 5\%$. The ohmic resistance increases linearly from the beginning in all cases. In contrast to the capacity fade in Fig. 40 (a), 25°C induces a faster ohmic resistance increase than 10°C . The resistance deviation is larger than the capacity deviation and expands gradually over EFC. In the case of the cells cycled at 40°C , the resistance evolution also divides into two degradation modes, with one continuous linear increase and the other accelerated increase. This coincides with their capacity evolution.

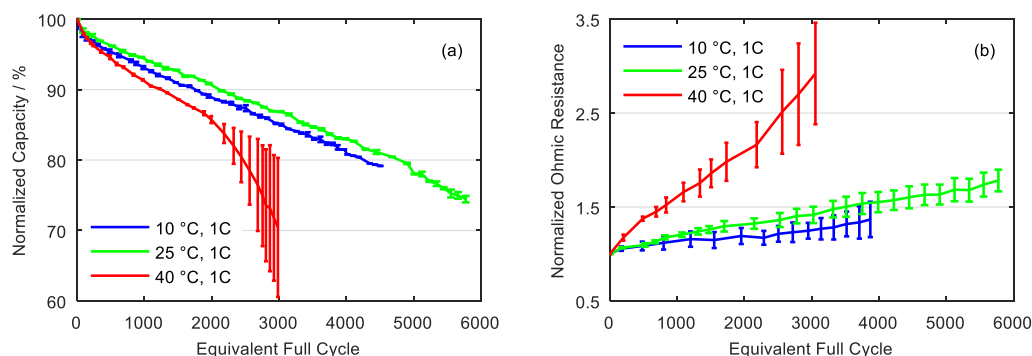


Figure 40. Results from the performance tests at 25°C : (a) normalized capacity plotted as a function of EFC; (b) normalized ohmic resistance plotted as a function of EFC. Data are shown for the cells cycled with 1C charge/discharge at 10°C , 25°C and 40°C . The curve represents the average value of two cells tested under the same condition and the error bar shows the values of individual cells [5].

A linear dependency of cell capacity on EFC has been reported in several studies [98, 192, 193]. The aging mechanisms in this linear part could be categorized into cycle-induced capacity loss and calendar-aging-induced capacity loss. The cycle-induced capacity loss refers to the lithium consumption caused by the cycle-triggered cracks on the anode particles and the additional SEI formation. The calendar-aging-induced capacity loss is related to temperature-accelerated parasitic reactions, which consume cyclable lithium, e.g., formation and reconstruction of SEI [193]. A higher capacity fade rate at 10°C than at 25°C is possibly a result of lithium plating [194, 195], since internal electrode resistances increase with lower temperature and the anode potential may eventually drop to potentials negative to reversible Li/Li^+ potential [196].

The ohmic resistance originates from the bulk chemistry of a cell, including resistance of the electrolyte, active materials and current collectors [62, 146, 152, 156, 157]. The ohmic resistance increase mainly originates from the decomposition of electrolyte, including both conductive salt and solvent, which in turn changes the electrolyte conductivity [39, 197–199]. The cell cycled at 40°C with a higher aging rate and a new cell were disassembled. This revealed that the aged cell had dried out, as no traces of electrolyte wetting the electrodes and the separator were visible. The absence of visible liquid electrolyte leads to the assumption that electrolyte decomposition is the reason for the marked capacity fade and resistance increase. Furthermore, plated lithium was also observed on the aged anode layers, which is usually not

expected at a temperature of 40 °C. This hints a relationship between the roll-over effect of cell capacity fade and lithium plating as has already been investigated in [44, 62]. Details of the dissembled cell are to be found in Chapter 6.

Empirical Aging Model & Arrhenius Behavior

In order to separate the aging influences from calendar aging and cycle life aging, capacity loss due to calendar aging is calculated with Eq. 49 and subtracted from the total capacity loss in Fig. 40 (a). For cells cycled at 40°C, the one with less aging is chosen. For 10°C and 25°C, the average aging data are adopted. For the calculation of calendar aging, the average cell temperatures 10.1°C, 27.5°C and 41.5°C from Tab. 11 are utilized.

The empirical aging model from Subsection 3.1.4 is employed to fit the capacity fade data without the calendar aging. The influences of temperature and Ah-throughput are addressed here. The influences of discharge rate and charge rate are introduced in the next two subsections. Eqs. 58-60 are obtained as the best fit for all three temperatures as shown in Fig. 41 (a). The mean square error is 0.0055.

$$10^{\circ}\text{C}: \quad \frac{Q_{\text{act}}}{Q_{\text{ini}}} = 1 - 2.0 \times 10^{-5} * \left(\frac{Q_{\text{Ah}}}{\text{Ah}}\right)^{0.8441} \quad (58)$$

$$25^{\circ}\text{C}: \quad \frac{Q_{\text{act}}}{Q_{\text{ini}}} = 1 - 1.5 \times 10^{-5} * \left(\frac{Q_{\text{Ah}}}{\text{Ah}}\right)^{0.8441} \quad (59)$$

$$40^{\circ}\text{C}: \quad \frac{Q_{\text{act}}}{Q_{\text{ini}}} = 1 - 1.9 \times 10^{-5} * \left(\frac{Q_{\text{Ah}}}{\text{Ah}}\right)^{0.8441} \quad (60)$$

Eqs. 58-60 show that temperature influences pure cycle life aging, but to a minor extent compared to calendar aging. 25°C is the optimal temperature for 1C cycling. 10°C and 40°C accelerate the cycle life aging to a similar extent. In literature [98, 104, 200, 201], a linear aging and a square root aging over Ah-throughput have both been proposed. The capacity fade of the tested cells in Fig. 41 (a) is closer to the linear aging behavior.

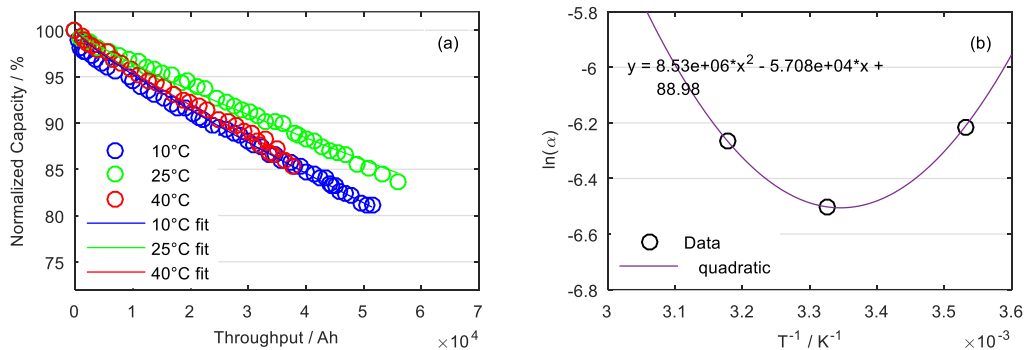


Figure 41. (a) Fitting results of capacity fade due to pure cycle life aging at different temperatures; (b) the influence of the temperature on the capacity fade reaction rate: a plot of $\ln(\alpha)$ vs. T^{-1} .

The factors before the Ah-throughput exponent in Eqs. 58-60 are extracted to analyze the temperature influence on the degradation rate owing to cycle life aging. In Fig. 41 (b), $\ln(\alpha)$ is plotted versus the reciprocal temperature. Unlike in Fig. 37 (b), there is no linear dependency between $\ln(\alpha)$ and T^{-1} . According to literature [195], a quadratic fitting is considered as appropriate for this situation.

The best cycle life can be obtained for moderate temperatures, because low temperatures decrease cycle life due to intensified lithium plating and high temperatures reduce battery life due to Arrhenius-driven aging reactions [202]. Waldmann et al. [195] conducted a comprehensive experiment covering a temperature range from -20°C to 70°C and discovered 25°C as the optimal temperature regarding the cycle life aging behavior of 18650-type cells with a NMC/LMO blended cathode and a graphite anode. As shown by other research works, the optimal cycling temperature can differ from 25°C . It varies with the cell type. Schuster et al. [62] reported the optimum to be at 35°C , whereas Bauer et al. [194] detected it to be around 17°C . Searching for the optimal temperature should consider both the temperature-dependency of calendar aging and the temperature-dependency of pure cycle life aging.

The final empirical model of capacity fade for pure cycle life aging can be expressed as follows:

$$\frac{Q_{\text{act}}}{Q_{\text{ini}}} = 1 - 0.01 * \exp\left(\frac{8530000 \text{ K}^2}{T^2} - \frac{57080 \text{ K}}{T} + 89\right) \left(\frac{Q_{\text{Ah}}}{\text{Ah}}\right)^{0.8441} \quad (61)$$

The total capacity loss during cycling is the addition of calendar aging and pure cycle life aging:

$$\begin{aligned} \frac{Q_{\text{loss}}}{Q_{\text{ini}}} = & 3149 * \exp\left(-\frac{34985 \text{ J/mol}}{RT}\right) \left(\frac{t}{\text{d}}\right)^{0.4393} \\ & + 0.01 * \exp\left(\frac{8530000 \text{ K}^2}{T^2} - \frac{57080 \text{ K}}{T} + 89\right) \left(\frac{Q_{\text{Ah}}}{\text{Ah}}\right)^{0.8441} \end{aligned} \quad (62)$$

Similarly, the ohmic resistance increase due to calendar aging is also subtracted from the data in Fig. 40 (b). For cells cycled at 40°C , the one with less aging is chosen. For 10°C and 25°C , the average aging data are applied. For the calculation of calendar aging, the average cell temperatures 10.1°C , 27.5°C and 41.5°C from Tab. 11 are utilized.

Eqs. 63-65 are obtained as the best fit for all three temperatures as shown in Fig. 42 (a), with a mean square error of 4.7×10^{-5} .

$$10^{\circ}\text{C}: \quad \frac{R_{\text{act}}}{R_{\text{ini}}} = 1 + 1.543 \times 10^{-5} * \left(\frac{Q_{\text{Ah}}}{\text{Ah}}\right)^{0.9271} \quad (63)$$

$$25^{\circ}\text{C}: \quad \frac{R_{\text{act}}}{R_{\text{ini}}} = 1 + 2.102 \times 10^{-5} * \left(\frac{Q_{\text{Ah}}}{\text{Ah}}\right)^{0.9271} \quad (64)$$

$$40^{\circ}\text{C}: \quad \frac{R_{\text{act}}}{R_{\text{ini}}} = 1 + 6.018 \times 10^{-5} * \left(\frac{Q_{\text{Ah}}}{\text{Ah}}\right)^{0.9271} \quad (65)$$

The factors before the Ah-throughput exponent in Eqs. 63-65 are extracted to verify the Arrhenius behavior of ohmic resistance increase. The factors here are much lower than those in Eqs. 50-52 for calendar aging.

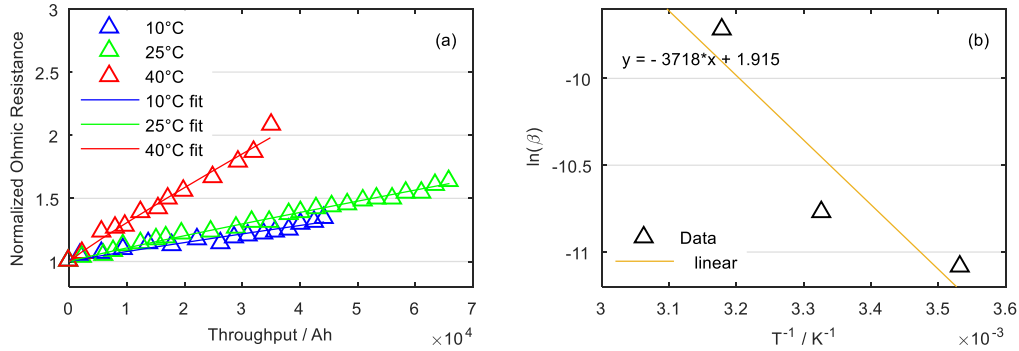


Figure 42. (a) Fitting results of ohmic resistance increase due to pure cycle life aging at different temperatures; (b) the influence of the temperature on the ohmic resistance increase reaction rate: a plot of $\ln(\beta)$ vs. T^{-1} .

In Fig. 42 (b), $\ln(\beta)$ is plotted versus the reciprocal temperature. The linear tendency is less prominent than that of calendar aging in Fig. 38 (b). The linear regression has a norm of residuals of 0.39. The activation energy is calculated to be around 31 kJ/mol, which is the half of the calendar aging activation energy regarding ohmic resistance.

The final empirical model of the ohmic resistance increase for pure cycle life aging can be expressed as follows:

$$\frac{R_{\text{act}}}{R_{\text{ini}}} = 1 + 6.8 * \exp\left(-\frac{30911 \text{ J/mol}}{RT}\right) \left(\frac{Q_{\text{Ah}}}{\text{Ah}}\right)^{0.9271} \quad (66)$$

The total ohmic resistance increase during cycling is the addition of calendar aging and pure cycle life aging:

$$\begin{aligned} \frac{R_{\text{inc}}}{R_{\text{ini}}} = & 4.052 \times 10^8 * \exp\left(-\frac{62804 \text{ J/mol}}{RT}\right) \left(\frac{t}{d}\right)^{0.5139} \\ & + 6.787 * \exp\left(-\frac{30911 \text{ J/mol}}{RT}\right) \left(\frac{Q_{\text{Ah}}}{\text{Ah}}\right)^{0.9271} \end{aligned} \quad (67)$$

Temperature also influences the ohmic resistance increase for pure cycle life aging, but to a minor extent than that for calendar aging. The dependency of ohmic resistance increase on the Ah-throughput is close to linear.

Round-Trip Energy Efficiency

The evolution of the round-trip energy efficiency with Ah-throughput and capacity retention is displayed in Fig. 43. The results of the cells cycled with 1C charge/discharge at 10°C, 25°C and 40°C are presented. The round-trip energy efficiency has a parabolic development over Ah-throughput. In Fig. 43 (a), the cells cycled at 25°C have higher energy efficiencies than those

cycled at 10°C and 40°C at the same Ah-throughput. In Fig. 43 (b), the cells cycled at 25°C and 40°C show better energy efficiencies than those cycled at 10°C at the same capacity retention.

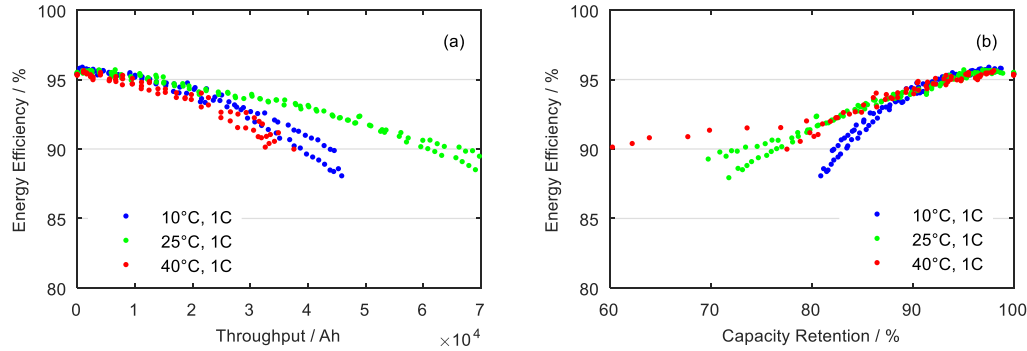


Figure 43. The evolution of the round-trip energy efficiency measured at 25°C and 1C with (a) Ah-throughput and (b) capacity retention. All the cells come from the cycle life aging tests at 10°C, 25°C and 40°C with 1C charge/discharge.

The energy efficiency development versus capacity retention at 25°C and 40°C cycling is almost identical within 20% capacity loss. There is a correlation between energy efficiency and capacity retention similar to calendar aging in Fig. 39 (b). As for cells cycled at 10°C, their energy efficiencies decrease faster than their capacities compared to those of cells cycled at 25°C and 40°C. Considering that 10°C cycling brings the lowest ohmic resistance in Fig. 40 (b), it may induce much higher resistance at medium or low frequencies, causing lower energy efficiencies at 10°C. It is proven with the EIS measurements in Section 5.3 that, cells cycled at 10°C have extremely high charge transfer resistance after more than 10% capacity loss. In the case of 40°C cycling, the cell with 60% rest capacity and 3.5 times higher ohmic resistance has a round-trip energy efficiency of 90%. Meanwhile, in the case of 55°C storage in Fig. 39, the cell with 69% rest capacity and 4 times higher ohmic resistance has an energy efficiency of 84%. The resistance increase has a more direct influence on the decrease of the round-trip energy efficiency.

5.1.2.2 Effect of the Discharge Rate

The effect of discharge rates on the aging behavior of the tested cells is discussed in this subsection. Fig. 44 (a) shows the normalized discharge capacity versus EFC at 25°C ambient temperature with the three discharge rates 1C, 3C and 5C. Their charge rates are kept at 1C. As shown in Tab. 11, average surface temperatures of 27.5°C, 30.2°C and 31.1°C are obtained for 1C, 3C and 5C discharge cycling, respectively. The tested cells had an initial average discharge capacity (CC+CV) of 5.709 Ah, with a deviation of $\pm 0.26\%$.

Similar to Fig. 40 (a), capacity decreases notably in the first 300 cycles and afterwards quasi linearly in all cases. All the capacity fade curves run almost parallel after 300 cycles until 80% normalized capacity. The influences of the elevated average surface temperature and the higher discharge rate on the aging rate cannot be separated from each other. 1C cycling has a cycling

life of about 4800 EFC, while 5C cycling achieves around 3500 EFC. The capacity deviation remains imperceptible, except for the cells cycled at 5C near EoT.

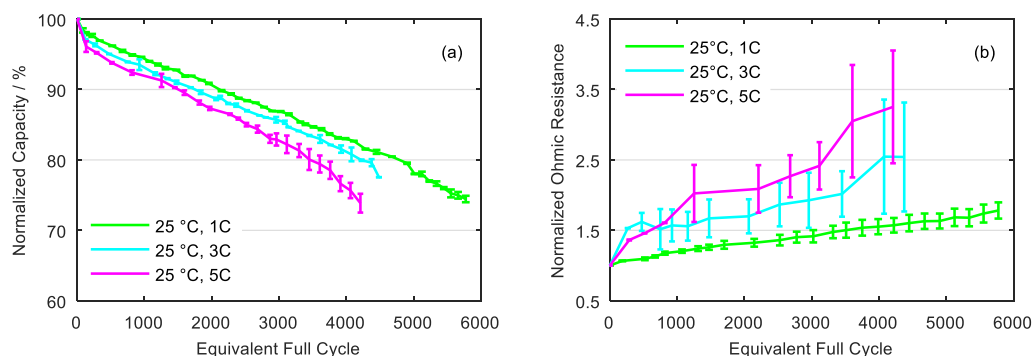


Figure 44. Results from the performance tests at 25°C: (a) normalized capacity plotted as a function of EFC; (b) normalized ohmic resistance plotted as a function of EFC. Data are shown for the cells cycled with 1C charge and 1C/3C/5C discharge at 25°C. The curve represents the average value of two cells tested under the same condition and the error bar shows the values of individual cells [5].

Fig. 44 (b) shows the evolution of ohmic resistance versus EFC at 25°C ambient temperature for the three cycling discharge rates. The cells had an initial average ohmic resistance of 2.7 mΩ, with a deviation of $\pm 5\%$. The ohmic resistances of 3C and 5C, unlike that of 1C, increase rapidly at the beginning, moderately afterwards and again strikingly near EoT. It's noteworthy that the cells cycled with 5C discharge rate double their ohmic resistances very quickly. The resistance deviation of 3C and 5C cycling is much larger than that of 1C cycling and grows with aging. Lithium-ion pouch cells have generally low ohmic resistances compared to 18650-type LICs. The cells cycled at 5C show a maximum ohmic resistance of 11.3 mΩ at EoT, which corresponds to more than three times the initial ohmic resistance.

A similar linear capacity fade rate is observed for the different discharge rates, implying similar aging mechanisms for all three cases. High discharge rates cause rapid volume changes, which break the SEI layer and induce more electrolyte decomposition, thus more capacity is lost in the first 300 cycles at 3C and 5C. Afterwards, the capacity aging rates of 1C, 3C and 5C are approximately identical, which hints a stabilization of the SEI layer and a constant SEI growth rate [203–205]. The higher cell temperatures at 3C and 5C may have also helped the stabilization of the SEI in the first few hundred cycles [5].

Empirical Aging Model & Arrhenius Behavior

In order to separate the aging influence from calendar aging and cycle life aging, the capacity loss due to calendar aging is calculated with Eq. 49 and subtracted from the total capacity loss in Fig. 44 (a). Instead of the ambient temperature 25°C, the average cell temperatures 27.5°C, 30.2°C and 31.1°C from Tab. 11 are used for the calculation of calendar aging. The average capacity fade data from Fig. 44 (a) are applied.

The empirical aging model from Subsection 3.1.4 is utilized to fit the capacity fade due to pure cycle life aging. The exponent of Ah-throughput is kept the same as in Eq. 63, i.e., 0.8441. Eqs. 68-70 are obtained as the best fit for all three discharge rates as shown in Fig. 45 (a). The mean square error is 0.0173.

$$1C: \quad \frac{Q_{act}}{Q_{ini}} = 1 - 1.5 \times 10^{-5} * \left(\frac{Q_{Ah}}{Ah}\right)^{0.8441} \quad (68)$$

$$3C: \quad \frac{Q_{act}}{Q_{ini}} = 1 - 1.8 \times 10^{-5} * \left(\frac{Q_{Ah}}{Ah}\right)^{0.8441} \quad (69)$$

$$5C: \quad \frac{Q_{act}}{Q_{ini}} = 1 - 2.2 \times 10^{-5} * \left(\frac{Q_{Ah}}{Ah}\right)^{0.8441} \quad (70)$$

The factors before the Ah-throughput exponent in Eqs. 68-70 and Eq. 60 (1C cycling at 40°C) are extracted to fit the capacity fade dependence on temperature (above 25°C) and discharge rate due to pure cycle life aging. According to Fig. 41 (b), the capacity fade due to pure cycle life aging has a quadratic dependence on temperature in the range of 10°C to 40°C. It is assumed that the Arrhenius law works for pure cycle life aging in the range between 25°C and 40°C. The reaction rate α is defined as follows (according to Eq. 6):

$$\alpha = B_{cyc} \exp\left(\frac{-Ea_{cyc} + a|I_{dis}|}{RT}\right) \quad (71)$$

Here I_{dis} is a C-rate in h^{-1} . After a logarithmic transformation, the following equation is obtained:

$$\ln(\alpha) = \ln(B_{cyc}) + \frac{(-Ea_{cyc} + a|I_{dis}|)}{R} \cdot \frac{1}{T} \quad (72)$$

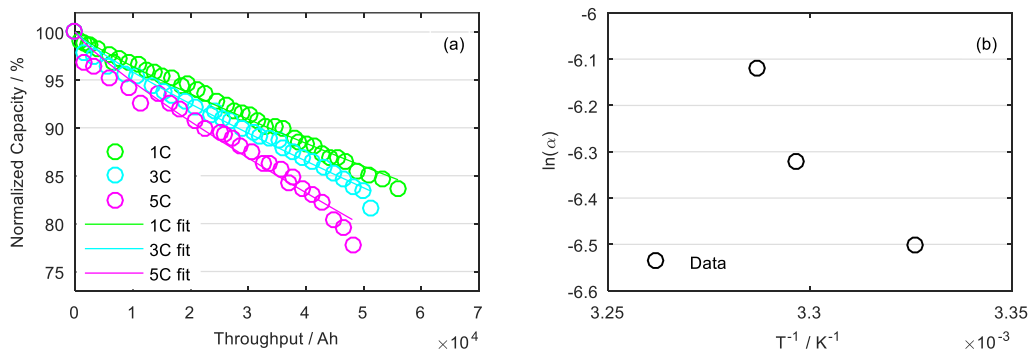


Figure 45. (a) Fitting results of capacity fade due to pure cycle life aging at different discharge rates; (b) the influence of the temperature on the capacity fade reaction rate: a plot of $\ln(\alpha)$ vs. T^{-1} .

The fitting result via the *Curve Fitting Tool* in Matlab is presented in Fig. 46 with a coefficient of determination (R^2) of 0.994 and a mean square error of 4.5×10^{-4} . The reaction rate according to the fitting result is described as follows:

$$\ln(\alpha) = -1.052 + \frac{(-13840 \text{ J/mol} + 201 \text{ J} \cdot \text{h/mol} \cdot |I_{\text{dis}}|)}{R} \cdot \frac{1}{T} \quad (73)$$

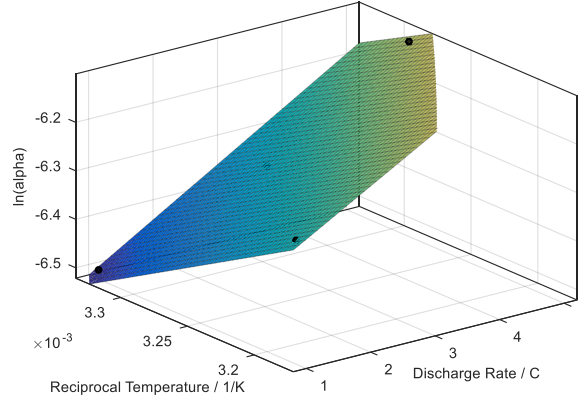


Figure 46. Parameter fitting of the pure cyclic capacity fade reaction rate with the reciprocal temperature and the discharge rate.

Hence, the final empirical model of the capacity fade for pure cycle life aging with dependence on temperature (above 25°C) and discharge rate (I_{dis}) can be expressed as follows:

$$\frac{Q_{\text{act}}}{Q_{\text{ini}}} = 1 - 0.0035 * \exp\left(\frac{-13840 \text{ J/mol} + 201 \text{ J} \cdot \text{h/mol} \cdot |I_{\text{dis}}|}{RT}\right) \left(\frac{Q_{\text{Ah}}}{\text{Ah}}\right)^{0.8441} \quad (74)$$

The total capacity loss during cycling above 25°C can be described as the addition of calendar aging and pure cycle life aging:

$$\begin{aligned} \frac{Q_{\text{loss}}}{Q_{\text{ini}}} = & 3149 * \exp\left(-\frac{34985 \text{ J/mol}}{RT}\right) \left(\frac{t}{d}\right)^{0.4393} \\ & + 0.0035 * \exp\left(\frac{-13840 \text{ J/mol} + 201 \text{ J} \cdot \text{h/mol} \cdot |I_{\text{dis}}|}{RT}\right) \left(\frac{Q_{\text{Ah}}}{\text{Ah}}\right)^{0.8441} \end{aligned} \quad (75)$$

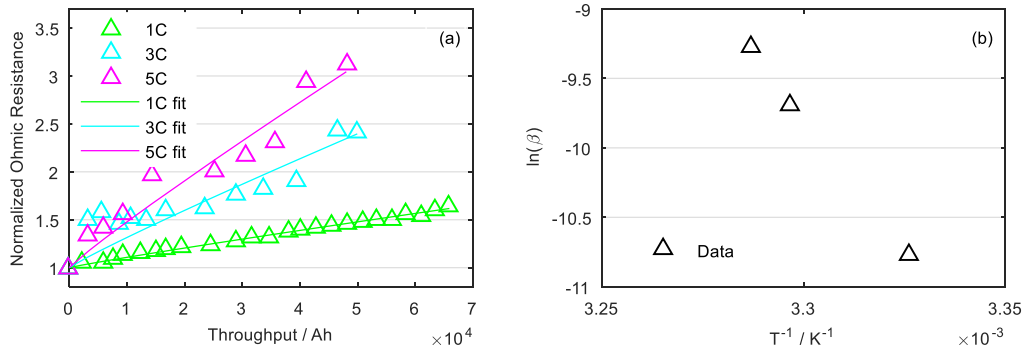


Figure 47. (a) Fitting results of ohmic resistance increase due to pure cycle life aging at different discharge rates; (b) the influence of the temperature on the ohmic resistance increase reaction rate: a plot of $\ln(\beta)$ vs. T^{-1} .

Similarly, the ohmic resistance increase due to calendar aging is also subtracted from the data in Fig. 44 (b). The empirical aging model Eq. 7 from Subsection 3.1.4 is utilized to fit the ohmic

resistance data without the calendar part. The exponent of Ah-throughput is kept the same as in Eq. 66, i.e., 0.9271. Eqs. 76-78 are obtained as the best fit for all three discharge rates as shown in Fig. 47 (a). The mean square error is 0.0015. The variable Q_{Ah} is the total charge throughput in Ah.

$$1C: \quad \frac{R_{act}}{R_{ini}} = 1 + 2.103 \times 10^{-5} * \left(\frac{Q_{Ah}}{Ah}\right)^{0.9271} \quad (76)$$

$$3C: \quad \frac{R_{act}}{R_{ini}} = 1 + 6.148 \times 10^{-5} * \left(\frac{Q_{Ah}}{Ah}\right)^{0.9271} \quad (77)$$

$$5C: \quad \frac{R_{act}}{R_{ini}} = 1 + 9.334 \times 10^{-5} * \left(\frac{Q_{Ah}}{Ah}\right)^{0.9271} \quad (78)$$

The factors before the Ah-throughput exponent in Eqs. 76-78, Eq. 63 and Eq. 65 (1C cycling at 10°C and 40°C) are extracted to analyze the ohmic resistance increase dependence on temperature (between 10°C and 40°C) and discharge rate due to pure cycle life aging. The reaction rate β is defined as follows:

$$\beta = B'_{cyc} \exp\left(\frac{-Ea'_{cyc} + a'|I_{dis}|}{RT}\right) \quad (79)$$

Here I_{dis} is a C-rate. After a logarithmic transformation, the following equation is obtained:

$$\ln(\beta) = \ln(B'_{cyc}) + \frac{-Ea'_{cyc} + a'|I_{dis}|}{R} \cdot \frac{1}{T} \quad (80)$$

The fitting result via the *Curve Fitting Tool* in Matlab is presented in Fig. 48 with a coefficient of determination (R^2) of 0.931 and a mean square error of 0.082. The final empirical model of the ohmic resistance increase for pure cycle life aging with dependence on temperature (between 10°C and 40°C) and discharge rate (I_{dis}) can be expressed as follows:

$$\frac{R_{act}}{R_{ini}} = 1 + 7.6 * \exp\left(\frac{-31830 \text{ J/mol} + 669 \text{ J} \cdot \text{h/mol} * |I_{dis}|}{RT}\right) \left(\frac{Q_{Ah}}{Ah}\right)^{0.9271} \quad (81)$$

The total ohmic resistance increase during cycling between 10°C and 40°C is the addition of calendar aging and pure cycle life aging:

$$\begin{aligned} \frac{R_{inc}}{R_{ini}} &= 4.052 \times 10^8 * \exp\left(-\frac{62804 \text{ J/mol}}{RT}\right) \left(\frac{t}{d}\right)^{0.5139} \\ &+ 7.6 * \exp\left(\frac{-31830 \text{ J/mol} + 669 \text{ J} \cdot \text{h/mol} * |I_{dis}|}{RT}\right) \left(\frac{Q_{Ah}}{Ah}\right)^{0.9271} \quad (82) \end{aligned}$$

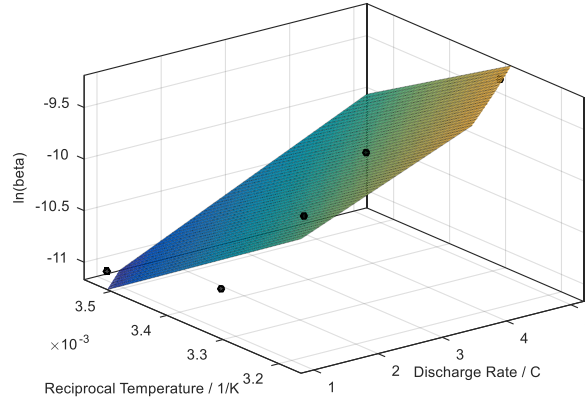


Figure 48. Parameter fitting of the pure cyclic ohmic resistance increase reaction rate with the reciprocal temperature and the discharge rate.

Round-Trip Energy Efficiency

The evolution of the round-trip energy efficiency with Ah-throughput and capacity retention is shown in Fig. 49. The results of the cells cycled with 1C charge and 1C, 3C or 5C discharge at 25°C are displayed.

The cells cycled with 1C have higher and more stable energy efficiencies than those cycled with 3C and 5C. The difference in their energy efficiencies originates most probably from their internal overpotentials. 3C and 5C discharge cycling generate higher resistances than 1C discharge cycling. For example, in Fig. 44 (b), the cells cycled with 3C and 5C discharge show much higher and more scattered ohmic resistances.

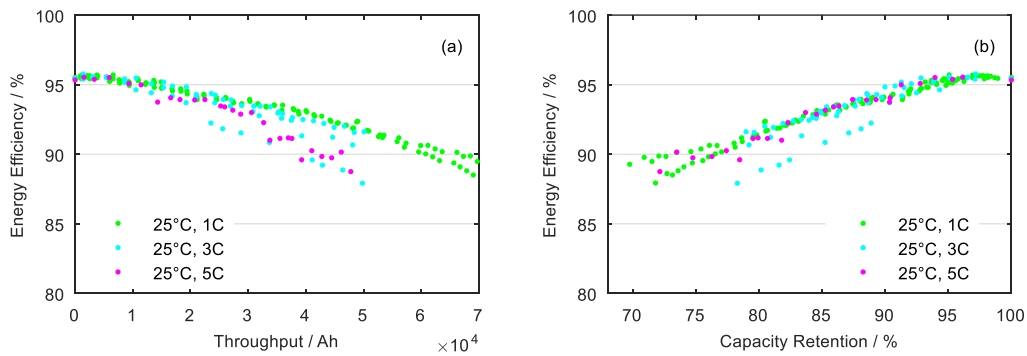


Figure 49. The evolution of the round-trip energy efficiency measured at 25°C and 1C with (a) Ah-throughput and (b) capacity retention. All the cells come from the cycle life aging tests at 25°C with 1C charge and 1C/3C/5C discharge.

5.1.2.3 Effect of the Charge Rate

The aging behavior of cells cycled with C/2, 1C, 2C or 3C charge and 1C discharge at 25°C is presented in this subsection. The investigation of charge rate was started later, so that the cells in this subsection have experienced much fewer cycles than the above ones. However, a clear aging tendency can still be observed.

Fig. 50 (a) shows the normalized discharge capacity versus EFC at 25°C with charge rates C/2, 1C, 2C and 3C. The discharge rate is kept at 1C. As shown in Tab. 11, average surface temperatures of 25.8°C, 27.5°C, 28.2°C and 29.8°C are recorded for C/2, 1C, 2C and 3C, respectively. The influence of charge rate on the cell heating is less prominent than that of discharge rate, since the reaction heat is positive (heat extraction from the environment) for the most time during the charge process. The tested cell in this subsection had an initial average discharge capacity (CC+CV) of 5.657 Ah, with a deviation of $\pm 0.45\%$.

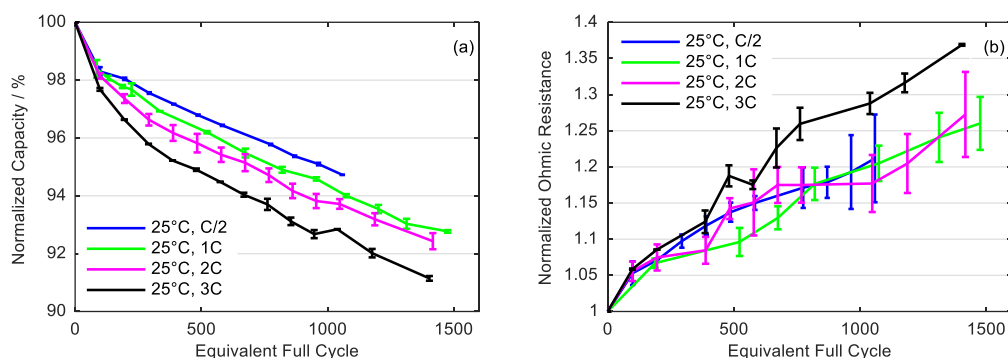


Figure 50. Results from the performance tests at 25°C: (a) normalized capacity plotted as a function of EFC; (b) normalized ohmic resistance plotted as a function of EFC. Data are shown for the cells cycled with 0.5C/1C/2C/3C charge and 1C discharge at 25°C. The curve represents the average value of two cells tested under the same condition and the error bar shows the values of individual cells.

The influence of charge rate on the capacity fade is similar to that of discharge rate in Fig. 44 (a). The capacity fade in the first 300 cycles is faster at a higher charge rate. Afterwards, however, the capacity fade curves of all charge rates are almost parallel. The capacity deviation is negligible. At 1404 EFCs, the average capacity loss at 3C charge and 1C discharge is 8.85%, while the average capacity loss at 1C charge and 3C discharge in Fig. 44 (a) is 8.69%. High charge rate causes slightly more capacity loss than high discharge rate.

Fig. 50 (b) shows the evolution of ohmic resistance versus EFC at 25°C for the four charge rates. The tested cell in this subsection had an initial average ohmic resistance of 2.9 mΩ, with a deviation of $\pm 6\%$. Compared to Fig. 44 (b), the discharge rate has a more pronounced influence on the ohmic resistance than the charge rate. Meanwhile, the ohmic resistance deviation has increased little at higher charge rates. C/2 has even a slightly higher ohmic resistance increase than 1C.

The rapid capacity fade in the first 300 cycles can be explained by the SEI break and repair mechanism. The linear aging area afterwards indicates a stabilization of the SEI layer. Although high charge rate increases the risk of lithium plating, the CV phase provides a chance for some plated lithium to reintercalate into the graphite and thus lithium plating is not yet noticeable in cases of 2C and 3C charge.

Empirical Aging Model & Arrhenius Behavior

In order to separate the aging influence from calendar aging and cycle life aging, the capacity loss due to calendar aging is calculated with Eq. 49 and subtracted from the total capacity loss. Instead of the ambient temperature 25°C, the average cell temperatures 25.8°C, 27.5°C, 28.2°C and 29.8°C from Tab. 11 are used for the calculation of calendar aging, in order to separate the influence from temperature and charge rate. The average capacity fade data from Fig. 50 (a) is applied.

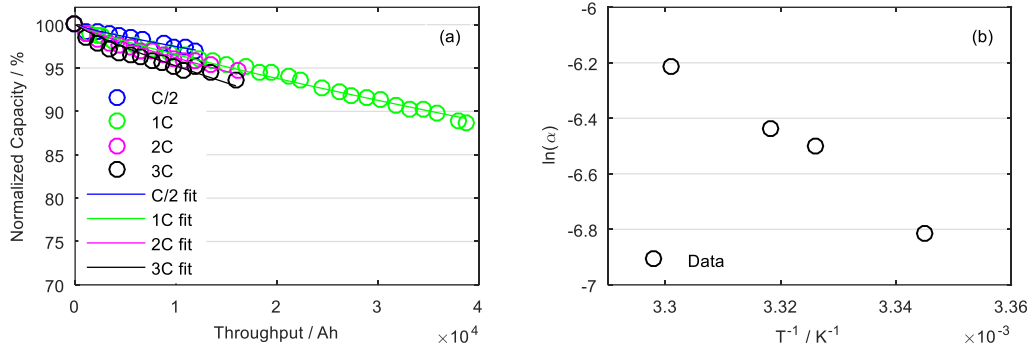


Figure 51. (a) Fitting results of capacity fade due to pure cycle life aging at different charge rates; (b) the influence of the temperature on the capacity fade reaction rate: a plot of $\ln(\alpha)$ vs. T^{-1} .

The empirical aging model from Subsection 3.1.4 is utilized to fit the capacity fade data without the calendar part. The exponent of Ah-throughput is kept at 0.8441. The following equations are obtained as the best fit for all charge rates as shown in Fig. 51 (a). The mean square error is 0.0094.

$$\frac{C}{2}: \quad \frac{Q_{\text{act}}}{Q_{\text{ini}}} = 1 - 1.1 \times 10^{-5} * \left(\frac{Q_{\text{Ah}}}{\text{Ah}}\right)^{0.8441} \quad (83)$$

$$1C: \quad \frac{Q_{\text{act}}}{Q_{\text{ini}}} = 1 - 1.5 \times 10^{-5} * \left(\frac{Q_{\text{Ah}}}{\text{Ah}}\right)^{0.8441} \quad (84)$$

$$2C: \quad \frac{Q_{\text{act}}}{Q_{\text{ini}}} = 1 - 1.6 \times 10^{-5} * \left(\frac{Q_{\text{Ah}}}{\text{Ah}}\right)^{0.8441} \quad (85)$$

$$3C: \quad \frac{Q_{\text{act}}}{Q_{\text{ini}}} = 1 - 2.0 \times 10^{-5} * \left(\frac{Q_{\text{Ah}}}{\text{Ah}}\right)^{0.8441} \quad (86)$$

The factors before the Ah-throughput exponent in Eqs. 83-86 and Eq. 60 (1C cycling at 40°C) are extracted to fit the capacity fade dependence on temperature (above 25°C) and charge rate due to pure cycle life aging. The reaction rate α is defined in Eq. 71 and its logarithmic form in Eq. 72.

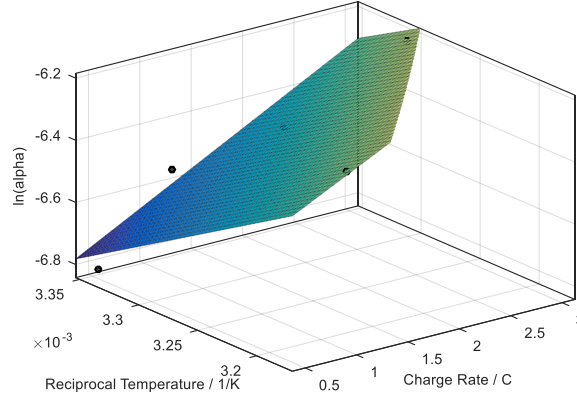


Figure 52. Parameter fitting of the pure cyclic capacity fade reaction rate with the reciprocal temperature and the charge rate.

$\ln(\alpha)$ versus T^{-1} of Eqs. 83-86 is plotted in Fig. 51 (b). $\ln(\alpha)$ versus the charge rate and the reciprocal temperature of Eqs. 83-86 and Eq. 60 is plotted in Fig. 52 with the fitting result of *Curve Fitting Tool* in Matlab. The following equation presents the fitting result with a coefficient of determination (R^2) of 0.924 and a mean square error of 8.5×10^{-3} :

$$\ln(\alpha) = 1.252 + \frac{(-20080 \text{ J/mol} + 432 \text{ J} \cdot \text{h/mol} * |I_{\text{ch}}|)}{R} \cdot \frac{1}{T} \quad (87)$$

Hence, the final empirical model of the capacity fade for pure cycle life aging with dependence on temperature (above 25°C) and charge rate (I_{ch}) can be expressed as follows:

$$\frac{Q_{\text{act}}}{Q_{\text{ini}}} = 1 - 0.035 * \exp\left(\frac{-20080 \text{ J/mol} + 432 \text{ J} \cdot \text{h/mol} * |I_{\text{ch}}|}{RT}\right) \left(\frac{Q_{\text{Ah}}}{\text{Ah}}\right)^{0.8441} \quad (88)$$

The total capacity fade during cycling above 25°C can be described as follows:

$$\begin{aligned} \frac{Q_{\text{loss}}}{Q_{\text{ini}}} &= 3149 * \exp\left(-\frac{34985 \text{ J/mol}}{RT}\right) \left(\frac{t}{d}\right)^{0.4393} \\ &+ 0.035 * \exp\left(\frac{-20080 \text{ J/mol} + 432 \text{ J} \cdot \text{h/mol} * |I_{\text{ch}}|}{RT}\right) \left(\frac{Q_{\text{Ah}}}{\text{Ah}}\right)^{0.8441} \quad (89) \end{aligned}$$

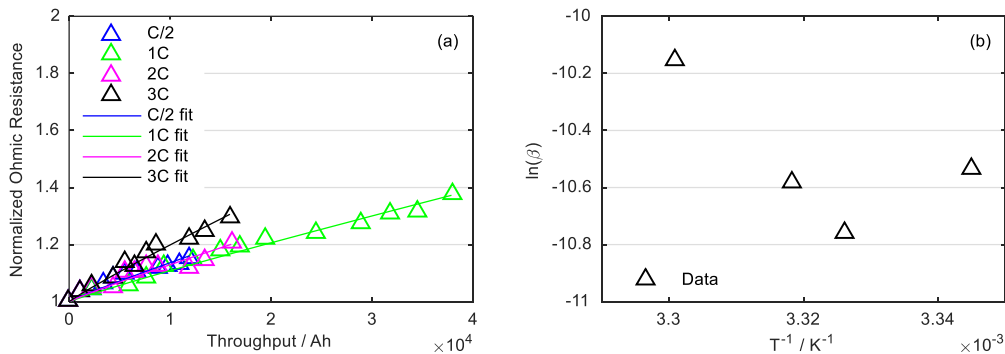


Figure 53. (a) Fitting results of ohmic resistance increase due to pure cycle life aging at different charge rates; (b) the influence of the temperature on the ohmic resistance increase reaction rate: a plot of $\ln(\beta)$ vs. T^{-1} .

The ohmic resistance increase due to calendar aging is also subtracted from the data in Fig. 50 (b). The exponent of Ah-throughput is kept at 0.9271. The following equations are obtained as the best fit for all charge rates as shown in Fig. 53 (a). The mean square error is 2.6×10^{-5} .

$$\frac{C}{2}: \quad \frac{R_{act}}{R_{ini}} = 1 + 2.668 \times 10^{-5} * \left(\frac{Q_{Ah}}{Ah}\right)^{0.9271} \quad (90)$$

$$1C: \quad \frac{R_{act}}{R_{ini}} = 1 + 2.122 \times 10^{-5} * \left(\frac{Q_{Ah}}{Ah}\right)^{0.9271} \quad (91)$$

$$2C: \quad \frac{R_{act}}{R_{ini}} = 1 + 2.534 \times 10^{-5} * \left(\frac{Q_{Ah}}{Ah}\right)^{0.9271} \quad (92)$$

$$3C: \quad \frac{R_{act}}{R_{ini}} = 1 + 3.891 \times 10^{-5} * \left(\frac{Q_{Ah}}{Ah}\right)^{0.9271} \quad (93)$$

The factors before the charge throughput exponent in Eqs. 90-93, Eq. 63 and Eq. 65 (1C cycling at 10°C and 40°C) are extracted to fit the ohmic resistance increase dependence on temperature (between 10°C and 40°C) and charge rate due to pure cycle life aging. The reaction rate β is defined in Eq. 79 and its logarithmic form in Eq. 80.

The fitting result via *Curve Fitting Tool* in Matlab is presented in Fig. 54 with a coefficient of determination (R^2) of 0.824 and a mean square error of 0.067. The final empirical model of the ohmic resistance increase for pure cycle life aging with dependence on temperature (between 10°C and 40°C) and charge rate (I_{ch}) can be expressed as follows:

$$\frac{R_{act}}{R_{ini}} = 1 + 6.6 * \exp\left(\frac{-31010 \text{ J/mol} + 140 \text{ J} \cdot \text{h/mol} * |I_{ch}|}{RT}\right) \left(\frac{Q_{Ah}}{Ah}\right)^{0.9271} \quad (94)$$

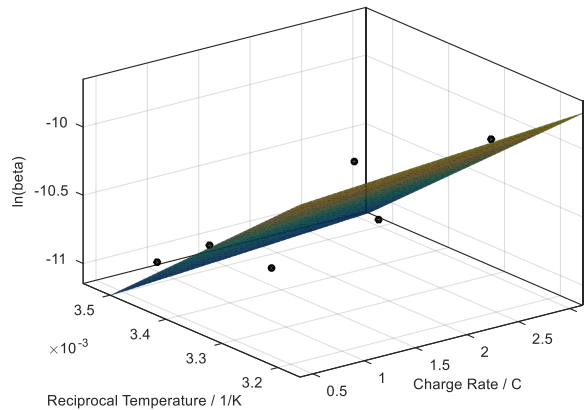


Figure 54. Parameter fitting of the pure cyclic ohmic resistance increase reaction rate with the reciprocal temperature and the charge rate.

The total ohmic resistance increase during cycling between 10°C and 40°C is expressed as follows:

$$\begin{aligned} \frac{R_{\text{inc}}}{R_{\text{ini}}} = & 4.052 \times 10^8 * \exp\left(-\frac{62804 \text{ J/mol}}{RT}\right) \left(\frac{t}{d}\right)^{0.5139} \\ & + 6.6 * \exp\left(\frac{-31010 \text{ J/mol} + 140 \text{ J} \cdot \text{h/mol} * |I_{\text{ch}}|}{RT}\right) \left(\frac{Q_{\text{Ah}}}{\text{Ah}}\right)^{0.9271} \end{aligned} \quad (95)$$

Round-Trip Energy Efficiency

The evolution of the round-trip energy efficiency with Ah-throughput and capacity retention is displayed in Fig. 55. The results of the cells cycled with 1C discharge and C/2, 1C, 2C or 3C charge at 25°C are presented.

In Fig. 55 (a), the cells cycled with 1C charge have higher energy efficiencies than the others, especially after 10000 Ah-throughput. It agrees with the ohmic resistance increase in Fig. 53. The higher ohmic resistances of the cells cycled with C/2, 2C and 3C charge lead to lower energy efficiencies. However, compared to Fig. 49, charge rate increase has less influence on the cell energy efficiency than discharge rate increase.

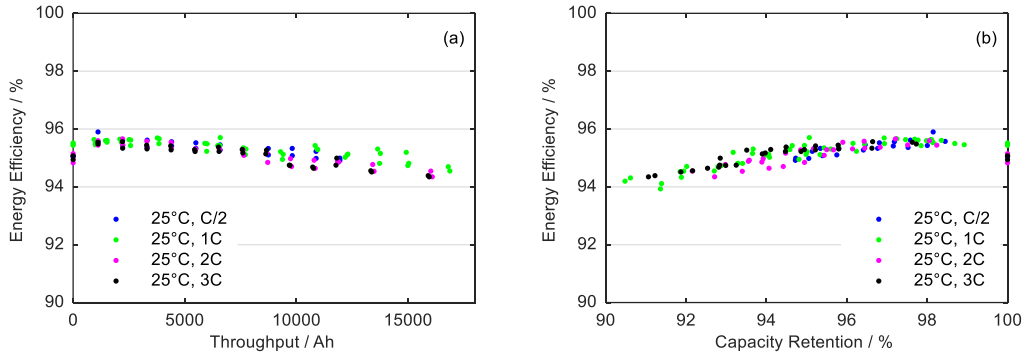


Figure 55. The evolution of the round-trip energy efficiency measured at 25°C and 1C with (a) Ah-throughput and (b) capacity retention. All the cells come from the cycle life aging tests at 25°C with 1C discharge and 0.5C/1C/2C/3C charge.

5.2 Current-Voltage-Based Aging Detection

In this section, current-voltage-based aging detection involves only DVA and ICA methods. The former is useful for the determination of cyclable lithium amount and active material amount on each electrode. The latter is more suitable for the detection of electrode health state and internal resistance increase. The aging data of the cells from Tab. 8 and Tab. 9 are analyzed, except for those cells cycled with C/2, 2C or 3C charge due to their minor capacity loss.

5.2.1 C/10 Charge Voltage Degradation

The fundamental of the current-voltage-based detection methods is the deforming shape of OCV due to aging. As depicted in Subsection 3.2.2.1, the C/10 charge curve from the extended performance test is accurate enough to replace OCV for DVA and ICA transformation. Before applying DVA and ICA detection methods, the deformation of the C/10 charge curves of the

tested cells is presented in Fig. 56. If more than one cell is tested under the same condition, the one with less capacity loss is shown.

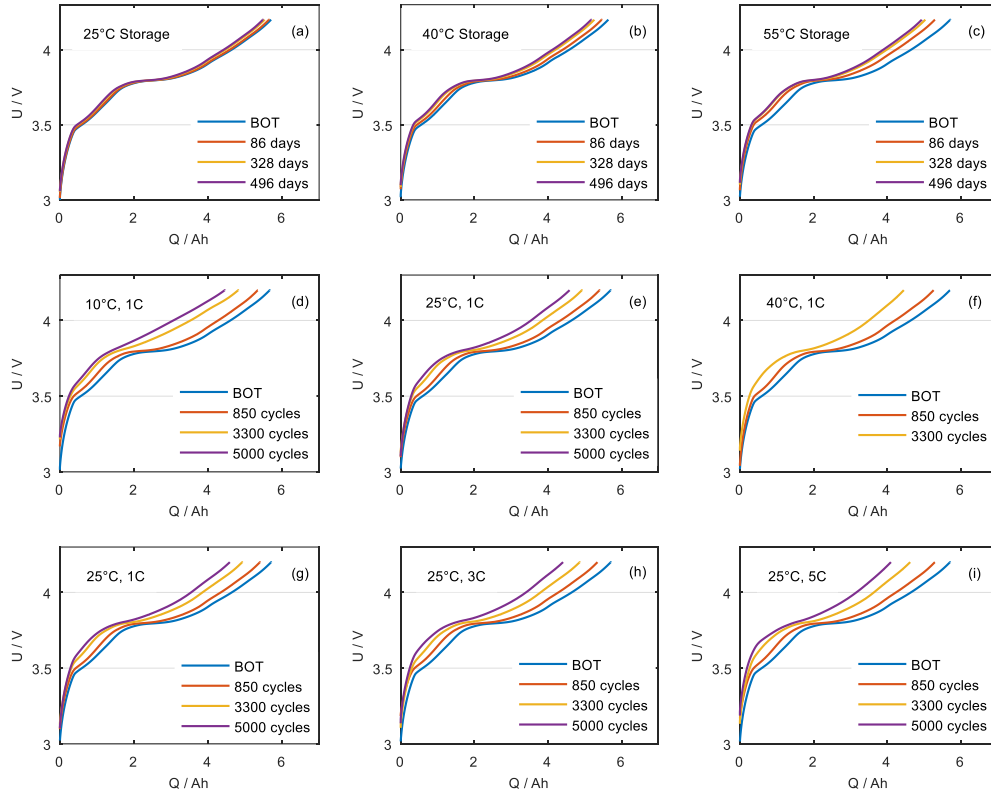


Figure 56. C/10 charge curve evolution of a cell stored at (a) 25°C; (b) 40°C; (c) 55°C; or cycled at (d) 10°C, 1C; (e) 25°C, 1C; (f) 40°C, 1C; (g) 25°C, 1C; (h) 25°C, 3C; (i) 25°C, 5C.

The most obvious trends are the shrinkage of the charge curve (capacity fade) and the blur of the voltage plateaus with aging. The deformation is less prominent for cells in storage than those in cycling. It is difficult to get any more information from the C/10 charge curves without the help of DVA and ICA.

5.2.2 DVA Method

Fig. 57 shows the DVA transformation of C/10 charge curves from Fig. 56. Figs. 57 (a), 57 (b) and 57 (c) show the charge DVA curves of cells stored at 25°C, 40°C and 55°C. The three subplots show mainly the same evolution: the shift of all the curves towards the A1 end, as explained in Fig. 10. This trend slows down after 328 days storage, which corresponds to the root-function-like capacity loss in Fig. 36 (a). High temperature expedites the shift process. The A3 peak, attributed to graphite, becomes less visible after 328 days storage at 55°C, which indicates anode degradation.

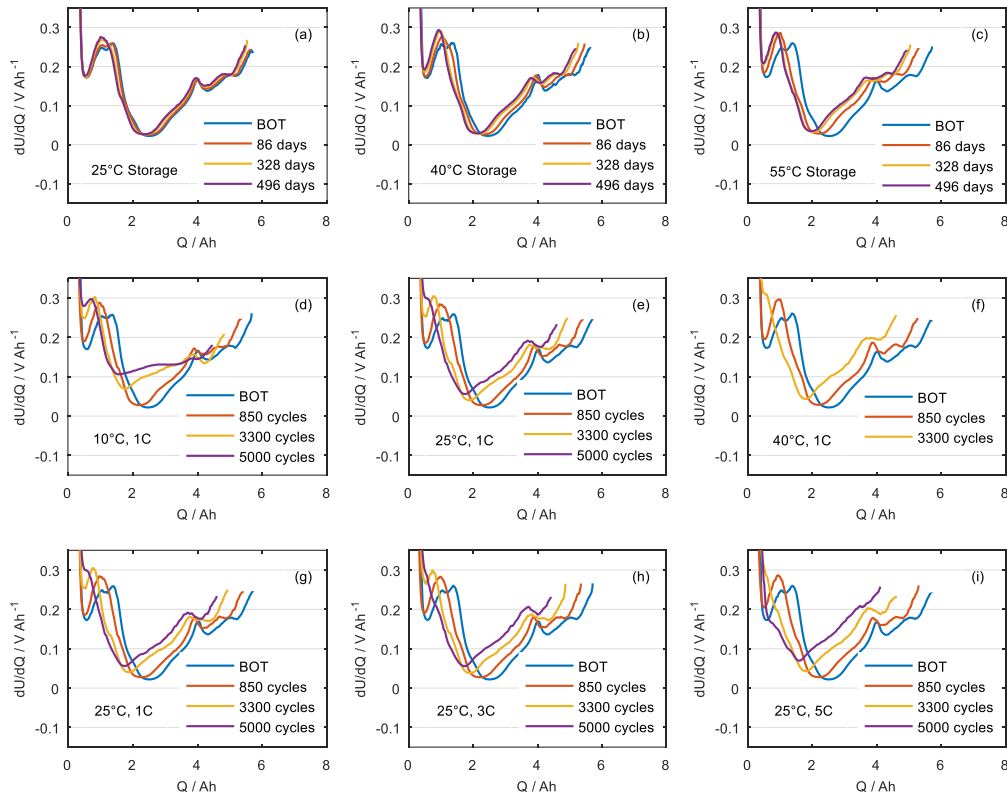


Figure 57. C/10 Charge DVA curve evolution of a cell stored at (a) 25°C; (b) 40°C; (c) 55°C; or cycled at (d) 10°C, 1C; (e) 25°C, 1C; (f) 40°C, 1C; (g) 25°C, 1C; (h) 25°C, 3C; (i) 25°C, 5C.

Figs. 57 (d), 57 (e) and 57 (f) show those cells cycled with 1C charge/discharge at 10°C, 25°C and 40°C. Figs. 57 (g), 57 (h) and 57 (i) show those cells cycled at 25°C with 1C charge and 1C, 3C or 5C discharge. Figs. 57 (e) and 57 (g) are identical. It is displayed twice to keep the appropriate comparison sequence. Except for Fig. 57 (d), all other cases show a continuous parallel shift of the cathode contributions to the A1 end. The shift even leads to the disappearance of A2 and C1 peaks after 5000 cycles. In Fig. 57 (d), the slope between 40% and 100% SoC, which is characteristic of the cathode according to Fig. 10, flattens with cycles, suggesting cathode material degradation. This degradation is further clarified in Subsection 5.2.3 with ICA.

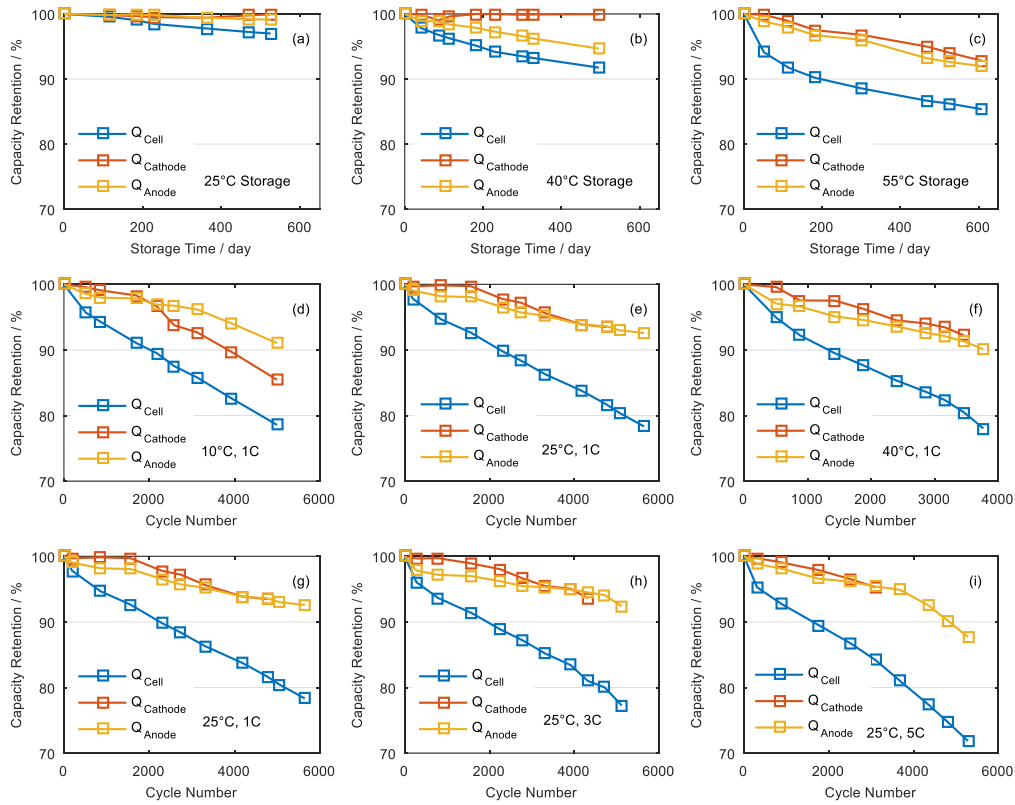


Figure 58. Capacity decrease and loss of electrode active material of a cell stored at (a) 25°C; (b) 40°C; (c) 55°C; or cycled at (d) 10°C, 1C; (e) 25°C, 1C; (f) 40°C, 1C; (g) 25°C, 1C; (h) 25°C, 3C; (i) 25°C, 5C.

LLI and LAM in the tested cells can be quantitatively analyzed with the help of DVA. As described in Fig. 10 (c), A1, A2, A3, C1, C2 and C3 are attributes of the anode and the cathode, respectively. Q_{Anode} , defined as the x-axis distance between A1 and A3, reveals changes in the anode active material capacity. Q_{Cathode} , defined as the x-axis distance between C1 and C3, reveals changes in the cathode active material capacity. Q_{Cell} , defined as the x-axis distance between A1 and C3, is the full cell capacity or cyclable lithium amount.

The DVA curves from Fig. 57 are firstly smoothed to remove noise using *Moving Average Filtering*. Then, the positions of A3 and C1 are detected by the *Findpeaks* function in Matlab. Finally, Q_{Anode} , Q_{Cathode} and Q_{Cell} are plotted versus storage time or cycle number in Fig. 58. It is not intended to measure the precise and absolute capacity amount of electrodes, but to identify the tendency of active material change.

For calendar aging, Q_{Cell} and Q_{Anode} have both root-function-like development in Figs. 58 (a)-(c). The anode loss is within 8% and should have no influence on the full cell capacity owing to 20% anode oversizing in Fig. 10 (c). The cathode loss appears only at 55°C and is within 6%. The majority of the full cell capacity loss comes from LLI.

For cycle life aging, Q_{Cell} has quasi-linear development in Figs. 58 (d)-(i). In Fig. 58 (d), there is extremely high cathode capacity loss, which is due to the aforementioned cathode material degradation at 10°C cycling. 40°C cycling causes higher anode loss and cathode loss than 25°C cycling. However, the anode loss is within 10%, which should not be a reason for cell capacity fade. After 20% cell capacity loss, Q_{Cathode} cannot be detected anymore in Figs. 58 (e) and 58 (f) due to the disappearance of cathode peak C1. At higher discharge rates in Figs. 58 (h) and 58 (i), both anode and cathode loss increase. At 5C discharge cycling in Fig. 58 (i), the anode loss begins to accelerate after 20% cell capacity loss. Generally, the most pronounced aging mechanism for capacity fade is still LLI, which is possibly combined with anode loss around 20% cell capacity loss.

During the calendar aging test as well as the cycle life test, cells with the identical test condition show splitted aging behavior after a certain point of time. DVA method is applied to unveil the reason for the splitted aging.

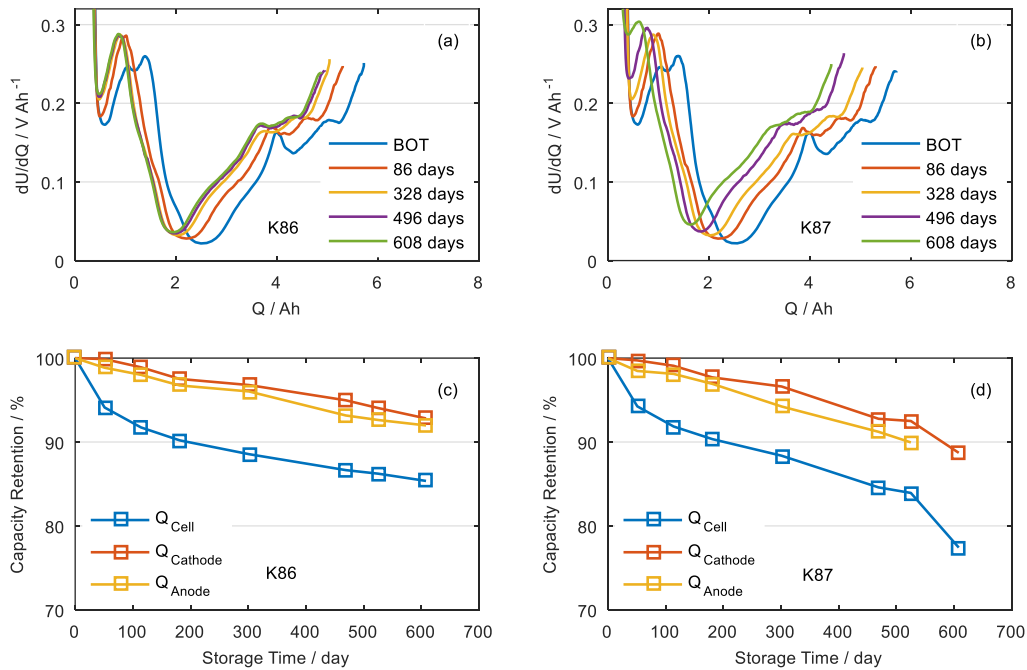


Figure 59. Charge DVA curve evolution of two cells stored at 55°C with the reference number (a) K86 and (b) K87; the active material loss according to the DVA of (c) K86 and (d) K87.

In Fig. 36, two cells (K86 and K87) begin to exhibit different aging behavior regarding capacity fade and ohmic resistance increase after 450 days storage at 55°C. Both cells had 87% normalized capacity at the point of split. The capacity fade of cell K86 in Figs. 59 (a) and 59 (c) obeys the root-function-like behavior, while the capacity fade of cell K87 in Figs. 59 (b) and 59 (d) accelerates slightly after 450 days and drastically after 500 days. In Fig. 59 (b), the last DVA curve at 608 days has no obvious A3 peak, thus there is no corresponding Q_{Anode} in Fig. 59 (d). Q_{Cathode} has a much faster loss in cell K87 than in cell K86 after 450 days. The cathode

is the limiting electrode in this cell type. The abrupt capacity decrease of cell K87 after 450 days originates most probably from the cathode side.

Additionally, a slight swelling is observed for cell K87 after 608 days storage. According to literature [206, 207], gas evolution during storage is a result of chemical reactions between surface free lithium compounds (e.g., Li_2CO_3 or LiOH) and electrolyte on the cathode/electrolyte interface. NCA cathode generates mainly CO_2 , while LCO cathode tends to generate a combination of CO and CO_2 .

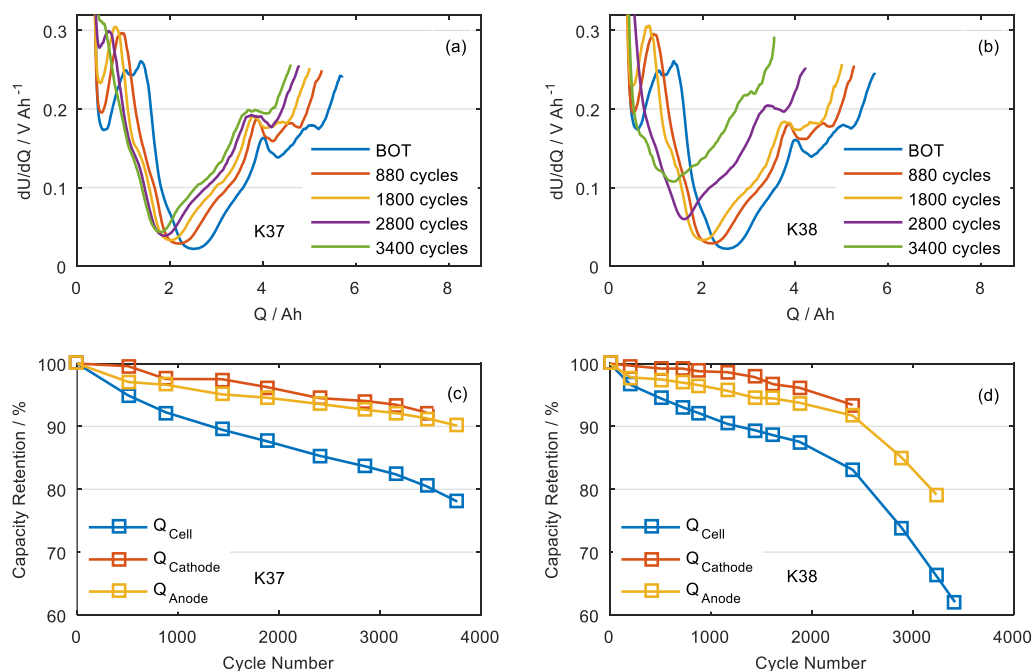


Figure 60. Charge DVA curve evolution of two cells cycled at 40°C with 1C charge/discharge with the reference number (a) K37 and (b) K38; the active material loss according to the DVA of (c) K37 and (d) K38.

In Fig. 40, the degradation plot of two cells (K37 and K38) cycled at 40°C begins to split after 2000 EFC in capacity. The DVA curves of both cells are presented in Fig. 60. Comparing Fig. 60 (c) to Fig. 60 (d), the major difference is the accelerate anode loss in cell K38. Although anode loss is not the direct reason for capacity loss due to 20% anode overdimension, it is probably a combination of anode degradation and LLI. Lithium plating due to anode surface degradation is considered as the reason for the roll-over effect in cell capacity fade by some researchers [44, 62]. The existence of plated lithium is proven by post-mortem analysis in Chapter 6.

5.2.3 ICA Method

Fig. 61 shows the ICA transformation of C/10 charge curves from Fig. 56. Figs. 61 (a)-(c) show the charge ICA curves of cells stored at 25°C, 40°C and 55°C. The three subplots show mainly the same evolution: the right-shift of the peak at 3.5 V and the decrease of the peaks at 3.8 V

and 3.95 V. High temperature expedites the evolution but the speed slows down with the storage time. According to Ref. [208], the combination of the offset in the region 3.4-3.6 V and the peak shrinkage at 3.8 V is a result of LLI.

Figs. 61 (d)-(f) show those cells cycled with 1C charge/discharge at 10°C, 25°C and 40°C ambient temperatures. Figs. 61 (g)-(i) show those cells cycled at 25°C ambient temperature with 1C charge and 1C, 3C or 5C discharge. The chosen aging states are BoT, 850 cycles, 3300 cycles and 5000 cycles. The ICA curve evolution in Figs. 61 (d)-(i) also shows the LLI aging pattern. The existence of anode and cathode loss is not excluded here, but it is more difficult to detect material loss with ICA than with DVA.

Comparing Fig. 57 (d) with Fig. 61 (d), the flattening slope of the DVA curve after 3300 cycles results in an accelerated decrease of the ICA peak at 3.8 V. At 5000 cycles, the cell in Fig. 61 (d) has a normalized capacity of 80.80%, while the cell in Fig. 61 (e) has a normalized capacity of 80.86%. They have similar capacity loss, but their ICA curves differ a lot at around 3.8 V. According to Ref. [208], in the case of pure LLI aging, the peak deformation at 3.5 V correlates with the peak deformation at 3.8 V. In Fig. 61 (d), the extra decrease of peak 3.8 V should be a result of electrode material degradation.

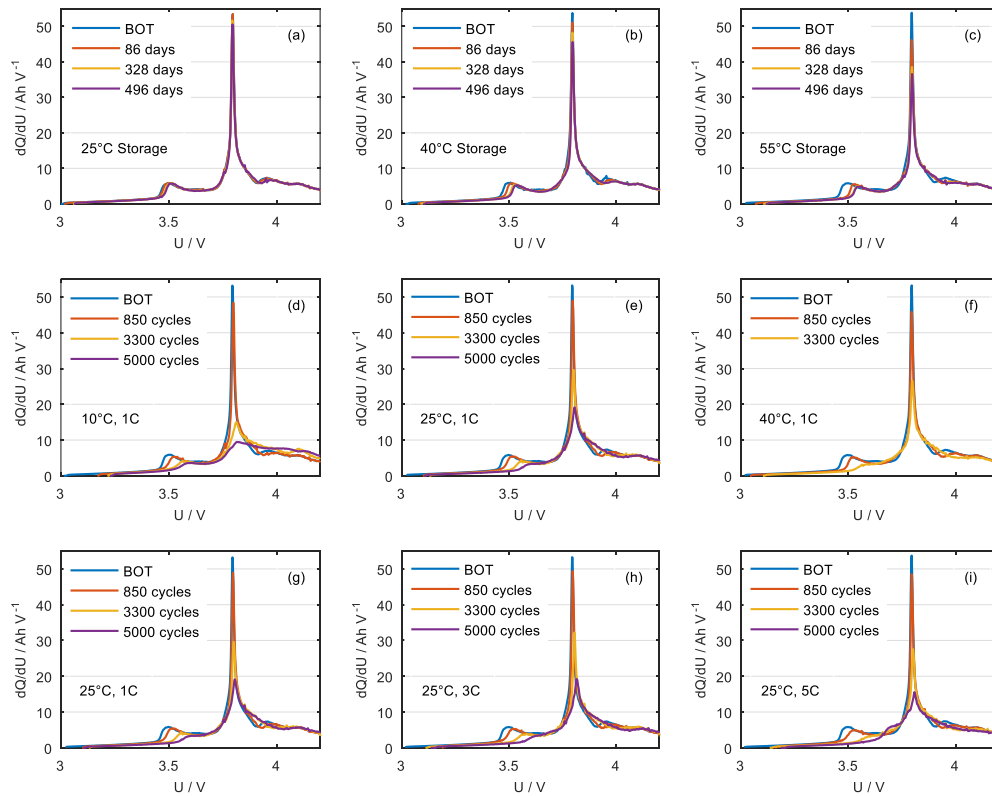


Figure 61. C/10 charge ICA curve evolution of a cell stored at (a) 25°C; (b) 40°C; (c) 55°C; or cycled at (d) 10°C, 1C; (e) 25°C, 1C; (f) 40°C, 1C; (g) 25°C, 1C; (h) 25°C, 3C; (i) 25°C, 5C.

According to Fig. 12 (a), the ICA peak at 3.8 V is characteristic of the cathode. Since the cathode consists of LCO and NCA, C/20 CC charge voltage data of the cathode materials are obtained from literature [142] for further analysis. The ICA curves of LCO and NCA and their superposition result are shown in Fig. 62 (a). The ICA curve of the blended cathode in Fig. 62 (a) is calculated from the cathode half cell charge voltage curve from Fig. 10 (b). The fitting result suggests a capacity ratio of 44:56 (LCO:NCA).

According to Fig. 62 (a), the ICA peak at around 3.9 V can be attributed to LCO. The voltage curve around 3.9 V correspondingly receives dominant influence from LCO. Fig. 62 (b) shows the DVA curves of the blended cathode and the LCO+NCA fitting. The curve from fitted literature data is in good agreement with the half cell measurement of the actual blended cathode. The flat voltage plateau, which leads to the valley in the DVA curve, corresponds to the dominant LCO peak in the ICA curve. Hence, in the case of 1C cycling at 10°C, there is LCO degradation in addition to LLI. It is not simply loss of LCO active material, but some irreversible material change of LCO, which alters its intercalation behavior.

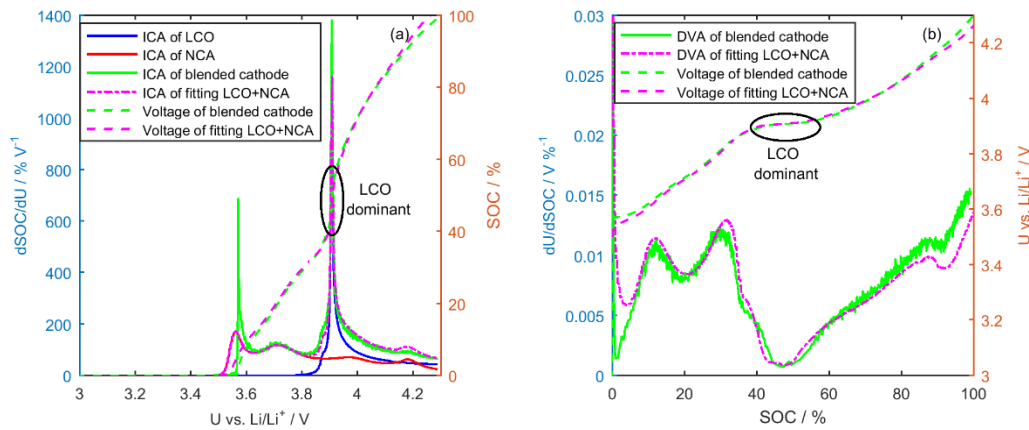


Figure 62. (a) ICA curves of both cathode components and their superposition fitting result compared with the actual blended cathode measurement; (b) the fitting result from (a) is transferred into DVA curves [5].

Fig. 11 and Fig. 12 in Subsection 3.2.2 have shown DVA and ICA evolution of six degradation modes. However, real aging condition is usually a combination of more than two degradation modes, which makes exhaustive aging interpretation with DVA and ICA difficult.

DVA is more suitable for the quantitative determination of LLI and LAM, if the characteristic peaks from both electrodes are clear to identify in the DVA curve. Nevertheless, the deformation of the DVA curve due to irreversible material change should be taken into consideration. Additionally, the precise determination of the distance between the characteristic DVA peaks is challenging. It is influenced not only by the measurement but also by the post-processing methods such as smooth algorithm and peak selection algorithm. The LLI and LAM calculated with DVA should thus be used more carefully. It is a useful tool to prove the existence of LLI/LAM and their relative amounts. However, if the accurate amount is crucial,

it is necessary to conduct half cell measurements on the aged cells. The values from the DVA interpretation can act as references.

Compared to DVA, the interpretation of ICA is not straightforward. However, the ICA method works well for the aging analysis of blended electrodes. A combination of DVA and ICA can compensate each other and make the aging analysis results more plausible.

5.3 Impedance-Based Aging Detection

The impedance-based aging detection is a comprehensive analysis of the EIS results, which have been regularly collected during the calendar and cycle life aging tests. The inductive part of the cell impedance is not discussed in this section, since it receives little influence from aging. The ohmic resistance part is already presented in Figs. 36 (b), 40 (b) and 44 (b). The focus of this section is on the cell impedance from medium to low frequencies.

5.3.1 Nyquist Plots

In order to get a profound understanding of the aging mechanisms of the tested cells, Nyquist plots acquired from the EIS measurements are presented in Fig. 63. Since the ohmic resistance is the real part of the impedance at zero crossing in a Nyquist plot and its evolution has already been shown in Section 5.1, the Nyquist plots are all normalized to the beginning zero crossing point in each case to give a better comparison of the resistances from medium to low frequencies.

In these Nyquist plots, two superimposed semi-circles and a sloping line can be observed. According to literature, the semi-circle at higher frequencies originates largely from the anode and is ascribed to the SEI layer [146, 152–157, 209], the semi-circle at medium frequencies represents mainly the double layer capacity and the charge transfer resistance of the cathode [147, 154, 158, 159, 210] and the slope at lower frequencies can be attributed to diffusion-limited processes [153, 158, 211, 212].

Figs. 63 (a)-(c) show the Nyquist plots of cells stored at 25°C, 40°C and 55°C. Four aging states are chosen: BoT, 86 days, 328 days and 496 days of storage. Both semi-circles increase with high temperature. It shows that both SEI growth and charge transfer resistance increase are temperature-dependent. At 40°C and 55°C storage, the boundary between the two semi-circles blurs and it seems to be one semi-circle. The increase of the semi-circle slows down after 86 days storage at 55°C in Fig. 63 (c), which coincides with the root-function-like degradation behavior in cell capacity and ohmic resistance.

Figs. 63 (d)-(f) show the Nyquist plots of cells cycled with 1C charge/discharge at 10°C, 25°C and 40°C. Four representative aging states are chosen: BoT, 850 cycles, 3300 cycles and 5000 cycles. The semi-circle at higher frequencies stays unchanged at 10°C and 25°C and increases gradually at 40°C. This confirms an intensified SEI growth at higher temperature, which has also been reported by other research groups [194, 213–216]. The temperature dependence of

the SEI growth is comprehensible, since the SEI growth comprises chemical reactions, like electrolyte decomposition and organic/inorganic compounds formation, which can be accelerated by high temperature [217, 218].

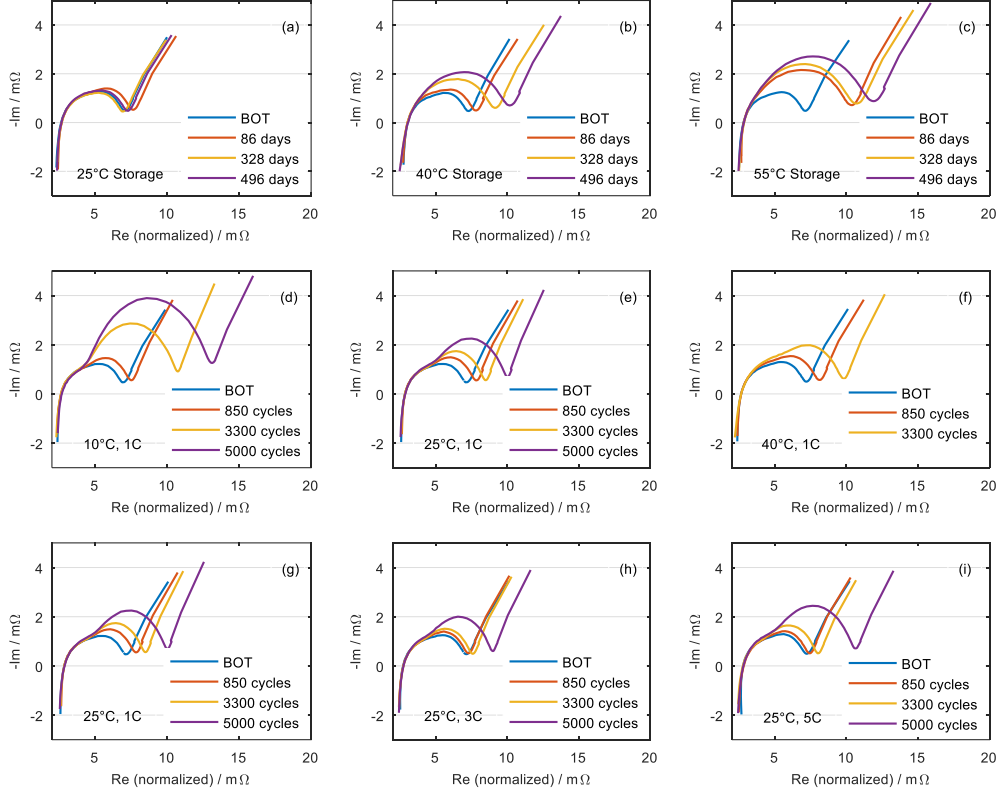


Figure 63. Normalized Nyquist plots of a cell stored at (a) 25°C; (b) 40°C; (c) 55°C; or cycled at (d) 10°C, 1C; (e) 25°C, 1C; (f) 40°C, 1C; (g) 25°C, 1C; (h) 25°C, 3C; (i) 25°C, 5C. All spectra of cycled cells have been left-shifted to the same zero-crossing of the x-axis as the spectrum at BoT.

The semi-circle at medium frequencies increases enormously after 850 cycles at 10°C. In the cases of 25°C and 40°C, the semi-circles at medium frequencies both increase steadily and 40°C show a faster increase. Due to a damage to the cell connection, Fig. 63 (f) shows only the aging states until 3300 cycles. The charge transfer resistance originates from the interface of electrolyte and electrodes, particularly the cathode side [219–224]. Passive layer growth and phase transitions on the cathode surface lead to a continuous increase of the charge transfer resistance. The massive charge transfer resistance increase at 10°C is probably owing to a crucial cathode material degradation, which has already been verified by means of DVA and ICA in the previous section.

Figs. 63 (g)-(i) show the influence of the discharge rate on the impedance spectra. Figs. 63 (e) and 63 (g) are identical. The semi-circle at higher frequencies keeps almost unchanged for all three discharge rates. The growth of the semi-circles at medium frequencies is suppressed by higher discharge rates at first. Only after 3300 cycles, i.e., shortly before 20% capacity loss,

they experience an abrupt increase (see Fig. 63 (h) and (i)). The suppression effect could be possibly explained by earlier cutoff of the CC discharge process at 3C and 5C, thus the cathode is less stressed by a high degree of lithiation. After 3300 cycles, severe cathode degradation takes place and hinders the charge transfer process.

5.3.2 Non-Ohmic Resistances

Non-ohmic resistances are directly related to the electrode surface characteristics of the cells. Different frequency ranges on the Nyquist plot are attributed to different chemical and physical processes inside the cell.

As shown in Fig. 64, between the two semi-circles at medium frequencies, there is a transition frequency of 66.7 Hz. Between the semi-circles and the sloping line, the minimum of the imaginary impedance Im_{\min} is recorded as a boundary. Hence, the non-ohmic resistances of the cell can be separated into SEI resistance R_{SEI} (1 kHz~67 Hz), charge transfer resistance R_{CT} (67 Hz~ Im_{\min}) and diffusion resistance R_{Diff} (Im_{\min} ~10 mHz). Fig. 64 is adapted from Fig. 15 in Subsection 3.2.3.

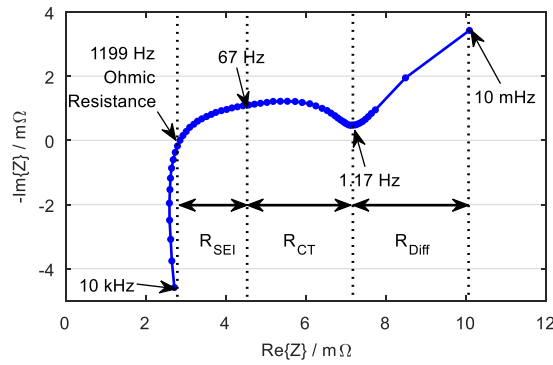


Figure 64. The definition of R_{SEI} , R_{CT} and R_{Diff} shown in a Nyquist plot of a fresh cell.

The non-ohmic resistances are extracted from all the Nyquist plots measured during the aging tests. The evolution of these non-ohmic resistances is displayed in Fig. 65.

For calendar aging, all three non-ohmic resistances increase at 40°C and 55°C in Figs. 65 (b) and 65 (c). They develop with root-function-like behavior. The change of the charge transfer resistance exceeds both SEI and diffusion resistances at 55°C storage in Fig. 65 (c). It relates with the cathode loss detected in Fig. 58 (c), since cathode degradation has a greater contribution to the charge transfer resistance.

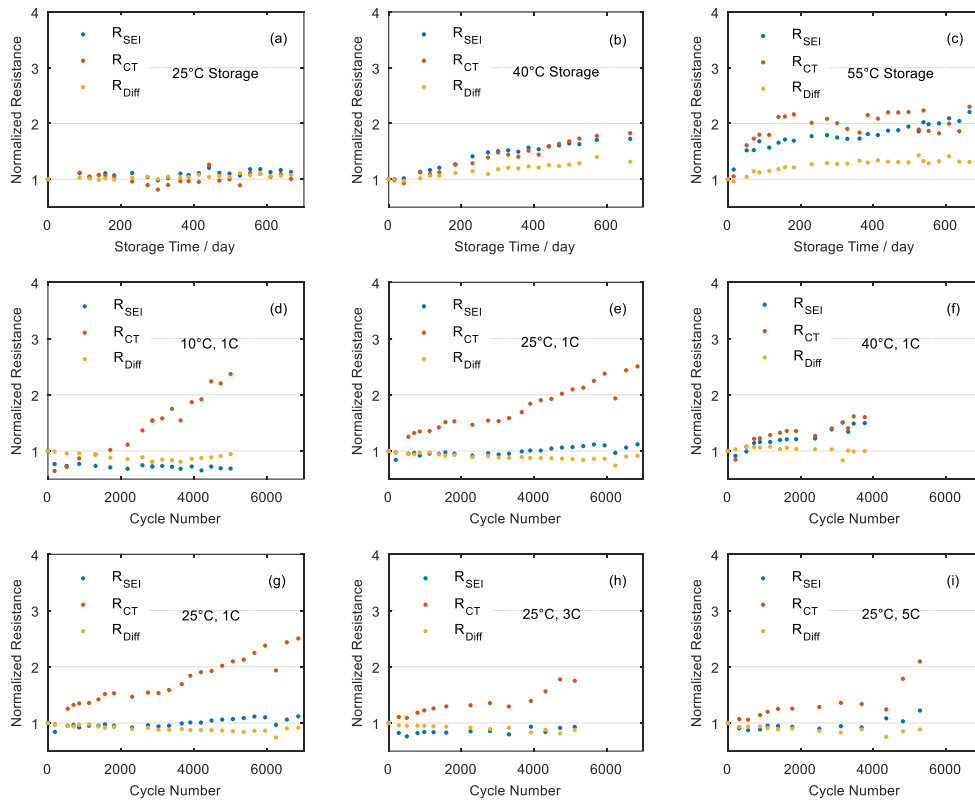


Figure 65. The evolution of the SEI resistance, charge transfer resistance and diffusion resistance of a cell stored at (a) 25°C; (b) 40°C; (c) 55°C; or cycled at (d) 10°C, 1C; (e) 25°C, 1C; (f) 40°C, 1C; (g) 25°C, 1C; (h) 25°C, 3C; (i) 25°C, 5C.

For cycle life aging, diffusion resistance stays almost unchanged in all cases in Figs. 65 (d)-(i). SEI resistance increases obviously in Fig. 65 (f) and only slightly in Figs. 65 (e), 65 (g) and 65 (i). SEI resistance is temperature-dependent. The charge transfer resistance has increased a lot in all cycling cases, especially for 1C cycling at 10°C and 25°C in Figs. 65 (d) and 65 (e). Under 3C and 5C discharge cycling in Figs. 65 (h) and 65 (i), charge transfer resistance has an abrupt increase shortly after 4000 cycles. Generally, the charge transfer resistance has the most pronounced increase among all the non-ohmic resistances for cycle life aging.

Nyquist plots and non-ohmic resistances are adopted to depict the aging split of the cell pairs: K86 versus K87 and K37 versus K38, which have already been analyzed with DVA in the previous subsection.

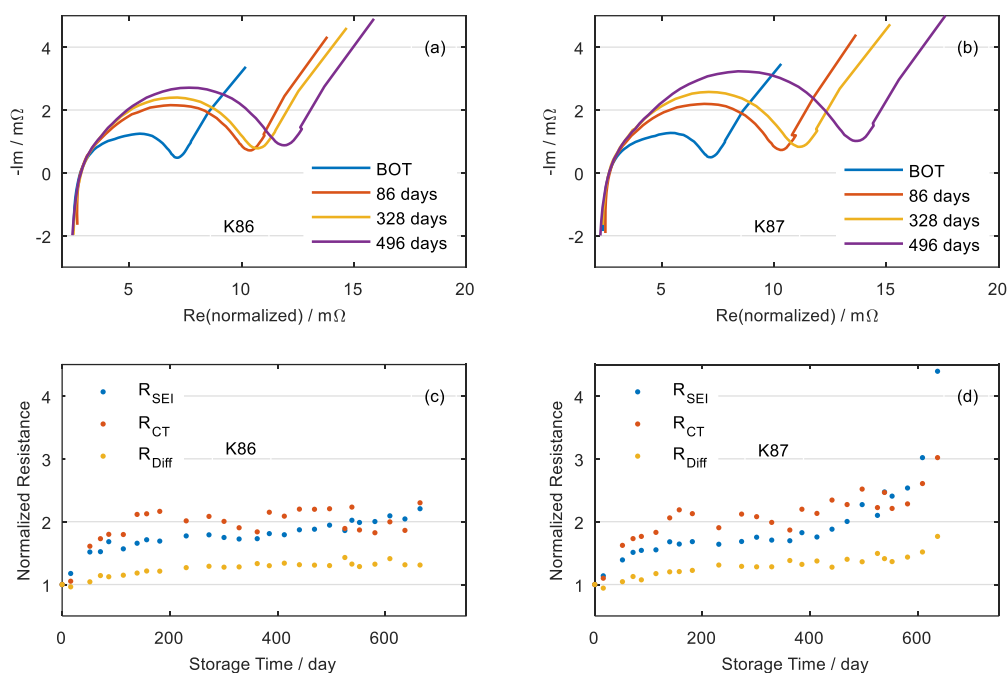


Figure 66. Normalized Nyquist plots of two cells stored at 55°C with the reference number (a) K86 and (b) K87; the evolution of the SEI resistance, charge transfer resistance and diffusion resistance of (c) K86 and (d) K87.

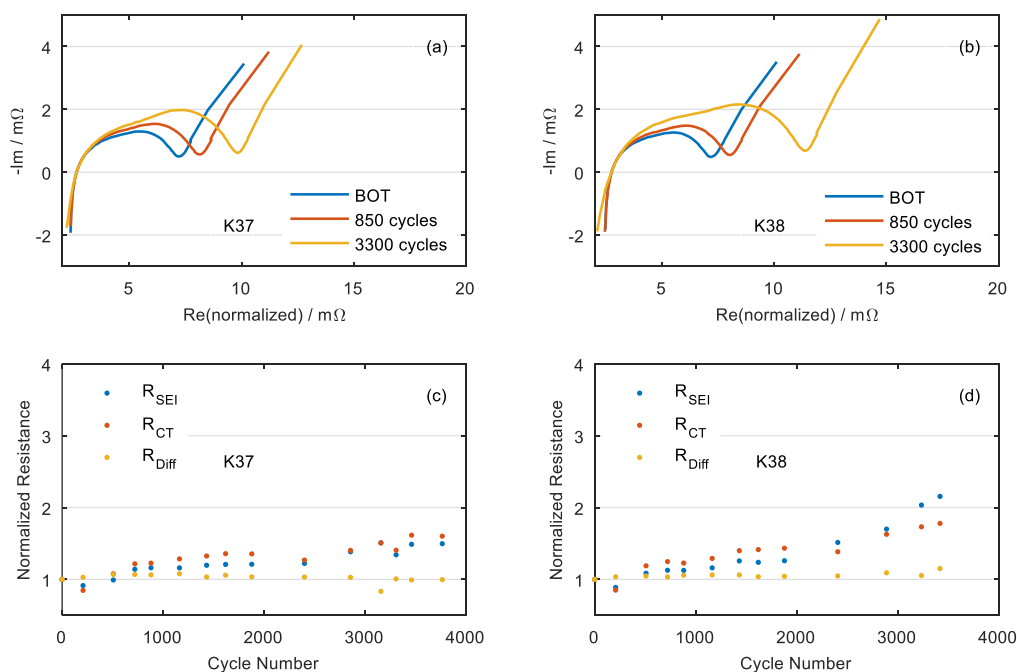


Figure 67. Normalized Nyquist plots of two cells cycled at 40°C with 1C charge/discharge with the reference number (a) K37 and (b) K38; the evolution of the SEI resistance, charge transfer resistance and diffusion resistance of (c) K37 and (d) K38.

The Nyquist plots and non-ohmic resistances of two cells (K86 and K87) stored at 55°C are shown in Fig. 66. The non-ohmic resistances of both cells increase in a similar root-function-like way before 450 days in Figs. 66 (c) and 66 (d). Afterwards, all non-ohmic resistances of cell K87 accelerate drastically. This phenomenon may relate with cathode loss and gas evolution inside the cell K87, as discussed in Subsection 5.2.2.

The Nyquist plots and non-ohmic resistances of two cells (K37 and K38) cycled with 1C at 40°C are shown in Fig. 67. The split of aging between both cells occurs after about 2000 cycles. In Figs. 67 (c) and 67 (d), their major difference after 2000 cycles is the evolution of SEI resistance. R_{SEI} grows much faster in cell K38 than in cell K37. In Fig. 60, there is also more anode loss in cell K38.

A possible explanation is that, the continuous growth of the SEI layer leads to an anode porosity drop and a large resistance increase at the anode/electrolyte interface. After a certain point, lithium plating begins and more parasitic reactions are triggered at the anode/electrolyte interface [44]. The SEI layer grows further due to more electrolyte decomposition compounds and both capacity and resistance degradation accelerates.

5.4 Temperature-Based Aging Detection

Temperature-based aging detection utilizes the evolution of cell entropy change in its value or its position. A change in its value means degradation in the electrode material. A change in its position unravels alignment change of both electrodes or a different degradation of the blended materials in one electrode.

The measurement of the absolute entropy change values usually takes several weeks, since different temperatures, different SoCs and long relaxation time should be included. Section 5.4 is mainly focused on the position shift of entropy change, which requests less expenditure and can be achieved during a dynamic process. It is believed to be more promising for on-line diagnosis application.

5.4.1 Surface Temperature Distribution

In Subsection 3.2.4.2, the Biot number of the examined cell is lower than 0.1 and thus the cell can be treated as an object with homogeneous temperature distribution. Nonetheless, temperature distribution test was carried out on the cell surface to ensure that the surface center temperature is representative for the whole cell.

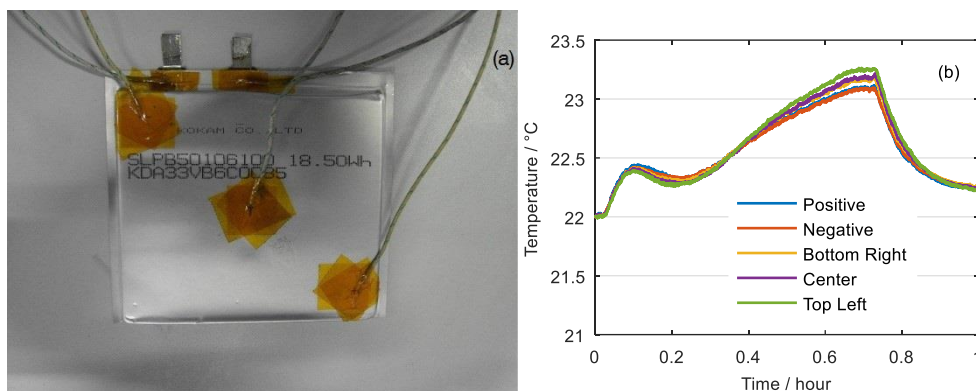


Figure 68. (a) Positions of five temperature sensors on the cell surface; (b) temperature evolution of the temperature sensors during a 1.5C CCCV charge process at room temperature.

Fig. 68 (a) shows the positions of five temperature sensors on the cell surface and Fig. 68 (b) shows the evolution of their temperatures during a 1.5C CCCV charge process. The ambient temperature during the test is 22°C. The original temperature values are all adjusted to 22°C at the beginning. The temperature difference between the five sensors is within 0.2°C. The top left point shows the highest temperature at the end of the CC phase, while the positive and negative tabs show the lowest temperatures. The temperature of the center point is in the middle range, which is appropriate for the following temperature analysis.

5.4.2 Temperature Variation Analysis

The temperature variation rate dT/dt , defined in Eq. 40, includes irreversible Joule heat, reversible reaction heat and heat exchange with the environment. It can be easily collected during the cell operation. If the absolute temperature change is low, the thermal parameters can be considered as constant and the heat exchange with the environment is negligible. The charge resistance is proven to be constant in the SoC range of 20% to 100% in Subsection 3.2.4.3. Hence, the temperature variation rate can be adopted to detect the change of reversible reaction heat or entropy change under CC operational condition.

5.4.2.1 Temperature Increase during Charge/Discharge

As depicted in Subsection 3.2.4.2, the heat generation of a cell during CC charge or discharge consists primarily of Joule heat and reaction heat. The Joule heat increases approximately quadratically with the current and linearly with the cell resistance. The reversible reaction heat varies linearly with the current, the temperature and the entropy change.

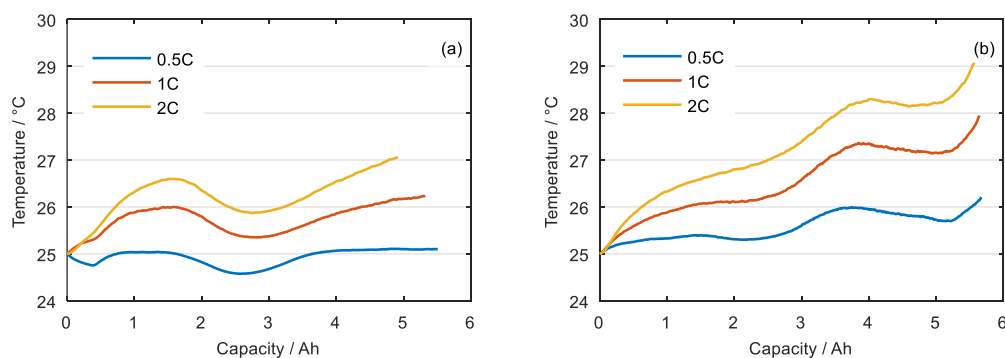


Figure 69. Temperature evolution at the surface center point of a fresh cell during 0.5C, 1C and 2C (a) charge; (b) discharge in a climate chamber at 25°C.

Fig. 69 shows the surface center temperature of a fresh cell charged and discharged with various C-rates. The temperature develops in a similar way and rises with higher C-rates. The temperature rise during discharge is higher than that during charge at the same C-rate. Additionally, there is an obvious temperature minimum in the middle of the charge process, which is not in the case of discharge. This temperature minimum is owing to the reversible reaction heat or more specifically the entropy change. Hence, for the investigated cell, the charge process is more appropriate for entropy change detection than the discharge process.

Furthermore, the lower temperature rise during charge has less influence on the thermal parameters of the cell. Since the regular capacity tests are conducted with 1C, the following temperature variation analysis is based on 1C charge.

5.4.2.2 Temperature Variation Rate

As discussed in Subsection 3.2.4.3, the 10s-charge resistance of the examined cell stays almost constant above 20% SoC under various aging conditions. Thus, in the range of 20-100% SoC, the temperature variation rate varies only with the entropy change ΔS during 1C CC charge.

Fig. 70 illustrates the temperature evolution and the temperature variation rate of one cell during 1C CC charge from 2.7 V to 4.2 V. This cell is cycled with 1C charge and discharge at 25°C. Fig. 70 (a) and Fig. 70 (b) show the temperature evolution of the same cell at the fresh state and after 6000 cycles, respectively.

As shown in Fig. 70 (a), there are two remarkable cooling areas ($dT/dt < 0$) in the charge process, i.e., the one in the first 0.05 h and the other at around 0.42 h (38% SoC). According to Subsection 3.2.4.3, the Joule heat for CC charging should be higher in the range of 0-20% SoC and nearly constant from 20% to 100% SoC. The heat dissipation changes only slightly, since the cell temperature change stays within 0.8°C. Hence, both cooling areas should be attributed to the reaction heat and the entropy change.

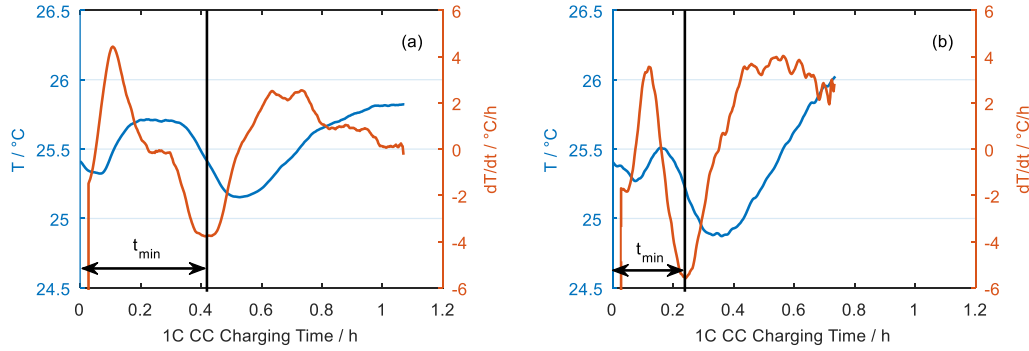


Figure 70. Evolution of the temperature and its variation rate of a cell cycled with 1C charge/discharge during a 1C CC charge process in a climate chamber at 25°C: (a) at BoT (100% SoH); (b) after 6000 cycles (75% SoH) [9].

In Fig. 70 (b), the two cooling areas are still observable after 6000 cycles. However, the one at around 0.42 h in Fig. 70 (a) has left-shifted to around 0.25 h, which corresponds to 30% SoC for the aged cell. The temperature change has increased to 1.2°C. The period from the charge begin to the dT/dt minimum in the second cooling area is defined as t_{\min} , which is proven as a useful SoH indicator in the following subsection.

5.4.2.3 t_{\min} vs. Aging Detection

As depicted in Subsection 3.2.4.1 and Fig. 20, the first cooling area of the entropy change curve of a Kokam cell originates from the graphite anode in its initial lithium intercalation phase. The second cooling area relates to the blended cathode. Therefore, the two cooling areas can be regarded as characteristics of the anode and the cathode, respectively.

According to Subsection 3.2.2.2, capacity fade of a LIC has three origins, loss of anode active material, loss of cathode active material and loss of lithium inventory (LLI) [137]. The last is the predominant degradation mechanism in the normal operation range of commercial LICs, especially in the initial aging phase [73, 129, 199, 225, 226]. As LLI increases, the anode gets more lithiated at the end of discharge, resulting in a shift between the anode and cathode voltage profiles towards each other [137] as shown in Fig. 71. If LLI is the only existing degradation mechanism for capacity fade, the offset between both electrodes should correlate with capacity fade. In Fig. 70, the time from the begin of charge to the dT/dt minimum represents the offset between both electrodes, since they originate from the anode and the cathode, respectively. This assumption is validated later with the experimental data of the examined cells.

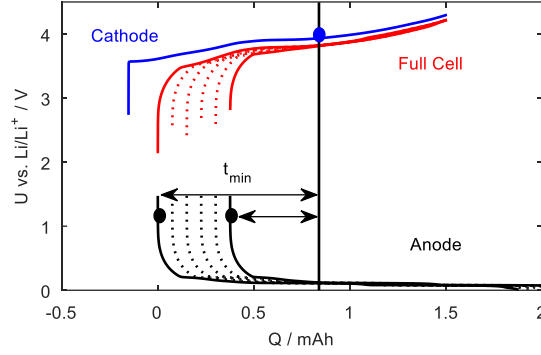


Figure 71. Schematic of the degradation mechanism of LLI [9, 137].

Firstly, t_{\min} is extracted from the 1C CC charge process in the regular performance tests. *Moving Average Filtering* and *Findpeaks* functions in Matlab are applied to the data post-processing. SoH is then determined with discharge capacity (CC+CV) at the corresponding aging state according to Eq. 10.

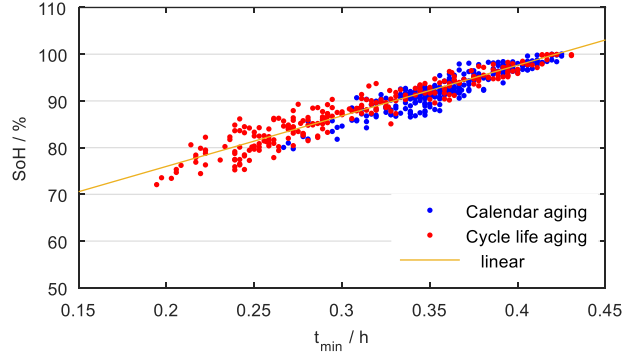


Figure 72. Scatter plot of t_{\min} and SoH of 287 calendar aging states and 257 cycle life aging states with a trend line [9].

Fig. 72 shows a scatter plot of t_{\min} and SoH with a trend line. It includes 20 cells and their 544 aging states, among which there are 287 calendar aging states and 257 cycle life aging states. The cells cycled with 1C at 10°C are not included here, since they show obvious cathode degradation in their DVA curves. The product-moment correlation coefficient or Pearson's r is employed to measure the association between t_{\min} and SoH:

$$r = \frac{\sum_{i=1}^n (x_i - \bar{x})(y_i - \bar{y})}{\sqrt{\sum_{i=1}^n (x_i - \bar{x})^2 \cdot \sum_{i=1}^n (y_i - \bar{y})^2}} \quad (96)$$

Where (x_i, y_i) , $i=1, \dots, n$ are pairs of quantities, \bar{x} is the mean of all the x_i and \bar{y} is the mean of all the y_i . Pearson's r varies between -1 and 1. When (x_i, y_i) lie on a perfect straight line with positive slope, also known as “complete positive correlation”, r equals 1. If r equals zero, x_i and y_i are uncorrelated. If r equals -1, they have “complete negative correlation” [227]. The calculated Pearson's r for 544 pairs of t_{\min} and SoH is 0.954, which suggests a strong positive correlation. The results show a strong linear dependence between t_{\min} and SoH of our tested cells under all

the experimental conditions. Based on the linear least squares regression analysis, the cell SoH can be expressed with the following equation:

$$SoH = 1.07t_{\min} + 0.543 \quad (97)$$

In Fig. 72, the scatter points at lower SoH are further away from the trend line than those at higher SoH. It could be explained with the fact that, near EoL there is not only LLI but also more or less loss of cathode material in the cells. Since the 544 aging states include 7 different operational conditions, it is important to ensure that the trend line works for each condition separately. Fig. 73 presents the aging states from 6 operational conditions and their positions along the same correlation line (Eq. 97). The seventh operational condition that is not shown in Fig. 73 is 25°C storage, since the SoH change under this condition is not evident.

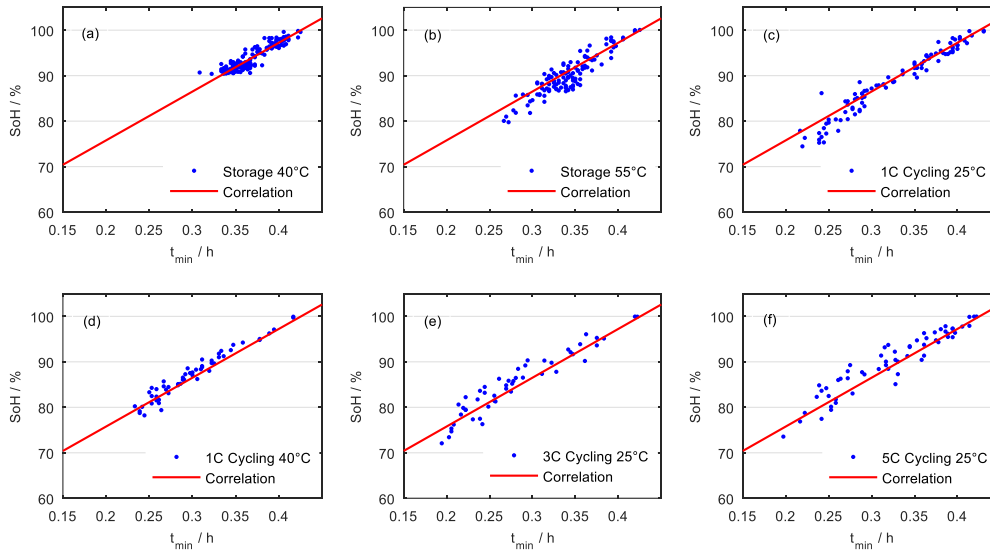


Figure 73. Scatter plots of t_{\min} and SoH under different operational conditions: (a) storage at 40°C; (b) storage at 55°C; (c) 1C charge/discharge cycling at 25°C; (d) 1C charge/discharge cycling at 40°C; (e) 3C discharge cycling at 25°C; (f) 5C discharge cycling at 25°C. The same correlation line is used to compare with the (t_{\min}, SoH) -pairs in different groups.

In Figs. 73 (a)-(c), the correlation line is almost in the middle of the aging states, while in Figs. 73 (d)-(f) the correlation line is below the majority of the aging states. As explained in Subsection 5.2.2, severe operational conditions in Figs. 73 (d)-(f) lead to more anode and cathode material loss besides LLI. Additionally, 3C and 5C cycling conditions have more scattered aging states similar to their capacity fade and ohmic resistance rise behavior.

5.4.2.4 Current Optimization

Until now, all the t_{\min} values are extracted from the 1C CC charge process, since it is part of the regular capacity test. In reality, different charge currents could be used. It is already known that the irreversible heat increases quadratically with the current and the reversible heat increases

linearly with the current. A change in the current alters the proportion of irreversible heat to reversible heat during the CC charge process.

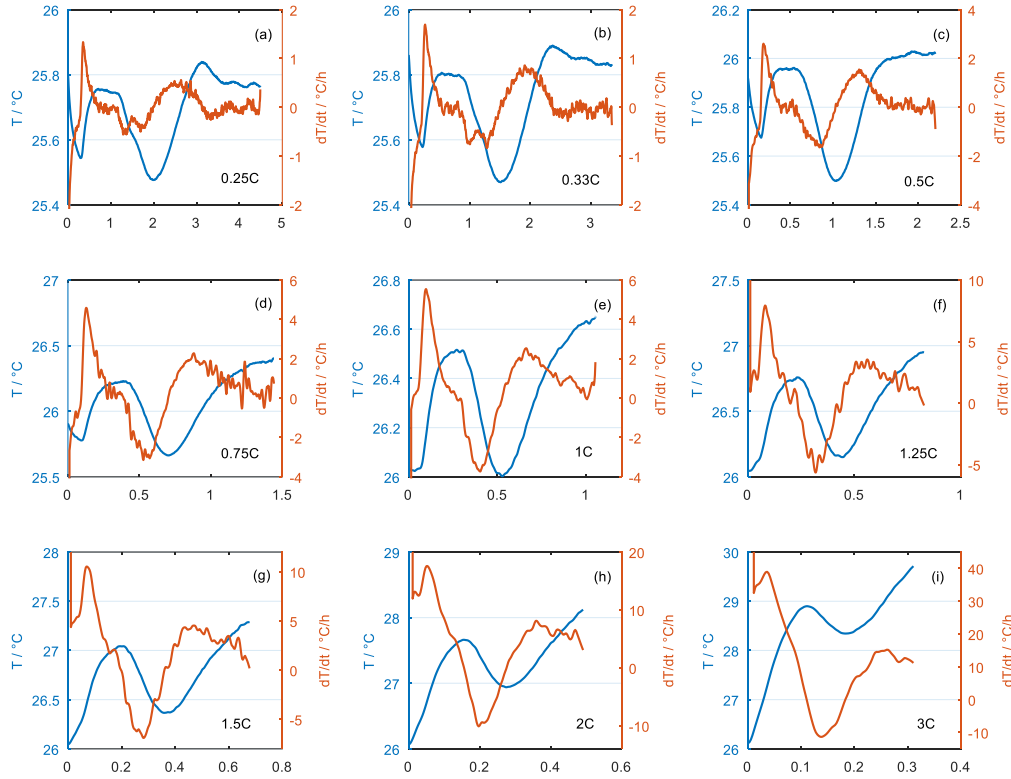


Figure 74. Evolution of the temperature and its variation rate of a fresh cell CC charged at 25°C with (a) 0.25C; (b) 0.33C; (c) 0.5C; (d) 0.75C; (e) 1C; (f) 1.25C; (g) 1.5C; (h) 2C; (i) 3C. The tests were conducted in the same temperature chamber at 25°C and the same charge current was repeated at least twice to ensure reproducibility.

Fig. 74 provides an overview of the temperature evolution and the temperature variation rate during CC charge processes with 0.25C to 3C. For 0.25C, 0.33C and 0.5C, the temperature variation is quite low and t_{\min} is not clear to identify. For higher currents, the dT/dt minimum is obvious. However, the temperature change rises with the current, e.g., the temperature during 3C charge has increased almost 4°C. High temperature increase may cause noticeable change in the heat dissipation term in Eq. 40, which is assumed to be constant during the CC charge process. Hence, the recommended current for the examined cell for t_{\min} analysis is between 0.75C and 2C.

The temperature-based aging detection introduced in this section is different from the current-voltage-based aging detection in Section 5.2 and the impedance-based aging detection in Section 5.3. It is not focused on the detailed interpretation of aging mechanisms. Based on the analysis results from Section 5.2 and Section 5.3, LLI is known as the most pronounced aging mechanism for capacity fade of the examined cells under various operational conditions. LLI

represents a shift between the electrodes. The shift can be measured with the relative position change of voltage plateaus, which are characteristics of both electrodes, as illustrated in Section 5.2. The electrodes also have their own entropy change curves, which can provide similar features of the electrodes in the cell temperature variation. The assumption is validated with the experimental data and thus temperature measurement can be used to predict capacity loss for the examined cell.

6. Post-Mortem Analysis

Although the focus of this thesis work is non-invasive aging detection, some post-mortem analysis is carried out to validate the aging prediction. A fresh cell and an aged cell cycled with 1C charge/discharge at 40°C were disassembled to reveal the aging mechanisms. The aged cell is the one with roll-over effect in Fig. 40.

Both cells were CCCV discharged to 0% SoC and taken apart in an Argon-filled glovebox. The examined cell has 17 double-side-coated copper foils with anode, 16 double-side-coated aluminum foils with cathode and 2 single-side-coated aluminum foils with cathode. Fig. 74 shows the condition of the electrodes inside the fresh cell. The electrodes wrapped in separator were soaked with electrolyte and in good conditions at first view.

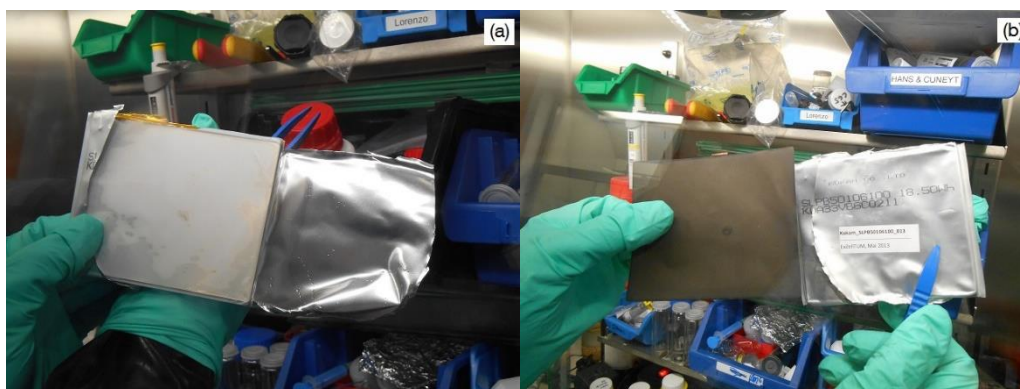


Figure 74. Photos of the fresh cell after disassembly: (a) electrodes wrapped in separator; (b) an anode sheet.

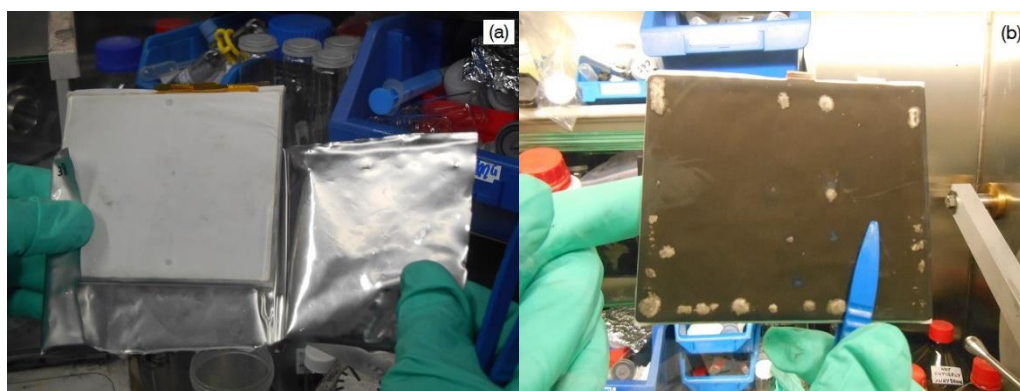


Figure 75. Photos of the aged cell after disassembly: (a) electrodes wrapped in separator; (b) an anode sheet.

Fig. 75 shows the condition of the electrodes inside the aged cell. After opening the pouch foil, the cell was not visibly wet and there was little electrolyte in the cell. It was almost dry-out, which explained the extremely high ohmic resistance of the cell. Each anode sheet had silver

shimmering particles on it as shown in Fig. 75 (b). They were believed to contain lithium metal, since they turned into bubbles and flames when soaked into water. Lithium plating occurred in the aged cell, thus its capacity fade had a roll-over effect after 2000 EFCs. The plated lithium reacted with the electrolyte and ultimately led to dry-out of the cell.

Slices were stamped out of the electrodes of both cells. They were washed with dimethyl carbonate. After drying overnight, SEM analysis was conducted on the electrode slices. The results are presented in Fig. 76. Compared to the fresh anode, the graphite layered structure in the aged anode is less obvious. In Figs. 76 (c) and 76 (d), there is no significant difference between the fresh and the aged cathode.

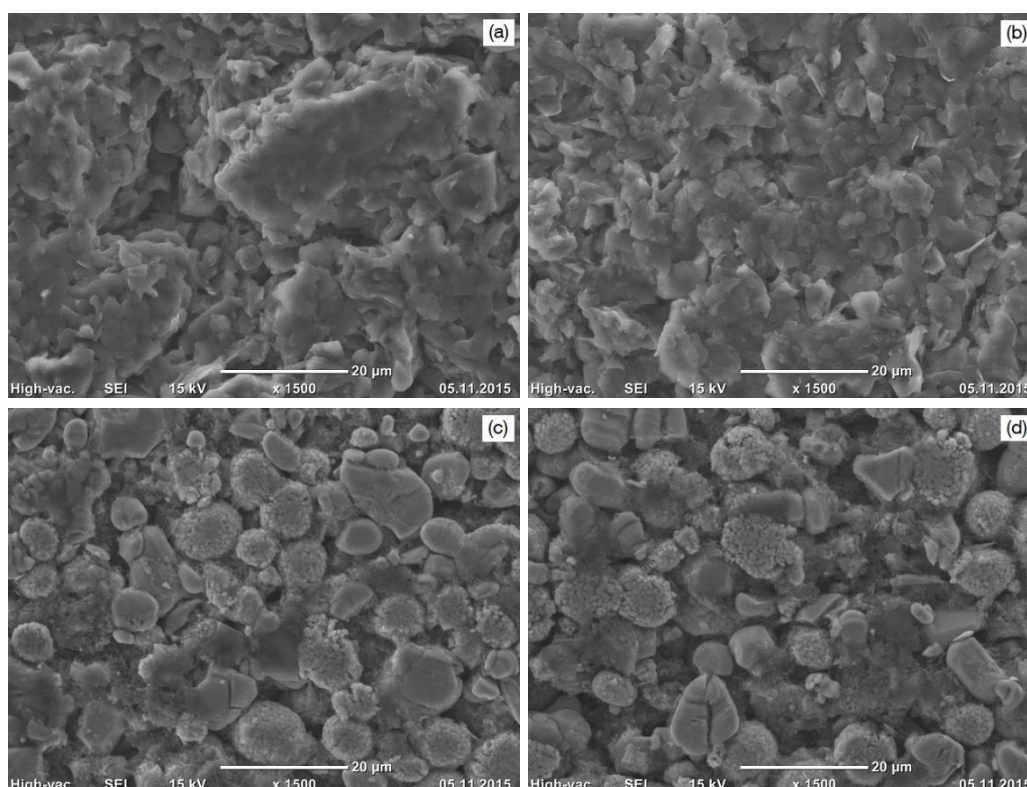


Figure 76. SEM images of the surface structure of the (a) fresh anode; (b) aged anode; (c) fresh cathode; (d) aged cathode.

7. Conclusion and Outlook

Calendar aging tests and cycle life aging tests were carried out on 5 Ah pouch LICs with an LCO/NCA blended cathode and a graphite anode. Temperature and storage time are investigated as stress factors for calendar aging, while temperature, discharge current, charge current and Ah-throughput are investigated for cycle life aging. Empirical aging models are established based on these stress factors to describe the degradation behavior of the tested LICs regarding capacity and ohmic resistance.

Both capacity fade and ohmic resistance increase due to calendar aging develop in a root-function-like way with storage time. The dependence of their degradation rates on temperature agrees with the Arrhenius law. The activation energy of ohmic resistance increase (63 kJ/mol) almost doubles that of capacity fade (35 kJ/mol).

As for pure cycle life aging, capacity fade and ohmic resistance increase develop both in a quasi-linear way with Ah-throughput. The dependence of capacity fade rate on temperature is quadratic, with 25°C for the lowest capacity fade rate. The dependence of ohmic resistance increase rate on temperature also follows the Arrhenius law. Both high discharge current and high charge current accelerate the degradation rates of capacity and ohmic resistance. The increase of discharge current has a more pronounced impact on ohmic resistance increase than capacity fade. By contrast, the increase of charge current has a greater influence on capacity fade than ohmic resistance increase.

In addition to capacity and ohmic resistance analysis, non-invasive aging detection methods are adopted to reveal internal aging mechanisms of the tested LICs under various operational conditions. The involved aging detection methods are categorized into current-voltage-based methods, impedance-based methods and temperature-based methods.

The employed current-voltage-based methods are DVA and ICA. The former can track the changes in cyclable lithium amount and electrode active material amount quantitatively, if the electrodes have visible characteristic voltage plateaus in the OCV. The DVA results show that loss of cyclable lithium is the dominant aging mechanism for all operational conditions. There is also slight active material loss in the anode and cathode near EoL. An exception is the LIC cycled at 10°C, where extremely high cathode loss is detected. The quantitative DVA detection contains inevitable inaccuracies from measurement precision, data post-processing and material degradation. Hence, the quantitative results should be used carefully.

ICA offers similar aging information to DVA, but in a more indirect way. The advantage of ICA is that it can separate the degradation of the cathode composite materials LCO and NCA.

The cathode degradation in the case of 10°C cycling is attributed to an irreversible material change in LCO with the aid of ICA.

EIS measurement is representative of impedance-based detection methods. Besides the aforementioned ohmic resistance increase, non-ohmic resistances from 1 kHz to 10 mHz also rise as aging intensifies. The non-ohmic resistances are divided into SEI resistance, charge transfer resistance and diffusion resistance based on their frequency ranges.

The EIS results show that SEI resistance only increases at an operation temperature above 25°C. The charge transfer resistance grows significantly under all the test conditions except for 25°C storage. The extremely high charge transfer resistance in the case of 10°C cycling relates probably with the LCO degradation in the blended cathode. The diffusion resistance presents minor growth only when the LICs are stored above 25°C.

The temperature-based detection method shows an alternative way to estimate capacity loss. The method determines the offset of the electrode balance, which corresponds to the loss of cyclable lithium. During a CC charge process, the offset is detected by means of a temperature variation rate minimum, which is an entropy change feature of the cathode. Since loss of cyclable lithium is proven as the dominant aging mechanism for capacity loss with current-voltage-based methods, capacity loss should correlate with the offset of the electrode balance, i.e., the position of the temperature variation rate minimum.

The assumption is validated with the aging data. It works for all the test conditions except for the case of 10°C cycling, which is known to have severe cathode degradation. The method provides a possible way to combine temperature monitoring and SoH estimation. However, this detection method requires at least a minimum or a maximum in the full cell entropy change during the charge or discharge process. Many LIC cathode materials have relatively flat entropy change curves. As for a LIC with a blended cathode, the entropy change curves of the cathode components should be distinguishable enough to generate such a minimum/maximum in the full cell entropy change profile.

Based on the aging results, some suggestions are summarized for the utilization of LICs. Lithium plating is usually considered as a risk during low temperature operation. However, it is also observed at 40°C cycling in the examined LIC. The existence of lithium plating should always be taken into consideration during the design of battery systems. On the other hand, there are no signs, that 10°C cycling causes lithium plating in the examined LIC. The cells suffer primarily from charge transfer resistance increase and cathode degradation due to LCO. Hence, for applications below room temperature, LCO cathode should be avoided.

During the literature survey and the experimental work, there are some common problems in the application of non-invasive aging detection methods, which should be addressed in the future. For example, in-depth knowledge of the electrode chemistry is always a requisite. The interpretation depends immensely on the electrode materials and thus there is hardly a universal

detection method for all types of LIC technologies. Furthermore, quantitative methods such as DVA and the temperature-based method rely considerably on the data post-processing, which brings some inaccuracies into the detection results. It is ideal to combine quantitative electric detection methods with post-mortem analysis to evaluate the reliability and precision of such non-invasive aging detection methods.

Appendix I

A.1 BaSyTec Test Protocols for Performance Tests and Cycling Tests

All test procedures conducted within this thesis are presented in detail in this section.

Table A.1-1. Basic performance test

Step No.	Step Name	Parameter	Termination
1	Pause		$t > 2 \text{ h}$
2	Charge CCCV	$I = 5 \text{ A}$ $U = 4.2 \text{ V}$	$I < 0.25 \text{ A}$
3	Pause		$t > 10 \text{ min}$
4	Discharge CC	$I = -5 \text{ A}$	$U > 4.2 \text{ V}$
5	Discharge CV	$U = 2.7 \text{ V}$	$I > -0.25 \text{ A}$
6	Pause		$t > 10 \text{ min}$
7	Charge CCCV	$I = 5 \text{ A}$ $U = 4.2 \text{ V}$	$I < 0.25 \text{ A}$
8	Pause		$t > 10 \text{ min}$
9	Discharge CC	$I = -5 \text{ A}$	$U > 4.2 \text{ V}$
10	Discharge CV	$U = 2.7 \text{ V}$	$I > -0.25 \text{ A}$
11	Pause		$t > 10 \text{ min}$
12	Charge CC	$I = 5 \text{ A}$	$\text{SoC} > 50\%$
13	Pause		$t > 30 \text{ min}$
14	Stop		

Table A.1-2. Extended performance test

Step No.	Step Name	Parameter	Termination
1	Pause		$t > 2 \text{ h}$
2	Charge CCCV	$I = 5 \text{ A}$ $U = 4.2 \text{ V}$	$I < 0.25 \text{ A}$
3	Pause		$t > 10 \text{ min}$
4	Discharge CC	$I = -5 \text{ A}$	$U > 4.2 \text{ V}$
5	Discharge CV	$U = 2.7 \text{ V}$	$I > -0.25 \text{ A}$
6	Pause		$t > 10 \text{ min}$
7	Charge CCCV	$I = 5 \text{ A}$ $U = 4.2 \text{ V}$	$I < 0.25 \text{ A}$
8	Pause		$t > 10 \text{ min}$
9	Discharge CC	$I = -5 \text{ A}$	$U > 4.2 \text{ V}$
10	Discharge CV	$U = 2.7 \text{ V}$	$I > -0.25 \text{ A}$
11	Pause		$t > 10 \text{ h}$
12	Charge CC	$I = 0.5 \text{ A}$	$U > 4.2 \text{ V}$
13	Charge CV	$U = 4.2 \text{ V}$	$I < 0.25 \text{ A}$
14	Pause		$t > 1 \text{ h}$
15	Discharge CC	$I = -0.5 \text{ A}$	$U < 2.7 \text{ V}$
16	Discharge CV	$U = 2.7 \text{ V}$	$I > -0.25 \text{ A}$
17	Pause		$t > 10 \text{ min}$
18	Charge CC	$I = 5 \text{ A}$	$\text{SoC} > 50\%$
19	Pause		$t > 6 \text{ h}$
20	Stop		
21	Go to EIS test		

Table A.1-3. Cycle life test

Step No.	Step Name	Parameter	Termination
1	Pause		$t > 30 \text{ min}$
2	Cycle-start		
3	Discharge CC	$I = -5 \text{ A}$ (-10 A or -15 A)	$U < 2.7 \text{ V}$
4	Pause		$t > 5 \text{ min}$
5	Charge CCCV	$I = 5 \text{ A}$ (2.5 A, 10 A or 15 A) $U = 4.2 \text{ V}$	$I < 0.25 \text{ A}$
6	Cycle-end	Count=100	
7	Discharge CC	$I = -5 \text{ A}$	$U < 3.6 \text{ V}$
8	Pause		$t > 10 \text{ min}$
9	Stop		

Table A.1-4. DC pulse resistance test

Step No.	Step Name	Parameter	Termination
1	Pause		$t > 2 \text{ min}$
2	Discharge CC	$I = -5 \text{ A}$	$U < 2.7 \text{ V}$
3	Discharge CV	$U = 2.7 \text{ V}$	$I > -0.25 \text{ A}$
4	Pause		$t > 30 \text{ min}$
5	Cycle-start		
6	Charge CC	$I = 5 \text{ A}$	$t > 30 \text{ s}$
7	Pause		$t > 10 \text{ min}$
8	Charge CC	$I = 5 \text{ A}$	SoC $> 5\%$, $U > 4.2 \text{ V}$ (SoC: 10%, 20%, 30%, 40%, 50%, 60%, 70%, 80%, 90%, 95%)
9	Pause		$t > 30 \text{ min}$
10	Cycle-end	SoC = 95%	
11	Charge CC	$I = 5 \text{ A}$	$t > 30 \text{ s}$
12	Pause		$t > 10 \text{ min}$
13	Charge CCCV	$I = 5 \text{ A}$ $U = 4.2 \text{ V}$	$I < 0.25 \text{ A}$
14	Pause		$t > 30 \text{ min}$
15	Cycle-start		
16	Discharge CC	$I = -5 \text{ A}$	$t > 30 \text{ s}$
17	Pause		$t > 10 \text{ min}$
18	Discharge CC	$I = -5 \text{ A}$	SoC $< 95\%$, $U < 2.7 \text{ V}$ (SoC: 90%, 80%, 70%, 60%, 50%, 40%, 30%, 20%, 10%, 5%)

19	Pause		$t > 30 \text{ min}$
20	Cycle-end	$\text{SoC} = 5\%$	
21	Discharge CC	$I = -5 \text{ A}$	$t > 30 \text{ s}$
22	Pause		$t > 10 \text{ min}$
23	Charge CC	$I = 5 \text{ A}$	$U > 3.6 \text{ V}$
24	Pause		$t > 30 \text{ min}$
25	Stop		

A.2 Biologic Test Protocols for Electrochemical Impedance Spectroscopy

The following table shows the test settings for the EIS measurement done on a potentiostat VMP3 by Biologic Science Instruments.

Table A.2-1. EIS measurement settings

Stage I	
Excitation Signal Mode	Single sine
Frequency Range	100 kHz ~ 2.1 Hz
Points per Decade	12 (in logarithmic spacing)
Current Amplitude	200 mA
Wait for	0.1 period before each frequency
Average	10 measures per frequency
Stage II	
Excitation Signal Mode	Single sine
Frequency Range	1.93 Hz ~ 100 mHz
Points per Decade	10 (in logarithmic spacing)
Current Amplitude	200 mA
Wait for	0.1 period before each frequency
Average	5 measures per frequency
Stage III	
Excitation Signal Mode	Single sine
Frequency Range	90 mHz ~ 10 mHz
Points per Decade	3 (in logarithmic spacing)
Current Amplitude	100 mA
Wait for	0.1 period before each frequency
Average	2 measures per frequency

Appendix II

All the empirical aging models from the thesis are summarized in this section.

Part I - Capacity Fade:

Calendar Aging (Temperature):

$$25^{\circ}\text{C}: \quad \frac{Q_{\text{act}}}{Q_{\text{ini}}} = 1 - 0.002355 * \left(\frac{t}{d}\right)^{0.4393} \quad (44)$$

$$40^{\circ}\text{C}: \quad \frac{Q_{\text{act}}}{Q_{\text{ini}}} = 1 - 0.004552 * \left(\frac{t}{d}\right)^{0.4393} \quad (45)$$

$$55^{\circ}\text{C}: \quad \frac{Q_{\text{act}}}{Q_{\text{ini}}} = 1 - 0.008563 * \left(\frac{t}{d}\right)^{0.4393} \quad (46)$$

$$\frac{Q_{\text{act}}}{Q_{\text{ini}}} = 1 - 3149 * \exp\left(-\frac{34985 \text{ J/mol}}{RT}\right) \left(\frac{t}{d}\right)^{0.4393} \quad (49)$$

Cycle Life Aging (Temperature):

$$10^{\circ}\text{C}: \quad \frac{Q_{\text{act}}}{Q_{\text{ini}}} = 1 - 2.0 \times 10^{-5} * \left(\frac{Q_{\text{Ah}}}{\text{Ah}}\right)^{0.8441} \quad (58)$$

$$25^{\circ}\text{C}: \quad \frac{Q_{\text{act}}}{Q_{\text{ini}}} = 1 - 1.5 \times 10^{-5} * \left(\frac{Q_{\text{Ah}}}{\text{Ah}}\right)^{0.8441} \quad (59)$$

$$40^{\circ}\text{C}: \quad \frac{Q_{\text{act}}}{Q_{\text{ini}}} = 1 - 1.9 \times 10^{-5} * \left(\frac{Q_{\text{Ah}}}{\text{Ah}}\right)^{0.8441} \quad (60)$$

$$\frac{Q_{\text{act}}}{Q_{\text{ini}}} = 1 - 0.01 * \exp\left(\frac{8.53 \times 10^6 \text{ K}^2}{T^2} - \frac{5.708 \times 10^4 \text{ K}}{T} + 89\right) \left(\frac{Q_{\text{Ah}}}{\text{Ah}}\right)^{0.8441} \quad (61)$$

Cycle Life Aging (Discharge Rate):

$$1\text{C}: \quad \frac{Q_{\text{act}}}{Q_{\text{ini}}} = 1 - 1.5 \times 10^{-5} * \left(\frac{Q_{\text{Ah}}}{\text{Ah}}\right)^{0.8441} \quad (68)$$

$$3\text{C}: \quad \frac{Q_{\text{act}}}{Q_{\text{ini}}} = 1 - 1.8 \times 10^{-5} * \left(\frac{Q_{\text{Ah}}}{\text{Ah}}\right)^{0.8441} \quad (69)$$

$$5\text{C}: \quad \frac{Q_{\text{act}}}{Q_{\text{ini}}} = 1 - 2.2 \times 10^{-5} * \left(\frac{Q_{\text{Ah}}}{\text{Ah}}\right)^{0.8441} \quad (70)$$

$$\frac{Q_{\text{act}}}{Q_{\text{ini}}} = 1 - 0.0035 * \exp\left(\frac{-13840 \text{ J/mol} + 201 \text{ J} \cdot \text{h/mol} * |I_{\text{dis}}|}{RT}\right) \left(\frac{Q_{\text{Ah}}}{\text{Ah}}\right)^{0.8441} \quad (74)$$

Cycle Life Aging (Charge Rate):

$$\frac{C}{2}: \quad \frac{Q_{act}}{Q_{ini}} = 1 - 1.1 \times 10^{-5} * \left(\frac{Q_{Ah}}{Ah}\right)^{0.8441} \quad (83)$$

$$1C: \quad \frac{Q_{act}}{Q_{ini}} = 1 - 1.5 \times 10^{-5} * \left(\frac{Q_{Ah}}{Ah}\right)^{0.8441} \quad (84)$$

$$2C: \quad \frac{Q_{act}}{Q_{ini}} = 1 - 1.6 \times 10^{-5} * \left(\frac{Q_{Ah}}{Ah}\right)^{0.8441} \quad (85)$$

$$3C: \quad \frac{Q_{act}}{Q_{ini}} = 1 - 2.0 \times 10^{-5} * \left(\frac{Q_{Ah}}{Ah}\right)^{0.8441} \quad (86)$$

$$\frac{Q_{act}}{Q_{ini}} = 1 - 0.035 * \exp\left(\frac{-20080 \text{ J/mol} + 432 \text{ J} \cdot \text{h/mol} * |I_{ch}|}{RT}\right) \left(\frac{Q_{Ah}}{Ah}\right)^{0.8441} \quad (88)$$

Part II – Ohmic Resistance Increase:

Calendar Aging (Temperature):

$$25^{\circ}\text{C}: \quad \frac{R_{act}}{R_{ini}} = 1 + 0.0036 * \left(\frac{t}{d}\right)^{0.5139} \quad (50)$$

$$40^{\circ}\text{C}: \quad \frac{R_{act}}{R_{ini}} = 1 + 0.0170 * \left(\frac{t}{d}\right)^{0.5139} \quad (51)$$

$$55^{\circ}\text{C}: \quad \frac{R_{act}}{R_{ini}} = 1 + 0.0361 * \left(\frac{t}{d}\right)^{0.5139} \quad (52)$$

$$\frac{R_{act}}{R_{ini}} = 1 + 4.052 \times 10^8 * \exp\left(-\frac{62804 \text{ J/mol}}{RT}\right) \left(\frac{t}{d}\right)^{0.5139} \quad (55)$$

Cycle Life Aging (Temperature):

$$10^{\circ}\text{C}: \quad \frac{R_{act}}{R_{ini}} = 1 + 1.543 \times 10^{-5} * \left(\frac{Q_{Ah}}{Ah}\right)^{0.9271} \quad (63)$$

$$25^{\circ}\text{C}: \quad \frac{R_{act}}{R_{ini}} = 1 + 2.102 \times 10^{-5} * \left(\frac{Q_{Ah}}{Ah}\right)^{0.9271} \quad (64)$$

$$40^{\circ}\text{C}: \quad \frac{R_{act}}{R_{ini}} = 1 + 6.018 \times 10^{-5} * \left(\frac{Q_{Ah}}{Ah}\right)^{0.9271} \quad (65)$$

$$\frac{R_{act}}{R_{ini}} = 1 + 6.8 * \exp\left(-\frac{30911 \text{ J/mol}}{RT}\right) \left(\frac{Q_{Ah}}{Ah}\right)^{0.9271} \quad (66)$$

Cycle Life Aging (Discharge Rate):

$$1C: \quad \frac{R_{act}}{R_{ini}} = 1 + 2.103 \times 10^{-5} * \left(\frac{Q_{Ah}}{Ah}\right)^{0.9271} \quad (76)$$

$$3C: \quad \frac{R_{act}}{R_{ini}} = 1 + 6.148 \times 10^{-5} * \left(\frac{Q_{Ah}}{Ah}\right)^{0.9271} \quad (77)$$

$$5C: \quad \frac{R_{act}}{R_{ini}} = 1 + 9.334 \times 10^{-5} * \left(\frac{Q_{Ah}}{Ah}\right)^{0.9271} \quad (78)$$

$$\frac{R_{act}}{R_{ini}} = 1 + 7.6 * \exp\left(\frac{-31830 \text{ J/mol} + 669 \text{ J} \cdot \text{h/mol} * |I_{dis}|}{RT}\right) \left(\frac{Q_{Ah}}{Ah}\right)^{0.9271} \quad (81)$$

Cycle Life Aging (Charge Rate):

$$\frac{C}{2}: \quad \frac{R_{act}}{R_{ini}} = 1 + 2.668 \times 10^{-5} * \left(\frac{Q_{Ah}}{Ah}\right)^{0.9271} \quad (90)$$

$$1C: \quad \frac{R_{act}}{R_{ini}} = 1 + 2.122 \times 10^{-5} * \left(\frac{Q_{Ah}}{Ah}\right)^{0.9271} \quad (91)$$

$$2C: \quad \frac{R_{act}}{R_{ini}} = 1 + 2.534 \times 10^{-5} * \left(\frac{Q_{Ah}}{Ah}\right)^{0.9271} \quad (92)$$

$$3C: \quad \frac{R_{act}}{R_{ini}} = 1 + 3.891 \times 10^{-5} * \left(\frac{Q_{Ah}}{Ah}\right)^{0.9271} \quad (93)$$

$$\frac{R_{act}}{R_{ini}} = 1 + 6.6 * \exp\left(\frac{-31010 \text{ J/mol} + 140 \text{ J} \cdot \text{h/mol} * |I_{ch}|}{RT}\right) \left(\frac{Q_{Ah}}{Ah}\right)^{0.9271} \quad (94)$$

Bibliography

- [1] T.R. Hawkins, B. Singh, G. Majeau-Bettez, A.H. Strømman, Comparative environmental life cycle assessment of conventional and electric vehicles, *Journal of Industrial Ecology* 17 (2013) 53-64.
- [2] Solomon, S.; Qin, D.; Manning, M.; Marquis, M.; Averyt, K.; Tignor, M.M.; Miller, H.L.; Chen, Z. (eds.), *Climate Change 2007 – The Physical Science Basis*, Cambridge University Press, Cambridge (2007).
- [3] D.A. Notter, M. Gauch, R. Widmer, P. Wäger, A. Stamp, R. Zah, H.-J. Althaus, Contribution of Li-ion batteries to the environmental impact of electric vehicles, *Environmental Science & Technology* 44 (2010) 6550-6556.
- [4] L.A.-W. Ellingsen, G. Majeau-Bettez, B. Singh, A.K. Srivastava, L.O. Valøen, A.H. Strømman, Life cycle assessment of a lithium-ion battery vehicle pack, *Journal of Industrial Ecology* 18 (2014) 113-124.
- [5] Y. Wu, P. Keil, S.F. Schuster, A. Jossen, Impact of temperature and discharge rate on the aging of a LiCoO₂/LiNi_{0.8}Co_{0.15}Al_{0.05}O₂ lithium-ion pouch cell, *Journal of the Electrochemical Society* 164 (2017) A1438-A1445.
- [6] IEA - International Energy Agency, *Global EV Outlook 2017 – Two Million and Counting*, IEA (2017).
- [7] Office of Energy Efficiency & Renewable Energy, *The Most Common Warranty for Plug-In Vehicle Batteries is 8 Years/100,000 Miles*, URL: <https://energy.gov/eere/vehicles/fact-913-february-22-2016-most-common-warranty-plug-vehicle-batteries-8-years100000>.
- [8] D.H. Doughty, C.C. Crafts, *FreedomCAR: Electrical Energy Storage System Abuse Test Manual for Electric and Hybrid Electric Vehicle Applications* (2006).
- [9] Y. Wu, A. Jossen, Entropy-induced temperature variation as a new indicator for state of health estimation of lithium-ion cells, *Electrochimica Acta* 276 (2018) 370-376.
- [10] R. Marom, S.F. Amalraj, N. Leifer, D. Jacob, D. Aurbach, A review of advanced and practical lithium battery materials, *Journal of Materials Chemistry* 21 (2011) 9938-9938.
- [11] S. Goriparti, E. Miele, F. de Angelis, E. Di Fabrizio, R.P. Zaccaria, C. Capiglia, Review on recent progress of nanostructured anode materials for Li-ion batteries, *Journal of Power Sources* 257 (2014) 421-443.
- [12] S.S. Zhang, A review on the separators of liquid electrolyte Li-ion batteries, *Journal of Power Sources* 164 (2007) 351-364.
- [13] P. Roy, S.K. Srivastava, Nanostructured anode materials for lithium ion batteries, *Journal of Materials Chemistry A* 00 (2014) 1-27.

-
- [14] S.B. Chikkannanavar, D.M. Bernardi, L. Liu, A review of blended cathode materials for use in Li-ion batteries, *Journal of Power Sources* 248 (2014) 91-100.
- [15] N. Nitta, F. Wu, J.T. Lee, G. Yushin, Li-ion battery materials – Present and future, *Materials Today* 18 (2015) 252-264.
- [16] H. Jung, K.S. Kim, S.-E. Park, J. Park, The structural and electrochemical study on the blended anode with graphite and silicon carbon nano composite in Li ion battery, *Electrochimica Acta* 245 (2017) 791-795.
- [17] Y. Yamada, K. Usui, C.H. Chiang, K. Kikuchi, K. Furukawa, A. Yamada, General observation of lithium intercalation into graphite in ethylene-carbonate-free superconcentrated electrolytes, *ACS Applied Materials & Interfaces* 6 (2014) 10892-10899.
- [18] C.K. Chan, H. Peng, G. Liu, K. McIlwrath, X.F. Zhang, R.A. Huggins, Y. Cui, High-performance lithium battery anodes using silicon nanowires, *Nature Nanotechnology* 3 (2008) 31-35.
- [19] L.-H. Hu, F.-Y. Wu, C.-T. Lin, A.N. Khlobystov, L.-J. Li, Graphene-modified LiFePO₄ cathode for lithium ion battery beyond theoretical capacity, *Nature Communications* 4 (2013) 1687-1687.
- [20] J. Cho, Y.J. Kim, B. Park, Novel LiCoO₂ cathode material with Al₂O₃ coating for a Li ion cell, *Chemistry of Materials* 12 (2000) 3788-3791.
- [21] F. Lin, I.M. Markus, D. Nordlund, T.-C. Weng, M.D. Asta, H.L. Xin, M.M. Doeff, Surface reconstruction and chemical evolution of stoichiometric layered cathode materials for lithium-ion batteries, *Nature Communications* 5 (2014) 3529-3529.
- [22] S.K. Martha, O. Haik, E. Zinigrad, I. Exnar, T. Drezen, J.H. Miners, D. Aurbach, On the Thermal Stability of Olivine Cathode Materials for Lithium-Ion Batteries, *Journal of the Electrochemical Society* 158 (2011) A1115-A1122.
- [23] J. Tu, X.B. Zhao, G.S. Cao, D.G. Zhuang, T.J. Zhu, J.P. Tu, Enhanced cycling stability of LiMn₂O₄ by surface modification with melting impregnation method, *Electrochimica Acta* 51 (2006) 6456-6462.
- [24] A. Du Pasquier, I. Plitz, S. Menocal, G. Amatucci, A comparative study of Li-ion battery, supercapacitor and nonaqueous asymmetric hybrid devices for automotive applications, *Journal of Power Sources* 115 (2003) 171-178.
- [25] W.A. Appiah, J. Park, L. van Khue, Y. Lee, J. Choi, M.-H. Ryou, Y.M. Lee, Comparative study on experiments and simulation of blended cathode active materials for lithium ion batteries, *Electrochimica Acta* 187 (2016) 422-432.
- [26] P. Albertus, J. Christensen, J. Newman, Experiments on and modeling of positive electrodes with multiple active materials for lithium-ion batteries, *Journal of the Electrochemical Society* 156 (2009) A606-A618.
- [27] Z. Zhang, D. Fouchard, J.R. Rea, Differential scanning calorimetry material studies – implications for the safety of lithium-ion cells, *Journal of Power Sources* 70 (1998) 16-20.

- [28] A.J. Smith, S.R. Smith, T. Byrne, J.C. Burns, J.R. Dahn, Synergies in blended LiMn_2O_4 and $\text{Li}[\text{Ni}_{1/3}\text{Mn}_{1/3}\text{Co}_{1/3}]\text{O}_2$ positive electrodes, *Journal of the Electrochemical Society* 159 (2012) A1696-A1701.
- [29] S.-T. Myung, M.H. Cho, H.T. Hong, T.H. Kang, C.-S. Kim, Electrochemical evaluation of mixed oxide electrode for Li-ion secondary batteries: $\text{Li}_{1.1}\text{Mn}_{1.9}\text{O}_4$ and $\text{LiNi}_{0.8}\text{Co}_{0.15}\text{Al}_{0.05}\text{O}_2$, *Journal of Power Sources* 146 (2005) 222-225.
- [30] J. Jiang, J.R. Dahn, ARC studies of the thermal stability of three different cathode materials – LiCoO_2 ; $\text{Li}[\text{Ni}_{0.1}\text{Co}_{0.8}\text{Mn}_{0.1}]\text{O}_2$; and LiFePO_4 , in LiPF_6 and LiBoB EC/DEC electrolytes, *Electrochemistry Communications* 6 (2004) 39-43.
- [31] J.F. Whitacre, K. Zaghib, W.C. West, B.V. Ratnakumar, Dual active material composite cathode structures for Li-ion batteries, *Journal of Power Sources* 177 (2008) 528-536.
- [32] K.G. Gallagher, S.-H. Kang, S.U. Park, S.Y. Han, $x\text{Li}_2\text{MnO}_3 \cdot (1-x)\text{LiMO}_2$ blended with LiFePO_4 to achieve high energy density and pulse power capability, *Journal of Power Sources* 196 (2011) 9702-9707.
- [33] K.-S. Lee, S.-T. Myung, D.-W. Kim, Y.-K. Sun, AlF_3 -coated LiCoO_2 and $\text{Li}[\text{Ni}_{1/3}\text{Co}_{1/3}\text{Mn}_{1/3}]\text{O}_2$ blend composite cathode for lithium ion batteries, *Journal of Power Sources* 196 (2011) 6974-6977.
- [34] C.S. Johnson, N. Li, C. Lefief, J.T. Vaughey, M.M. Thackeray, Synthesis, Characterization and Electrochemistry of Lithium Battery Electrodes – $x\text{Li}_2\text{MnO}_3 \cdot (1-x)\text{LiMn}_{0.333}\text{Ni}_{0.333}\text{Co}_{0.333}\text{O}_2$ ($0 \leq x \leq 0.7$), *Chemistry of Materials* 20 (2008) 6095-6106.
- [35] M.M. Thackeray, S.-H. Kang, C.S. Johnson, J.T. Vaughey, R. Benedek, S.A. Hackney, Li_2MnO_3 -stabilized LiMO_2 ($\text{M} = \text{Mn}, \text{Ni}, \text{Co}$) electrodes for lithium-ion batteries, *Journal of Materials Chemistry* 17 (2007) 3112-3112.
- [36] J.P. Schmidt, H.Y. Tran, J. Richter, E. Ivers-Tiffée, M. Wohlfahrt-Mehrens, Analysis and prediction of the open circuit potential of lithium-ion cells, *Journal of Power Sources* 239 (2013) 696-704.
- [37] A. Barré, B. Deguilhem, S. Grolleau, M. Gérard, F. Suard, D. Riu, A review on lithium-ion battery ageing mechanisms and estimations for automotive applications, *Journal of Power Sources* 241 (2013) 680-689.
- [38] D.P. Abraham, E.M. Reynolds, E. Sammann, A.N. Jansen, D.W. Dees, Aging characteristics of high-power lithium-ion cells with $\text{LiNi}_{0.8}\text{Co}_{0.15}\text{Al}_{0.05}\text{O}_2$ and $\text{Li}_{4/3}\text{Ti}_5/3\text{O}_4$ electrodes, *Electrochimica Acta* 51 (2005) 502-510.
- [39] J. Vetter, P. Novák, M.R. Wagner, C. Veit, K.-C. Möller, J.O. Besenhard, M. Winter, M. Wohlfahrt-Mehrens, C. Vogler, A. Hammouche, Ageing mechanisms in lithium-ion batteries, *Journal of Power Sources* 147 (2005) 269-281.
- [40] M. Nie, D. Chalasani, D.P. Abraham, Y. Chen, A. Bose, B.L. Lucht, Lithium ion battery graphite solid electrolyte interphase revealed by microscopy and spectroscopy, *Journal of Physical Chemistry C* 117 (2013) 1257-1267.

- [41] K. Xu, A. von Cresce, Interfacing electrolytes with electrodes in Li ion batteries, *Journal of Materials Chemistry* 21 (2011) 9849-9849.
- [42] P. Verma, P. Maire, P. Novák, A review of the features and analyses of the solid electrolyte interphase in Li-ion batteries, *Electrochimica Acta* 55 (2010) 6332-6341.
- [43] F.M. Wang, M.H. Yu, Hsiao Y.J., Tsai Y., Hwang B.J., Wang Y.Y., Wan C.C., Aging effects to solid electrolyte interface (SEI) membrane formation and the performance analysis of lithium ion batteries, *International Journal of Electrochemical Science* 6 (2011) 1014-1026.
- [44] X.-G. Yang, Y. Leng, G. Zhang, S. Ge, C.-Y. Wang, Modeling of lithium plating induced aging of lithium-ion batteries – Transition from linear to nonlinear aging, *Journal of Power Sources* 360 (2017) 28-40.
- [45] R. Yazami, Y. Reynier, Mechanism of self-discharge in graphite–lithium anode, *Electrochimica Acta* 47 (2002) 1217-1223.
- [46] P. Ramadass, B. Haran, R. White, B.N. Popov, Capacity fade of Sony 18650 cells cycled at elevated temperatures – Part I. Cycling performance, *Journal of Power Sources* 112 (2002) 606-613.
- [47] P. Ramadass, B. Haran, R. White, B.N. Popov, Capacity fade of Sony 18650 cells cycled at elevated temperatures – Part II. Capacity fade analysis, *Journal of Power Sources* 112 (2002) 614-620.
- [48] G. Amatucci, A. Du Pasquier, A. Blyr, T. Zheng, J.M. Tarascon, The elevated temperature performance of the $\text{LiMn}_2\text{O}_4/\text{C}$ system: failure and solutions, *Electrochimica Acta* 45 (1999) 255-271.
- [49] A.M. Andersson, K. Edström, J.O. Thomas, Characterisation of the ambient and elevated temperature performance of a graphite electrode, *Journal of Power Sources* 81-82 (1999) 8-12.
- [50] F. Joho, B. Rykart, R. Imhof, P. Novák, M.E. Spahr, A. Monnier, Key factors for the cycling stability of graphite intercalation electrodes for lithium-ion batteries, *Journal of Power Sources* 81-82 (1999) 243-247.
- [51] G.E. Blomgren, Electrolytes for advanced batteries, *Journal of Power Sources* 81-82 (1999) 112-118.
- [52] S. Schindler, M. Bauer, M. Petzl, M.A. Danzer, Voltage relaxation and impedance spectroscopy as in-operando methods for the detection of lithium plating on graphitic anodes in commercial lithium-ion cells, *Journal of Power Sources* 304 (2016) 170-180.
- [53] D. Anseán, M. Dubarry, A. Devie, B.Y. Liaw, V.M. García, J.C. Viera, M. González, Operando lithium plating quantification and early detection of a commercial LiFePO_4 cell cycled under dynamic driving schedule, *Journal of Power Sources* 356 (2017) 36-46.
- [54] S.S. Zhang, K. Xu, T.R. Jow, Study of the charging process of a LiCoO_2 -based Li-ion battery, *Journal of Power Sources* 160 (2006) 1349-1354.
- [55] C. Uhlmann, J. Illig, M. Ender, R. Schuster, E. Ivers-Tiffée, In situ detection of lithium metal plating on graphite in experimental cells, *Journal of Power Sources* 279 (2015) 428-438.

- [56] D. Burow, K. Sergeeva, S. Calles, K. Schorb, A. Börger, C. Roth, P. Heitjans, Inhomogeneous degradation of graphite anodes in automotive lithium ion batteries under low-temperature pulse cycling conditions, *Journal of Power Sources* 307 (2016) 806-814.
- [57] M. Petzl, M.A. Danzer, Nondestructive detection, characterization, and quantification of lithium plating in commercial lithium-ion batteries, *Journal of Power Sources* 254 (2014) 80-87.
- [58] D. Aurbach, B. Markovsky, G. Salitra, E. Markevich, Y. Talyossef, M. Koltypin, L. Nazar, B. Ellis, D. Kovacheva, Review on electrode–electrolyte solution interactions, related to cathode materials for Li-ion batteries, *Journal of Power Sources* 165 (2007) 491-499.
- [59] N. Legrand, B. Knosp, P. Desprez, F. Lapique, S. Raël, Physical characterization of the charging process of a Li-ion battery and prediction of Li plating by electrochemical modelling, *Journal of Power Sources* 245 (2014) 208-216.
- [60] H. Honbo, K. Takei, Y. Ishii, T. Nishida, Electrochemical properties and Li deposition morphologies of surface modified graphite after grinding, *Journal of Power Sources* 189 (2009) 337-343.
- [61] M. Dollé, L. Sannier, B. Beaudoin, M. Trentin, J.-M. Tarascon, Live scanning electron microscope observations of dendritic growth in lithium/polymer cells, *Electrochemical and Solid-State Letters* 5 (2002) A286-A289.
- [62] S.F. Schuster, T. Bach, E. Fleder, J. Müller, M. Brand, G. Sextl, A. Jossen, Nonlinear aging characteristics of lithium-ion cells under different operational conditions, *Journal of Energy Storage* 1 (2015) 44-53.
- [63] C. Julien, A. Mauger, K. Zaghib, H. Groult, Comparative issues of cathode materials for Li-ion batteries, *Inorganics* 2 (2014) 132-154.
- [64] de Dompablo, M. E. A., C. Marianetti, A. van der Ven, G. Ceder, Jahn-Teller mediated ordering in layered Li_xMO_2 compounds, *Physical Review B* 63 (2001) 311-311.
- [65] M. Wohlfahrt-Mehrens, C. Vogler, J. Garche, Aging mechanisms of lithium cathode materials, *Journal of Power Sources* 127 (2004) 58-64.
- [66] G.G. Amatucci, Tarascon J.M., Klein L.C., Cobalt dissolution in LiCoO_2 -based non-aqueous rechargeable batteries, *Solid State Ionics* 83 (1996) 167-173.
- [67] J. Wang, Y. Tang, J. Yang, R. Li, G. Liang, X. Sun, Nature of LiFePO_4 aging process – Roles of impurity phases, *Journal of Power Sources* 238 (2013) 454-463.
- [68] K. Amine, J. Liu, I. Belharouak, High-temperature storage and cycling of C- LiFePO_4 /graphite Li-ion cells, *Electrochemistry Communications* 7 (2005) 669-673.
- [69] H. Zheng, Q. Sun, G. Liu, X. Song, V.S. Battaglia, Correlation between dissolution behavior and electrochemical cycling performance for $\text{LiNi}_{1/3}\text{Co}_{1/3}\text{Mn}_{1/3}\text{O}_2$ -based cells, *Journal of Power Sources* 207 (2012) 134-140.
- [70] D.P. Abraham, T. Spila, M.M. Furczon, E. Sammann, Evidence of transition-metal accumulation on aged graphite anodes by SIMS, *Electrochemical and Solid-State Letters* 11 (2008) A226-A228.

- [71] S.K. Martha, H. Sclar, Z. Szmuk Framowitz, D. Kovacheva, N. Saliyski, Y. Gofer, P. Sharon, E. Golik, B. Markovsky, D. Aurbach, A comparative study of electrodes comprising nanometric and submicron particles of $\text{LiNi}_{0.50}\text{Mn}_{0.50}\text{O}_2$, $\text{LiNi}_{0.33}\text{Mn}_{0.33}\text{Co}_{0.33}\text{O}_2$, and $\text{LiNi}_{0.40}\text{Mn}_{0.40}\text{Co}_{0.20}\text{O}_2$ layered compounds, *Journal of Power Sources* 189 (2009) 248-255.
- [72] M. Börner, S. Klamor, B. Hoffmann, M. Schroeder, S. Nowak, A. Würsig, M. Winter, F.M. Schappacher, Investigations on the C-rate and temperature dependence of manganese dissolution/deposition in $\text{LiMn}_2\text{O}_4/\text{Li}_4\text{Ti}_5\text{O}_{12}$ lithium ion batteries, *Journal of the Electrochemical Society* 163 (2016) A831-A837.
- [73] Z. Ma, J. Jiang, W. Shi, W. Zhang, C.C. Mi, Investigation of path dependence in commercial lithium-ion cells for pure electric bus applications – Aging mechanism identification, *Journal of Power Sources* 274 (2015) 29-40.
- [74] H. Takahara, Y. Kobayashi, K. Shono, H. Kobayashi, M. Shikano, T. Nakamura, Analysis of solid electrolyte interphase in Mn-based cathode/graphite Li-ion battery with glow discharge optical emission spectroscopy, *Journal of the Electrochemical Society* 161 (2014) A1716-A1722.
- [75] K. Amine, C.H. Chen, J. Liu, M. Hammond, A. Jansen, D. Dees, I. Bloom, D. Vissers, G. Henriksen, Factors responsible for impedance rise in high power lithium ion batteries, *Journal of Power Sources* 97-98 (2001) 684-687.
- [76] S. Krueger, R. Kloepsch, J. Li, S. Nowak, S. Passerini, M. Winter, How do reactions at the anode/electrolyte interface determine the cathode performance in lithium-ion batteries?, *Journal of the Electrochemical Society* 160 (2013) A542-A548.
- [77] M.K. Rahman, Y. Saito, Investigation of positive electrodes after cycle testing of high-power Li-ion battery cells, *Journal of Power Sources* 174 (2007) 889-894.
- [78] M. Shikano, H. Kobayashi, S. Koike, H. Sakaebe, E. Ikenaga, K. Kobayashi, K. Tatsumi, Investigation of positive electrodes after cycle testing of high-power Li-ion battery cells II, *Journal of Power Sources* 174 (2007) 795-799.
- [79] S.J. An, J. Li, C. Daniel, D. Mohanty, S. Nagpure, D.L. Wood, The state of understanding of the lithium-ion-battery graphite solid electrolyte interphase (SEI) and its relationship to formation cycling, *Carbon* 105 (2016) 52-76.
- [80] D. Aurbach, H. Gottlieb, The electrochemical behavior of selected polar aprotic systems, *Electrochimica Acta* 34 (1989) 141-156.
- [81] V. Etacheri, R. Marom, R. Elazari, G. Salitra, D. Aurbach, Challenges in the development of advanced Li-ion batteries – A review, *Energy & Environmental Science* 4 (2011) 3243-3243.
- [82] A. Würsig, H. Buqa, M. Holzapfel, F. Krumeich, P. Novák, Film formation at positive electrodes in Lithium-ion batteries, *Electrochemical and Solid-State Letters* 8 (2005) A34-A37.
- [83] R. Hausbrand, G. Cherkashinin, H. Ehrenberg, M. Gröting, K. Albe, C. Hess, W. Jaegermann, Fundamental degradation mechanisms of layered oxide Li-ion battery cathode materials –

- Methodology, insights and novel approaches, *Materials Science and Engineering: B* 192 (2015) 3-25.
- [84] J. Song, Two- and three-electrode impedance spectroscopy of lithium-ion batteries, *Journal of Power Sources* 111 (2002) 255-267.
- [85] C. Peabody, C.B. Arnold, The role of mechanically induced separator creep in lithium-ion battery capacity fade, *Journal of Power Sources* 196 (2011) 8147-8153.
- [86] L. Norin, R. Kostecki, F. McLarnon, Study of membrane degradation in high-power lithium-ion cells, *Electrochemical and Solid-State Letters* 5 (2002) A67-A69.
- [87] R. Kostecki, L. Norin, X. Song, F. McLarnon, Diagnostic studies of polyolefin separators in high-power Li-ion cells, *Journal of the Electrochemical Society* 151 (2004) A522-A526.
- [88] B. Michalak, H. Sommer, D. Mannes, A. Kaestner, T. Brezesinski, J. Janek, Gas evolution in operating lithium-ion batteries studied in situ by neutron imaging, *Scientific Reports* 5 (2015) 15627-15627.
- [89] F. Leng, C.M. Tan, M. Pecht, Effect of temperature on the aging rate of Li ion battery operating above room temperature, *Scientific Reports* 5 (2015) 12967-12967.
- [90] T. Ma, G.-L. Xu, Y. Li, L. Wang, X. He, J. Zheng, J. Liu, M.H. Engelhard, P. Zapol, L.A. Curtiss, J. Jorne, K. Amine, Z. Chen, Revisiting the corrosion of the aluminum current collector in lithium-ion batteries, *Journal of Physical Chemistry Letters* 8 (2017) 1072-1077.
- [91] G. Mulder, K. Trad, S. Ried, D. Sotta, MAT4BAT-Advanced materials for batteries – Deliverable 5.1-List of relevant regulations and standards (2016).
- [92] G. Mulder, N. Omar, S. Pauwels, F. Leemans, B. Verbrugge, W. de Nijs, P. van den Bossche, D. Six, J. van Mierlo, Enhanced test methods to characterise automotive battery cells, *Journal of Power Sources* 196 (2011) 10079-10087.
- [93] Idaho National Laboratory, Battery Test Manual For Plug-In Hybrid Electric Vehicles, 1st edition, Idaho Falls, Idaho (2010).
- [94] International Organization for Standardization, Electrically propelled road vehicles — Test specification for lithium-ion traction battery systems – Part 1: High power applications (2009).
- [95] International Organization for Standardization, Electrically propelled road vehicles — Test specification for lithium-ion traction battery packs and systems – Part 2: High energy application (2009).
- [96] E.V. Thomas, I. Bloom, J.P. Christophersen, V.S. Battaglia, Statistical methodology for predicting the life of lithium-ion cells via accelerated degradation testing, *Journal of Power Sources* 184 (2008) 312-317.
- [97] Y. Cui, C. Du, G. Yin, Y. Gao, L. Zhang, T. Guan, L. Yang, F. Wang, Multi-stress factor model for cycle lifetime prediction of lithium ion batteries with shallow-depth discharge, *Journal of Power Sources* 279 (2015) 123-132.

- [98] J. Schmalstieg, S. Käbitz, M. Ecker, D.U. Sauer, A holistic aging model for Li(NiMnCo)O₂ based 18650 lithium-ion batteries, *Journal of Power Sources* 257 (2014) 325-334.
- [99] L. Su, J. Zhang, C. Wang, Y. Zhang, Z. Li, Y. Song, T. Jin, Z. Ma, Identifying main factors of capacity fading in lithium ion cells using orthogonal design of experiments, *Applied Energy* 163 (2016) 201-210.
- [100] Scrosati, B.; Garche, J.; Tillmetz, W. (eds.), *Advances in battery technologies for electric vehicles*, Elsevier (2015).
- [101] E. Sarasketa-Zabala, I. Laresgoiti, I. Alava, M. Rivas, I. Villarreal, F. Blanco, Validation of the methodology for lithium-ion batteries lifetime prognosis, *EVS 27*, Barcelona, Spain (2013).
- [102] F. Herb, *Alterungsmechanismen in Lithium-Ionen-Batterien und PEM-Brennstoffzellen und deren Einfluss auf die Eigenschaften von daraus bestehenden Hybrid-Systemen*, doctorate thesis, Universität Ulm, Ulm (2010).
- [103] M. Ecker, J.B. Gerschler, J. Vogel, S. Käbitz, F. Hust, P. Dechent, D.U. Sauer, Development of a lifetime prediction model for lithium-ion batteries based on extended accelerated aging test data, *Journal of Power Sources* 215 (2012) 248-257.
- [104] J. Wang, P. Liu, J. Hicks-Garner, E. Sherman, S. Soukiazian, M. Verbrugge, H. Tataria, J. Musser, P. Finamore, Cycle-life model for graphite-LiFePO₄ cells, *Journal of Power Sources* 196 (2011) 3942-3948.
- [105] G. Suri, S. Onori, A control-oriented cycle-life model for hybrid electric vehicle lithium-ion batteries, *Energy* 96 (2016) 644-653.
- [106] I. Laresgoiti, S. Käbitz, M. Ecker, D.U. Sauer, Modeling mechanical degradation in lithium ion batteries during cycling – Solid electrolyte interphase fracture, *Journal of Power Sources* 300 (2015) 112-122.
- [107] Q. Badey, G. Cherouvrier, Y. Reynier, J.M. Duffault, S. Franger, Ageing forecast of lithium-ion batteries for electric and hybrid vehicles, *Current Topics in Electrochemistry* 16 (2011) 65-79.
- [108] M. Petit, E. Prada, V. Sauvant-Moynot, Development of an empirical aging model for Li-ion batteries and application to assess the impact of Vehicle-to-Grid strategies on battery lifetime, *Applied Energy* 172 (2016) 398-407.
- [109] I. Bloom, B. Cole, J. Sohn, S. Jones, E. Polzin, V. Battaglia, G. Henriksen, C. Motloch, R. Richardson, T. Unkelhaeuser, D. Ingersoll, H. Case, An accelerated calendar and cycle life study of Li-ion cells, *Journal of Power Sources* 101 (2001) 238-247.
- [110] C. Guenther, B. Schott, W. Hennings, P. Waldowski, M.A. Danzer, Model-based investigation of electric vehicle battery aging by means of vehicle-to-grid scenario simulations, *Journal of Power Sources* 239 (2013) 604-610.
- [111] T. Waldmann, A. Iturrondobeitia, M. Kasper, N. Ghanbari, F. Aguesse, E. Bekaert, L. Daniel, S. Genies, I.J. Gordon, M.W. Löble, E. de Vito, M. Wohlfahrt-Mehrens, Review—Post-mortem analysis of aged lithium-ion batteries: Disassembly methodology and physico-chemical analysis techniques, *Journal of the Electrochemical Society* 163 (2016) A2149-A2164.

- [112] A. Farmann, W. Waag, A. Marongiu, D.U. Sauer, Critical review of on-board capacity estimation techniques for lithium-ion batteries in electric and hybrid electric vehicles, *Journal of Power Sources* 281 (2015) 114-130.
- [113] N. Latner, State of charge measurement of nickel-cadmium batteries, *Review of Scientific Instruments* 40 (1969) 364-365.
- [114] M. Dubarry, V. Svoboda, R. Hwu, B.Y. Liaw, Capacity loss in rechargeable lithium cells during cycle life testing – The importance of determining state-of-charge, *Journal of Power Sources* 174 (2007) 1121-1125.
- [115] M. Dubarry, V. Svoboda, R. Hwu, B. Yann Liaw, Incremental capacity analysis and close-to-equilibrium OCV measurements to quantify capacity fade in commercial rechargeable lithium batteries, *Electrochemical and Solid-State Letters* 9 (2006) A454-A457.
- [116] Z. Li, J. Huang, B.Y. Liaw, J. Zhang, On state-of-charge determination for lithium-ion batteries, *Journal of Power Sources* 348 (2017) 281-301.
- [117] USABC and DOE National Laboratories, *Electric Vehicle Battery Test Procedures Manual*, 2nd edition (1996).
- [118] M. Berecibar, I. Gandiaga, I. Villarreal, N. Omar, J. van Mierlo, P. van den Bossche, Critical review of state of health estimation methods of Li-ion batteries for real applications, *Renewable and Sustainable Energy Reviews* 56 (2016) 572-587.
- [119] M.U. Cuma, T. Koroglu, A comprehensive review on estimation strategies used in hybrid and battery electric vehicles, *Renewable and Sustainable Energy Reviews* 42 (2015) 517-531.
- [120] O. Erdinc, B. Vural, M. Uzunoglu, A dynamic lithium-ion battery model considering the effects of temperature and capacity fading, *IEEE Conference* (2009).
- [121] A. Nuhic, T. Terzimehic, T. Soczka-Guth, M. Buchholz, K. Dietmayer, Health diagnosis and remaining useful life prognostics of lithium-ion batteries using data-driven methods, *Journal of Power Sources* 239 (2013) 680-688.
- [122] S.F. Schuster, M.J. Brand, C. Campestrini, M. Gleissenberger, A. Jossen, Correlation between capacity and impedance of lithium-ion cells during calendar and cycle life, *Journal of Power Sources* 305 (2016) 191-199.
- [123] E. Cabrera-Castillo, F. Niedermeier, A. Jossen, Calculation of the state of safety (SOS) for lithium ion batteries, *Journal of Power Sources* 324 (2016) 509-520.
- [124] C.R. Birkel, E. McTurk, M.R. Roberts, P.G. Bruce, D.A. Howey, A parametric open circuit voltage model for lithium ion batteries, *Journal of the Electrochemical Society* 162 (2015) A2271-A2280.
- [125] K. Jalkanen, T. Aho, K. Vuorilehto, Entropy change effects on the thermal behavior of a LiFePO₄/graphite lithium-ion cell at different states of charge, *Journal of Power Sources* 243 (2013) 354-360.

- [126] A. Yamada, H. Koizumi, S.-I. Nishimura, N. Sonoyama, R. Kanno, M. Yonemura, T. Nakamura, Y. Kobayashi, Room-temperature miscibility gap in Li_xFePO_4 , *Nature Materials* 5 (2006) 357-360.
- [127] V. Srinivasan, J. Newman, Discharge Model for the Lithium Iron-Phosphate Electrode, *Journal of the Electrochemical Society* 151 (2004) A1517-A1529.
- [128] J.R. Dahn, Phase diagram of Li_xC_6 , *Physical Review B* 44 (1991) 9170-9177.
- [129] M. Ouyang, Z. Chu, L. Lu, J. Li, X. Han, X. Feng, G. Liu, Low temperature aging mechanism identification and lithium deposition in a large format lithium iron phosphate battery for different charge profiles, *Journal of Power Sources* 286 (2015) 309-320.
- [130] X. Feng, J. Li, M. Ouyang, L. Lu, J. Li, X. He, Using probability density function to evaluate the state of health of lithium-ion batteries, *Journal of Power Sources* 232 (2013) 209-218.
- [131] M. Safari, C. Delacourt, Aging of a commercial graphite/ LiFePO_4 cell, *Journal of the Electrochemical Society* 158 (2011) A1123-A1135.
- [132] M. Dubarry, C. Truchot, B.Y. Liaw, K. Gering, S. Sazhin, D. Jamison, C. Michelbacher, Evaluation of commercial lithium-ion cells based on composite positive electrode for plug-in hybrid electric vehicle applications – Part II. Degradation mechanism under 2C cycle aging, *Journal of Power Sources* 196 (2011) 10336-10343.
- [133] M. Dubarry, B.Y. Liaw, Identify capacity fading mechanism in a commercial LiFePO_4 cell, *Journal of Power Sources* 194 (2009) 541-549.
- [134] M. Kerlau, M. Marcinek, V. Srinivasan, R.M. Kostecki, Studies of local degradation phenomena in composite cathodes for lithium-ion batteries, *Electrochimica Acta* 52 (2007) 5422-5429.
- [135] N. Sharma, V.K. Peterson, M.M. Elcombe, M. Avdeev, A.J. Studer, N. Blagojevic, R. Yusoff, N. Kamarulzaman, Structural changes in a commercial lithium-ion battery during electrochemical cycling – An in situ neutron diffraction study, *Journal of Power Sources* 195 (2010) 8258-8266.
- [136] J. Christensen, J. Newman, Effect of anode film resistance on the charge/discharge capacity of a lithium-ion battery, *Journal of the Electrochemical Society* 150 (2003) A1416-A1420.
- [137] M. Dubarry, C. Truchot, B.Y. Liaw, Synthesize battery degradation modes via a diagnostic and prognostic model, *Journal of Power Sources* 219 (2012) 204-216.
- [138] I. Bloom, L.K. Walker, J.K. Basco, D.P. Abraham, J.P. Christophersen, C.D. Ho, Differential voltage analyses of high-power lithium-ion cells. 4. Cells containing NMC, *Journal of Power Sources* 195 (2010) 877-882.
- [139] I. Bloom, A.N. Jansen, D.P. Abraham, J. Knuth, S.A. Jones, V.S. Battaglia, G.L. Henriksen, Differential voltage analyses of high-power, lithium-ion cells, *Journal of Power Sources* 139 (2005) 295-303.
- [140] I. Bloom, J.P. Christophersen, D.P. Abraham, K.L. Gering, Differential voltage analyses of high-power lithium-ion cells, *Journal of Power Sources* 157 (2006) 537-542.

- [141] I. Bloom, J. Christophersen, K. Gering, Differential voltage analyses of high-power lithium-ion cells, *Journal of Power Sources* 139 (2005) 304-313.
- [142] H.M. Dahn, A.J. Smith, J.C. Burns, D.A. Stevens, J.R. Dahn, User-friendly differential voltage analysis freeware for the analysis of degradation mechanisms in Li-ion batteries, *Journal of the Electrochemical Society* 159 (2012) A1405-A1409.
- [143] P. Keil, A. Jossen, Calendar aging of NCA Lithium-ion batteries investigated by differential voltage analysis and coulomb tracking, *Journal of the Electrochemical Society* 164 (2016) A6066-A6074.
- [144] C. Clauss, H. Schweigart, The reduction of manganese dioxide in Leclanché-type dry cells as displayed by derivative discharge functions, *Journal of the Electrochemical Society* 123 (1976) 951-959.
- [145] T. Kobayashi, N. Kawasaki, Y. Kobayashi, K. Shono, Y. Mita, H. Miyashiro, A method of separating the capacities of layer and spinel compounds in blended cathode, *Journal of Power Sources* 245 (2014) 1-6.
- [146] D. Andre, M. Meiler, K. Steiner, C. Wimmer, T. Soczka-Guth, D.U. Sauer, Characterization of high-power lithium-ion batteries by electrochemical impedance spectroscopy. I. Experimental investigation, *Journal of Power Sources* 196 (2011) 5334-5341.
- [147] A. Jossen, Fundamentals of battery dynamics, *Journal of Power Sources* 154 (2006) 530-538.
- [148] Belharouak, I. (ed.), *Lithium Ion Batteries - New Developments*, InTech (2012).
- [149] J.S. Gnanaraj, R.W. Thompson, S.N. Iaconatti, J.F. DiCarlo, K.M. Abraham, Formation and growth of surface films on graphitic anode materials for Li-ion batteries, *Electrochemical Solid-State Letters* 8 (2005) A128-A132.
- [150] H. Brandstätter, I. Hanzu, M. Wilkening, Myth and reality about the origin of inductive loops in impedance spectra of lithium-ion electrodes — A critical experimental approach, *Electrochimica Acta* 207 (2016) 218-223.
- [151] T. Osaka, T. Momma, D. Mukoyama, H. Nara, Proposal of novel equivalent circuit for electrochemical impedance analysis of commercially available lithium ion battery, *Journal of Power Sources* 205 (2012) 483-486.
- [152] W. Waag, S. Käbitz, D.U. Sauer, Experimental investigation of the lithium-ion battery impedance characteristic at various conditions and aging states and its influence on the application, *Applied Energy* 102 (2013) 885-897.
- [153] A. Barai, G.H. Chouchelamane, Y. Guo, A. McGordon, P. Jennings, A study on the impact of lithium-ion cell relaxation on electrochemical impedance spectroscopy, *Journal of Power Sources* 280 (2015) 74-80.
- [154] H.-M. Cho, W.-S. Choi, J.-Y. Go, S.-E. Bae, H.-C. Shin, A study on time-dependent low temperature power performance of a lithium-ion battery, *Journal of Power Sources* 198 (2012) 273-280.

- [155] Q.-C. Zhuang, T. Wei, L.-L. Du, Y.-L. Cui, L. Fang, S.-G. Sun, An electrochemical impedance spectroscopic study of the electronic and ionic transport properties of spinel LiMn_2O_4 , *Journal of Physical Chemistry C* 114 (2010) 8614-8621.
- [156] K. Takeno, Quick testing of batteries in lithium-ion battery packs with impedance-measuring technology, *Journal of Power Sources* 128 (2004) 67-75.
- [157] C.T. Love, M.B. Virji, R.E. Rocheleau, K.E. Swider-Lyons, State-of-health monitoring of 18650 4S packs with a single-point impedance diagnostic, *Journal of Power Sources* 266 (2014) 512-519.
- [158] L. Liao, P. Zuo, Y. Ma, X. Chen, Y. An, Y. Gao, G. Yin, Effects of temperature on charge/discharge behaviors of LiFePO_4 cathode for Li-ion batteries, *Electrochimica Acta* 60 (2012) 269-273.
- [159] J. Gomez, R. Nelson, E.E. Kalu, M.H. Weatherspoon, J.P. Zheng, Equivalent circuit model parameters of a high-power Li-ion battery – Thermal and state of charge effects, *Journal of Power Sources* 196 (2011) 4826-4831.
- [160] A. Mertens, I.C. Vinke, H. Tempel, H. Kungl, L. de Haart, R.A. Eichel, J. Granwehr, Quantitative analysis of time-domain supported electrochemical impedance spectroscopy data of Li-ion batteries – Reliable activation energy determination at low frequencies, *Journal of the Electrochemical Society* 163 (2016) H521-H527.
- [161] J. Illig, J.P. Schmidt, M. Weiss, A. Weber, E. Ivers-Tiffée, Understanding the impedance spectrum of 18650 LiFePO_4 -cells, *Journal of Power Sources* 239 (2013) 670-679.
- [162] J. Illig, M. Ender, A. Weber, E. Ivers-Tiffée, Modeling graphite anodes with serial and transmission line models, *Journal of Power Sources* 282 (2015) 335-347.
- [163] K. Maher, R. Yazami, Effect of overcharge on entropy and enthalpy of lithium-ion batteries, *Electrochimica Acta* 101 (2013) 71-78.
- [164] K. Maher, R. Yazami, A study of lithium ion batteries cycle aging by thermodynamics techniques, *Journal of Power Sources* 247 (2014) 527-533.
- [165] K. Maher, R. Yazami, A thermodynamic and crystal structure study of thermally aged lithium ion cells, *Journal of Power Sources* 261 (2014) 389-400.
- [166] M. Fleischhammer, T. Waldmann, G. Bisle, B.-I. Hogg, M. Wohlfahrt-Mehrens, Interaction of cyclic ageing at high-rate and low temperatures and safety in lithium-ion batteries, *Journal of Power Sources* 274 (2015) 432-439.
- [167] P. Röder, B. Stiaszny, J.C. Ziegler, N. Baba, P. Lagaly, H.-D. Wiemhöfer, The impact of calendar aging on the thermal stability of a $\text{LiMn}_2\text{O}_4\text{--Li}(\text{Ni}_{1/3}\text{Mn}_{1/3}\text{Co}_{1/3})\text{O}_2/\text{graphite}$ lithium-ion cell, *Journal of Power Sources* 268 (2014) 315-325.
- [168] Y. Saito, M. Shikano, H. Kobayashi, Heat generation behavior during charging and discharging of lithium-ion batteries after long-time storage, *Journal of Power Sources* 244 (2013) 294-299.

- [169] Y. Merla, B. Wu, V. Yufit, N.P. Brandon, R.F. Martinez-Botas, G.J. Offer, Extending battery life – A low-cost practical diagnostic technique for lithium-ion batteries, *Journal of Power Sources* 331 (2016) 224-231.
- [170] Y. Merla, B. Wu, V. Yufit, N.P. Brandon, R.F. Martinez-Botas, G.J. Offer, Novel application of differential thermal voltammetry as an in-depth state-of-health diagnosis method for lithium-ion batteries, *Journal of Power Sources* 307 (2016) 308-319.
- [171] B. Wu, V. Yufit, Y. Merla, R.F. Martinez-Botas, N.P. Brandon, G.J. Offer, Differential thermal voltammetry for tracking of degradation in lithium-ion batteries, *Journal of Power Sources* 273 (2015) 495-501.
- [172] E.P.M. Leiva, E. Perassi, D. Barraco, Shedding light on the entropy change found for the transition stage II→stage I of Li-ion storage in graphite, *Journal of the Electrochemical Society* 164 (2016) A6154-A6157.
- [173] Scholz, F. (ed.), *Electroanalytical Methods – Guide to experiments and applications*, Springer (2010) 30-31.
- [174] W. Zhang, L. Jiang, P. van Durmen, S. Saadat, R. Yazami, A combined thermodynamics & computational method to assess lithium composition in anode and cathode of lithium ion batteries, *Electrochimica Acta* 214 (2016) 56-67.
- [175] Y. Reynier, R. Yazami, B. Fultz, The entropy and enthalpy of lithium intercalation into graphite, *Journal of Power Sources* 119-121 (2003) 850-855.
- [176] R.E. Williford, V.V. Viswanathan, J.-G. Zhang, Effects of entropy changes in anodes and cathodes on the thermal behavior of lithium ion batteries, *Journal of Power Sources* 189 (2009) 101-107.
- [177] Y.F. Reynier, R. Yazami, B. Fultz, Thermodynamics of lithium intercalation into graphites and disordered carbons, *Journal of the Electrochemical Society* 151 (2004) A422-A426.
- [178] V.V. Viswanathan, D. Choi, D. Wang, W. Xu, S. Towne, R.E. Williford, J.-G. Zhang, J. Liu, Z. Yang, Effect of entropy change of lithium intercalation in cathodes and anodes on Li-ion battery thermal management, *Journal of Power Sources* 195 (2010) 3720-3729.
- [179] V.A. Sethuraman, L.J. Hardwick, V. Srinivasan, R. Kostecki, Surface structural disordering in graphite upon lithium intercalation/deintercalation, *Journal of Power Sources* 195 (2010) 3655-3660.
- [180] M. Winter, J.O. Besenhard, M.E. Spahr, P. Novák, Insertion electrode materials for rechargeable lithium batteries, *Advanced Materials* 10 (1998) 725-763.
- [181] K.E. Thomas, J. Newman, Thermal modeling of porous insertion electrodes, *Journal of the Electrochemical Society* 150 (2003) A176-A192.
- [182] J.P. Schmidt, A. Weber, E. Ivers-Tiffée, A novel and precise measuring method for the entropy of lithium-ion cells – ΔS via electrothermal impedance spectroscopy, *Electrochimica Acta* 137 (2014) 311-319.

- [183] B.J. Cantwell, *Aircraft and Rocket Propulsion – Chapter 9: Thermodynamics of reacting mixtures*, Stanford, CA, USA (2007).
- [184] T.M. Bandhauer, S. Garimella, T.F. Fuller, A critical review of thermal issues in lithium-ion batteries, *Journal of the Electrochemical Society* 158 (2011) R1-R25.
- [185] G. Liu, M. Ouyang, L. Lu, J. Li, X. Han, Analysis of the heat generation of lithium-ion battery during charging and discharging considering different influencing factors, *Journal of Thermal Analysis Calorimetry* 116 (2014) 1001-1010.
- [186] C. Forgez, D. Vinh Do, G. Friedrich, M. Morcrette, C. Delacourt, Thermal modeling of a cylindrical LiFePO₄/graphite lithium-ion battery, *Journal of Power Sources* 195 (2010) 2961-2968.
- [187] H. Herwig, *Wärmeübertragung A-Z – Systematische und ausführliche Erläuterungen wichtiger Größen und Konzepte*, Springer (2000) 21-22.
- [188] H. Maleki, Thermal properties of lithium-ion battery and components, *Journal of the Electrochemical Society* 146 (1999) 947-947.
- [189] Y. Ye, Y. Shi, N. Cai, J. Lee, X. He, Electro-thermal modeling and experimental validation for lithium ion battery, *Journal of Power Sources* 199 (2012) 227-238.
- [190] SLPB(Superior Lithium Polymer Battery) Technical Specification, Kokam Co. Ltd, May 17, 2010.
- [191] M. Ender, A. Weber, E. Ivers-Tiffée, Analysis of three-electrode setups for AC-impedance measurements on lithium-ion cells by FEM simulations, *Journal of the Electrochemical Society* 159 (2012) A128-A136.
- [192] M. Ecker, N. Nieto, S. Käbitz, J. Schmalstieg, H. Blanke, A. Warnecke, D.U. Sauer, Calendar and cycle life study of Li(NiMnCo)O₂-based 18650 lithium-ion batteries, *Journal of Power Sources* 248 (2014) 839-851.
- [193] J. Wang, J. Purewal, P. Liu, J. Hicks-Garner, S. Soukazian, E. Sherman, A. Sorenson, L. Vu, H. Tatara, M.W. Verbrugge, Degradation of lithium ion batteries employing graphite negatives and nickel–cobalt–manganese oxide + spinel manganese oxide positives – Part 1: Aging mechanisms and life estimation, *Journal of Power Sources* 269 (2014) 937-948.
- [194] M. Bauer, C. Guenther, M. Kasper, M. Petzl, M.A. Danzer, Discrimination of degradation processes in lithium-ion cells based on the sensitivity of aging indicators towards capacity loss, *Journal of Power Sources* 283 (2015) 494-504.
- [195] T. Waldmann, M. Wilka, M. Kasper, M. Fleischhammer, M. Wohlfahrt-Mehrens, Temperature dependent ageing mechanisms in lithium-ion batteries – A post-mortem study, *Journal of Power Sources* 262 (2014) 129-135.
- [196] H.-p. Lin, D. Chua, M. Salomon, H.-C. Shiao, M. Hendrickson, E. Plichta, S. Slane, Low-temperature behavior of Li-ion cells, *Electrochemical and Solid-State Letters* 4 (2001) A71-A73.

- [197] N.S. Hudak, L.E. Davis, G. Nagasubramanian, Cycling-induced changes in the entropy profiles of lithium cobalt oxide electrodes, *Journal of the Electrochemical Society* 162 (2014) A315-A321.
- [198] B. Stiaszny, J.C. Ziegler, E.E. Krauß, M. Zhang, J.P. Schmidt, E. Ivers-Tiffée, Electrochemical characterization and post-mortem analysis of aged LiMn₂O₄–NMC/graphite lithium ion batteries part II – Calendar aging, *Journal of Power Sources* 258 (2014) 61-75.
- [199] E. Sarasketa-Zabala, I. Gandiaga, L.M. Rodriguez-Martinez, I. Villarreal, Calendar ageing analysis of a LiFePO₄/graphite cell with dynamic model validations – Towards realistic lifetime predictions, *Journal of Power Sources* 272 (2014) 45-57.
- [200] R. Wright, J. Christophersen, C. Motloch, J. Belt, C. Ho, V. Battaglia, J. Barnes, T. Duong, R. Sutula, Power fade and capacity fade resulting from cycle-life testing of Advanced Technology Development Program lithium-ion batteries, *Journal of Power Sources* 119-121 (2003) 865-869.
- [201] K. Takei, K. Kumai, Y. Kobayashi, H. Miyashiro, N. Terada, T. Iwahori, T. Tanaka, Cycle life estimation of lithium secondary battery by extrapolation method and accelerated aging test, *Journal of Power Sources* 97-98 (2001) 697-701.
- [202] W. Prochazka, G. Pregartner, M. Cifrain, Design-of-experiment and statistical modeling of a large scale aging experiment for two popular lithium ion cell chemistries, *Journal of the Electrochemical Society* 160 (2013) A1039-A1051.
- [203] D. Wong, B. Shrestha, D.A. Wetz, J.M. Heinzel, Impact of high rate discharge on the aging of lithium nickel cobalt aluminum oxide batteries, *Journal of Power Sources* 280 (2015) 363-372.
- [204] A. Matasso, D. Wong, D. Wetz, F. Liu, Effects of high-rate cycling on the bulk internal pressure rise and capacity degradation of commercial LiCoO₂ cells, *Journal of the Electrochemical Society* 162 (2015) A885-A891.
- [205] G. Ning, B. Haran, B.N. Popov, Capacity fade study of lithium-ion batteries cycled at high discharge rates, *Journal of Power Sources* 117 (2003) 160-169.
- [206] Y. Kim, Investigation of the gas evolution in lithium ion batteries – Effect of free lithium compounds in cathode materials, *Journal of Solid State Electrochemistry* 17 (2013) 1961-1965.
- [207] A. Würsig, W. Scheifele, P. Novák, CO₂ gas evolution on cathode materials for lithium-ion batteries, *Journal of the Electrochemical Society* 154 (2007) A449-A454.
- [208] A. Devie, Intrinsic degradation variability in commercial lithium-ion batteries, 228th *ECS Meeting*, Phoenix, AZ, USA (2015).
- [209] D. Aurbach, B. Markovsky, M. Levi, E. Levi, A. Schechter, M. Moshkovich, Y. Cohen, New insights into the interactions between electrode materials and electrolyte solutions for advanced nonaqueous batteries, *Journal of Power Sources* 81-82 (1999) 95-111.
- [210] S. Rodrigues, N. Munichandraiah, A.K. Shukla, AC impedance and state-of-charge analysis of a sealed lithium-ion rechargeable battery, *Journal of Solid State Electrochemistry* 3 (1999) 397-405.

- [211] P. Arora, B.N. Popov, R.E. White, Electrochemical investigations of cobalt-doped LiMn_2O_4 as cathode material for lithium-ion batteries, *Journal of the Electrochemical Society* 145 (1998) 807-815.
- [212] Y.-M. Choi, S.-I. Pyun, Effects of intercalation-induced stress on lithium transport through porous LiCoO_2 electrode, *Solid State Ionics* 99 (1997) 173-183.
- [213] M. Zhou, L. Zhao, S. Okada, J. Yamaki, Quantitative studies on the influence of LiPF_6 on the thermal stability of graphite with electrolyte, *Journal of the Electrochemical Society* 159 (2012) A44-A48.
- [214] J. Yamaki, Thermal stability of graphite anode with electrolyte in lithium-ion cells, *Solid State Ionics* 148 (2002) 241-245.
- [215] X. Feng, J. Sun, M. Ouyang, X. He, L. Lu, X. Han, M. Fang, H. Peng, Characterization of large format lithium ion battery exposed to extremely high temperature, *Journal of Power Sources* 272 (2014) 457-467.
- [216] M. Dubarry, C. Truchot, B.Y. Liaw, K. Gering, S. Sazhin, D. Jamison, C. Michelbacher, Evaluation of commercial lithium-ion cells based on composite positive electrode for plug-in hybrid electric vehicle applications – III. Effect of thermal excursions without prolonged thermal aging, *Journal of the Electrochemical Society* 160 (2012) A191-A199.
- [217] M.B. Pinson, M.Z. Bazant, Theory of SEI formation in rechargeable batteries – capacity fade, accelerated aging and lifetime prediction, *Journal of the Electrochemical Society* 160 (2013) A243-A250.
- [218] H.J. Ploehn, P. Ramadass, R.E. White, Solvent diffusion model for aging of lithium-ion battery cells, *Journal of the Electrochemical Society* 151 (2004) A456-A462.
- [219] D. Mohanty, K. Dahlberg, D.M. King, L.A. David, A.S. Sefat, D.L. Wood, C. Daniel, S. Dhar, V. Mahajan, M. Lee, F. Albano, Modification of Ni-rich FCG NMC and NCA cathodes by atomic layer deposition – Preventing surface phase transitions for high-voltage lithium-ion batteries, *Scientific Reports* 6 (2016) 26532-26532.
- [220] K. Kleiner, D. Dixon, P. Jakes, J. Melke, M. Yavuz, C. Roth, K. Nikolowski, V. Liebau, H. Ehrenberg, Fatigue of $\text{LiNi}_{0.8}\text{Co}_{0.15}\text{Al}_{0.05}\text{O}_2$ in commercial Li ion batteries, *Journal of Power Sources* 273 (2015) 70-82.
- [221] S. Watanabe, M. Kinoshita, T. Hosokawa, K. Morigaki, K. Nakura, Capacity fading of $\text{LiAl}_y\text{Ni}_{1-x-y}\text{Co}_x\text{O}_2$ cathode for lithium-ion batteries during accelerated calendar and cycle life tests – Effect of depth of discharge in charge-discharge cycling on the suppression of the micro-crack generation of $\text{LiAl}_y\text{Ni}_{1-x-y}\text{Co}_x\text{O}_2$ particle, *Journal of Power Sources* 260 (2014) 50-56.
- [222] J. Zhou, P. Notten, Studies on the degradation of Li-ion batteries by the use of microreference electrodes, *Journal of Power Sources* 177 (2008) 553-560.

- [223] T. Nonaka, C. Okuda, Y. Seno, Y. Kondo, K. Koumoto, Y. Ukyo, Surface sensitive X-ray absorption study on $\text{LiNi}_{0.8}\text{Co}_{0.15}\text{Al}_{0.05}\text{O}_2$ cathode material for lithium ion batteries, *Journal of the Electrochemical Society* 154 (2007) A353-A358.
- [224] M.-S. Wu, P.-C.J. Chiang, J.-C. Lin, Electrochemical investigations on capacity fading of advanced lithium-ion batteries by three-electrode measurements, *Journal of the Electrochemical Society* 152 (2005) A47-A52.
- [225] D.A. Stevens, R.Y. Ying, R. Fathi, J.N. Reimers, J.E. Harlow, J.R. Dahn, Using high precision coulometry measurements to compare the degradation mechanisms of NMC/LMO and NMC-only automotive scale pouch cells, *Journal of the Electrochemical Society* 161 (2014) A1364-A1370.
- [226] D. Li, D.L. Danilov, J. Xie, L. Raijmakers, L. Gao, Y. Yang, P.H. Notten, Degradation mechanisms of $\text{C}_6/\text{LiFePO}_4$ batteries – Experimental analyses of calendar aging, *Electrochimica Acta* 190 (2016) 1124-1133.
- [227] D.J. Sheskin, *Handbook of Parametric and Nonparametric Statistical Procedures*, 3rd edition, Chapman & Hall/CRC (2004).